THE SPATIO-TEMPORAL BEHAVIOR OF BASIC MULTICELLULAR UNITS IN A PTH-INDUCED CORTICAL BONE REMODELING RABBIT MODEL

A Thesis Submitted to the
College of Graduate and Postdoctoral Studies
In Partial Fulfillment of the Requirements
For the Degree of Masters of Science
In the Department of Anatomy, Physiology and Pharmacology
University of Saskatchewan
Saskatoon

By

Erika da Silva Sales

PERMISSION TO USE

In presenting this thesis/dissertation in partial fulfillment of the requirements for a Postgraduate degree from the University of Saskatchewan, I agree that the Libraries of this University may make it freely available for inspection. I further agree that permission for copying of this thesis/dissertation in any manner, in whole or in part, for scholarly purposes may be granted by the professor or professors who supervised my thesis/dissertation work or, in their absence, by the Head of the Department or the Dean of the College in which my thesis work was done. It is understood that any copying or publication or use of this thesis/dissertation or parts thereof for financial gain shall not be allowed without my written permission. It is also understood that due recognition shall be given to me and to the University of Saskatchewan in any scholarly use which may be made of any material in my thesis/dissertation.

Requests for permission to copy or to make other uses of materials in this thesis/dissertation in whole or part should be addressed to:

Head of the Department of Anatomy, Physiology and Pharmacology
Health Science Building
107 Wiggins Rd
University of Saskatchewan
Saskatoon, Saskatchewan S7N 5E5 Canada

OR

Dean
College of Graduate and Postdoctoral Studies
University of Saskatchewan
116 Thorvaldson Building, 110 Science Place
Saskatoon, Saskatchewan S7N 5C9 Canada

ABSTRACT

The adult skeleton is continuously renewed by the bone remodeling process, which is carried out by coupled and balanced activities, localized in time and space, via cellular groupings known as basic multicellular units (BMUs). In cortical bone, a BMU is depicted as a cutting cone of osteoclasts in the front resorbing bone, followed by a reversal phase, and then a closing cone lined by osteoblasts behind forming new bone. Any imbalance in this sequence of events can lead to bone diseases such as osteoporosis. Although it is well known that many factors affect BMU activity and contribute to osteoporosis, little is known about BMU dynamic spatio-temporal regulation. The rate of BMU progression, their longitudinal erosion rate (LER) is a key example of where knowledge is lacking. LER has only been inferred by 2D (histological) double-labeling techniques based on remodeling in a steady state where the cutting cone advance is equal to that of the closing cone. If these spatio-temporal relationships are valid and constant, increasing the bone formation rate, as observed with recombinant parathyroid hormone (PTH), an anabolic treatment for osteoporosis, would concomitantly elevate LER. The present study utilizes a new methodology to explore whether the increased cortical remodeling activity induced by PTH, including accelerated bone formation, leads to an elevated LER. BMU progression was manipulated via different dosing regimens: PTH and PTH withdrawal (PTHW). It was hypothesized that LER would be higher during active dosing. After 14 days of PTH dosing, rabbit distal right tibiae were imaged *in vivo* by synchrotron-based phase-contrast micro-CT. For the following 14 days, the PTH group received the same treatment while the PTHW group was administered saline. At 28 days, the rabbits were then euthanized, and the tibiae were imaged *ex vivo* by micro-CT. The *in vivo* and *ex vivo* right limb data sets were then registered, and LER was measured as the distance traversed by BMU cutting cones divided by 14 days. A total of 638 BMUs were assessed. Counter to the hypothesis, LER was lower in the PTH (34.61 μm/day) compared with the PTHW (39.37 μm/day; $p < 0.01$) group. Slower BMU progression suggests that PTH has an important role in enhancing coupling both by increasing bone formation and slowing the advance of bone resorption within BMUs. This novel insight into BMU dynamics indicates that further investigation into LER modulation is warranted, with potential implications for combatting remodeling-related disease, improving treatment, and potentially reducing drug side effects.

ACKNOWLEDGEMENTS

Foremost, I would like to express my sincere gratitude to my supervisor Dr. David Cooper who made this work possible. His guidance and advice carried me through all the stages of my thesis. And for that, I am really thankful. I also would like to thank the other members of my advisory committee, Dr. Terra Arnason and Dr. Dean Chapman, for their advice and thoughtful input on my work in every meeting we had. I am also grateful for their support, especially in the last four months.

My sincere gratitude goes to my lab mates who have contributed to this work, Kim Harrison, Beverly Hiebert, Gavin King, and Kush Parolia. Especially to Kim, now Dr. Harrison, who guided me through all the experiments with the rabbits. I also would like to thank Dr. Kurtis Swekla and the Laboratory Animal Services Unit staff for their assistance with the animals.

The Biomedical Imaging and Therapy (BMIT-BM 05B1-1 beamline) facility at the Canadian Light Source (CLS) played an essential role in this project relating to acquiring the *in vivo* images that were the key to studying BMUs behaviour. I want to thank the CLS staff and the beamline scientists, Dr. Ning Zhu, Dr. Arash Panahifar, and Dr. Sergei Gasilov, for all the support given during my beamtime.

I want to acknowledge the provincial government of Saskatchewan for the Saskatchewan Innovation & Opportunity Scholarship, the University of Saskatchewan College of Medicine for the College of Medicine Graduate Student Awards (CoMGRAD), and Dr. David Cooper; who has also provided financial support for this thesis.

Finally, I want to express my gratitude to my sisters Elizabeth and Caroline for their unconditional love, emotional support and being my rock and safe place.

DEDICATION

I dedicate this thesis to my beloved mother.

Angela Maria da Silva (1955 – 2021)

TABLE OF CONTENTS

LIST OF TABLES

LIST OF FIGURES

LIST OF ABBREVIATIONS

º – Degrees

% – Percent

2D – Two-dimensional

3D – Three-dimensional

4D – Four-dimensional

α – Alpha or Level of Significance

Ac.f – Activation Frequency

BMD – Bone Mineral Density

BMU – Basic Multicellular Unit

BV – Bone Volume

BV/TV – Bone Volume Fraction

C – Celsius

Ca.Dm – Canal Diameter

Ct.Ar – Cortical Area

Ct.Po – Cortical Porosity

Ct.Th – Cortical Thickness

CCAC – Canadian Council on Animal Care

CLS – Canadian Light Source

CI – Confidence Interval

cm – Centimeter

DXA – Dual Energy X-ray Absorptiometry

GC – Glucocorticoids

Gy – Gray

HR - pQCT – High-Resolution Peripheral Quantitative Computed Tomography

IQR – Interquartile Range

Kg – Kilogram

kVp – Peak Kilovoltage

LER – Longitudinal Erosion Rate

LFC – Length of Closing Cone

On.MAR – Osteonal Mineral Apposition Rate

Ma.Ar – Marrow Area

micro-CT – X-ray Microtomography

ml – Milliliter

mg – Milligram

mm – Millimeter

ms – Millisecond

n – Sample Size

OPG – Osteoprotegerin

OVX – Ovariectomy

OVX + GC – Ovariectomy + Glucocorticoid

PHPT – Primary Hyperparathyroidism

PTE – Parathyroid Extract

PTH – Parathyroid Hormone

PTHR1 – Parathyroid Hormone Receptor 1

RANK – Receptor Activator of Nuclear Factor Kappa-β

RANKL – Receptor Activator of Nuclear Factor Kappa-β Ligand

RER – Radial Erosion Rate

ROI – Region of Interest

SD – Standard Deviation

σ_r – Time of Radial Closure

SHAM – Sham OVX Control

TBD – Total Bone Density

Tb.N – Trabecular Number

Tb.Sp – Trabecular Separation

Tb.Th – Trabecular Thickness

Tt.Ar – Total Area

U – Unit

µA – Microampere

µg – Microgram

µm – Micrometer

CHAPTER 1. Introduction

1.1. Introduction

Osteoporosis is characterized by bone tissue deterioration and decreased bone mass, leading to reduced bone strength and increased susceptibility to fracture.[1] Bone deterioration can occur over several years without presenting any symptoms, which is why osteoporosis is also known as the "silent thief".[2] According to Osteoporosis Canada, two million Canadians aged ≥ 50 years are affected by osteoporosis, and at least one in three women and one in five men will break a bone due to the disease.[2] Osteoporosis-related fractures, especially fractures of the hip, are associated with disability, mortality, and a high treatment cost.[3,4] An estimated 22% of Canadian women and 33% of Canadian men die in their first year after a hip fracture.[2,4] The number of Canadians aged ≥ 65 years is expected to grow rapidly over the next decade, reaching as high as 25% of the population by 2036.[4] As Canadians age, the number of osteoporotic fractures is expected to increase; in 2014, the annual cost of osteoporosis in Canada was already estimated at over $4.6 billion CAD.[4] Bone is a living tissue that is constantly being resorbed and replaced. Osteoporosis occurs when the replacement of new bone at the microstructural level does not keep up with the resorption of old bone.

At the macrostructure level, bone is classified by two types of tissue: **cortical bone** (or compacta) and **trabecular bone** (or spongiosa). About 80% of total bone mass is cortical bone, which forms the outer wall of all bones. The remaining 20% of the bone mass is trabecular bone, which is found mainly in the bones of the axial skeleton and within the ends of long bones.[5] In healthy adults, cortical and trabecular bone are continuously renewed at the microstructural level to maintain their structure and integrity by a process known as bone **remodeling**. Remodeling occurs on any of the four bone surfaces/envelopes—**periosteal, endocortical, intracortical,** and **trabecular** (Figure 1.1)—and it is carried out by intricate arrangements of cells, referred to by Frost as **basic multicellular units (BMUs)**.[6] In remodeling of the intracortical envelope (the focus of this thesis) a BMU initiates within a **Haversian or Volkmann's canal**.[7]

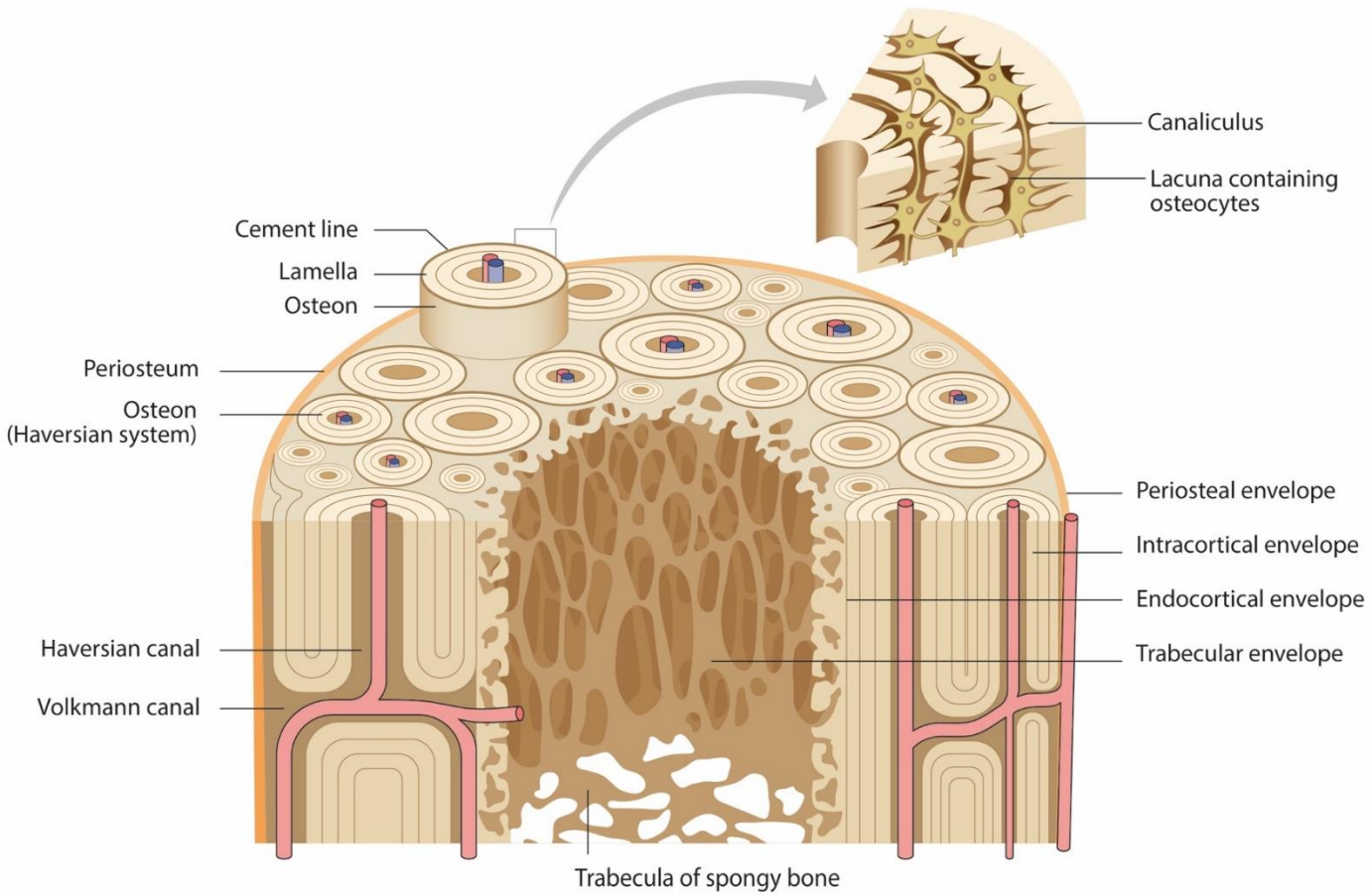

Figure 1.1. Bone anatomy. Diagram showing cortical and trabecular bone with the four bone surfaces/envelopes: periosteal, intracortical, endocortical, and trabecular. Illustration created by Gabriela Machado.

BMU's morphology is an elongated cylindrical structure comprising a **cutting cone** of **osteoclasts** in the front resorbing bone matrix, followed by a reversal phase, and then a **closing cone** lined by **osteoblasts** behind forming new bone. The remaining space in the cavity is occupied by connective tissue, blood vessels, and nerves (Figure 1.2).[7] The final product of an intracortical remodeling event is a **secondary osteon**, a structure composed of concentric layers of bone enclosed by a **cement line** and surrounding a central canal, collectively also referred to as a **Haversian system**. Alternatively, primary osteons form directly during bone development and growth (modeling, discussed in Chapter 2) and therefore, have no cement line. In trabecular, endocortical, and periosteal remodeling no blood vessels are incorporated and the final product is called a **hemiosteon**.[7,8] This thesis focuses on remodeling and, specifically, that occurring within cortical bone.

The process of remodeling consists of four sequential and distinct phases of cellular events: activation, resorption, reversal, and formation. This is often referred to as the **remodeling cycle**.[9,10] The **activation phase** is the first stage of bone remodeling, and it involves the detection of an initiating signal. This signal can take different forms, such as direct mechanical strain on the bone, which leads to structural damage, or hormonal effects (e.g., estrogen or parathyroid hormone) on bone cells.[9] Once there is a remodeling signal, osteoclast precursors are attracted to the bone surface, followed by differentiation and fusion to become fully functional osteoclasts. As soon as mature osteoclasts are present, bone-lining cells retract from the bone surface to expose the mineralized matrix. This appears to be an active process, and it is stimulated either by osteoclasts themselves as they approach the surface or by the same signal that initiated remodeling.[9] Without retraction of the bone-lining cells, osteoclasts cannot bind to the bone and begin resorption.[10,11] In the **resorption phase,** osteoclasts actively break down bone tissue by dissolving mineral and degrading collagen fibrils. As resorption proceeds, new osteoclasts are recruited to the remodeling site to either support existing osteoclasts or replace those that die. Once osteoclasts have finished resorbing bone, the remaining collagen fibrils on the exposed surface must be removed.[10] This is the beginning of the **reversal phase**, which is currently thought to be done by a specialized form of bone lining cells, known as reversal cells.[12] If the collagen fibril fragments are not removed, bone formation by osteoblasts does not proceed.[11]

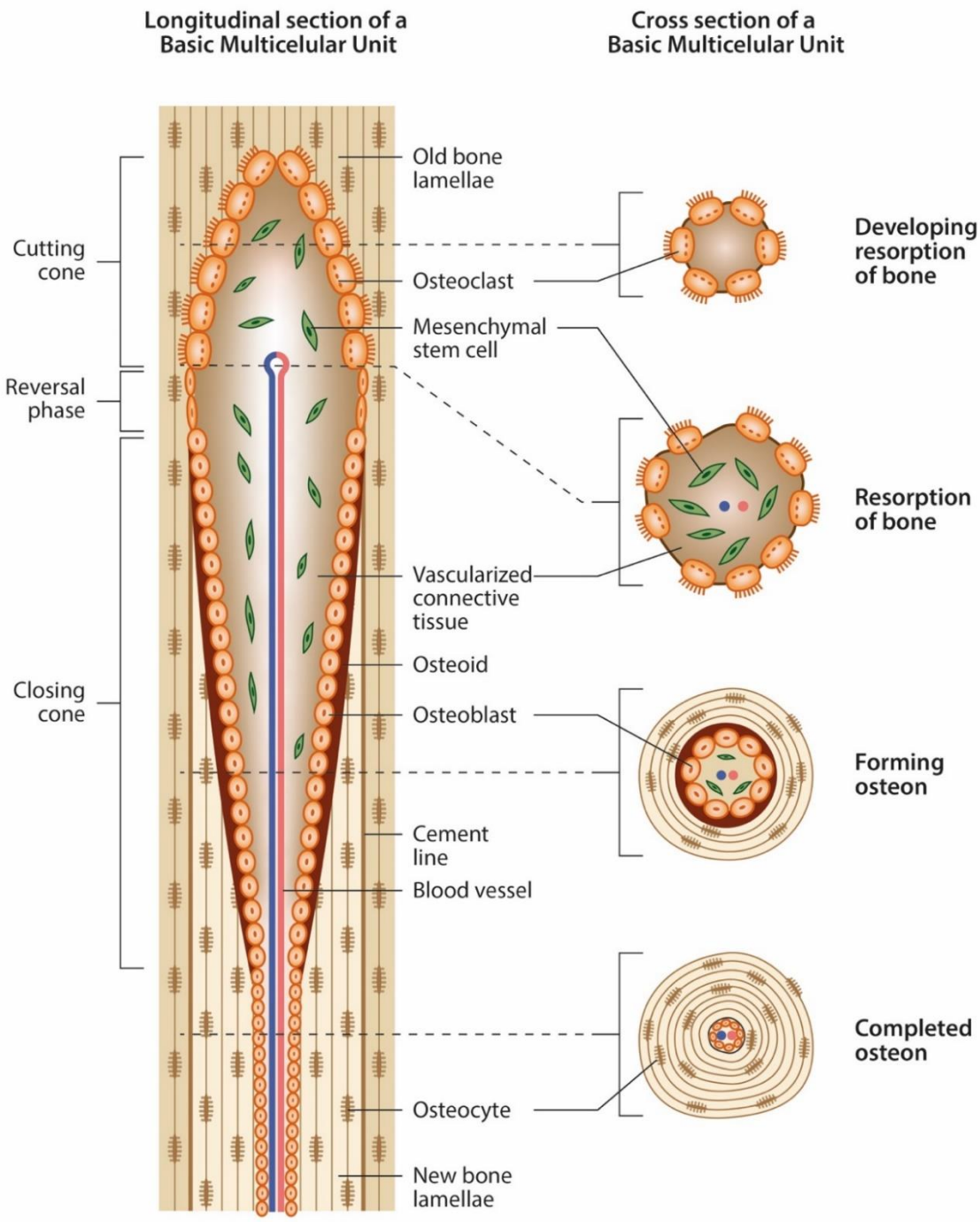

Figure 1.2. A diagram of a basic multicellular unit (BMU) in cortical remodeling. Illustration created by Gabriela Machado.

These reversal cells, which cover most eroded surfaces, are also thought to deposit a thin layer of new bone matrix (the cement or reversal line). This clear histologic feature delineates Haversian systems' boundaries from the surrounding older matrix.[12] During the **formation phase**, osteoblasts create a nonmineralized organic matrix (osteoid) consisting mainly of type I collagen fibers which serve as a template for inorganic hydroxyapatite crystals. The osteoblasts involved in bone formation experience one of three fates. The majority (90%) die as a result of apoptosis and may be replaced by new osteoblasts if local formation is still needed. Another portion of osteoblasts will be incorporated into the osteoid matrix and eventually become osteocytes embedded within lacunae. Finally, the osteoblasts left over at the end of the formation phase may remain on the bone's surface as inactive bone lining cells. These bone lining cells retain the ability to be activated and to start producing bone matrix again. At the end of a bone remodeling cycle, the new bone matrix will continue to mineralize over time.[10,11]

In healthy individuals, resorption, reversal, and formation are always **coupled and balanced**.[10] Coupling refers to the coordination of activities in time and space of osteoclasts and osteoblasts in each BMU, whereas balance refers to the amount of bone tissue resorbed and formed by a BMU. Any imbalance between resorption and formation (with a reduction in the volume of bone formed, an increase in the volume of bone resorbed, or both) disturbs the harmony of BMUs. **Such disturbances are the root cause of osteoporosis.**

Osteoporosis is traditionally categorized into primary (type I and type II) and secondary forms.[1] **Primary type I osteoporosis** (or **postmenopausal osteoporosis**) is a common bone disorder in postmenopausal women and is caused by estrogen deficiency resulting from menopause. Estrogen affects osteoclasts, osteoblasts, and osteocytes, and estrogen deficiency leads to an increased bone remodeling rate and an imbalance between bone formation and bone resorption. These changes in bone remodeling balance affect both trabecular bone (e.g., thinning and loss of trabeculae) and cortical bone (e.g., cortical thinning and increased porosity).[13] On the other hand, **primary type II osteoporosis** (also known as **senile osteoporosis**) is associated with aging in both women and men.[1] It is caused by decreased bone formation by aging bone cells.[13] **Secondary osteoporosis** is defined as a bone disorder that is a secondary complication of an underlying medical condition, immobility, or adverse results of therapeutic interventions such as the use of glucocorticoids to treat specific diseases.[1] Glucocorticoids induce bone loss via osteoblast suppression, and by stimulating osteoclastogenesis, and consequently cause uncoupling

between resorption and formation.[14] **Osteoporosis therapy** is divided into antiresorptive and anabolic agents.[15,16] **Antiresorptive agents** such as bisphosphonates and denosumab are widely used to treat osteoporosis. Bisphosphonates, which are the most prescribed antiresorptive agents, inactivate and promote osteoclasts apoptosis, inhibiting bone resorption and increasing bone mineral density (BMD).[17] Denosumab is a fully human monoclonal antibody that binds to the receptor activator of nuclear factor-κB ligand (RANKL). RANKL is essential for osteoclast differentiation, activation, and survival. Therefore, Denosumab suppresses the development, activation, and survival of osteoclasts.[17,18] In BMUs, however, resorption and formation are coupled; therefore, suppressing resorption also suppresses formation. Consequently, the increased BMD occurs as a result of the mineralization of the existing bone and not by an increase in bone formation; thus, antiresorptive agents cannot reverse the bone tissue deterioration that is a characteristic of the disease.[16] On the other hand, **anabolic agents** act on osteoblasts increasing new bone formation. Teriparatide, which is a **parathyroid hormone (PTH)** analogue that consists of the first 34 amino acids, is the first anabolic medication approved to treat osteoporosis.[15] PTH has a profound effect on the skeleton at the tissue level. Elevated circulating levels of PTH can generate both **catabolic and anabolic effects** in bone, depending on the temporal profile of its increase.[19] Continuous elevation in PTH, as in primary and secondary hyperparathyroidism, increases the rate of remodeling and can result in bone loss. On the other hand, daily administration of recombinant PTH has shown to improve both cortical and trabecular bone in osteoporotic patients.[20,21] Teriparatide administration used to be limited to two years to treat osteoporosis, as this agent was associated with the occurrence of osteosarcoma in rats exposed to a high dose of PTH over a two-year period.[22] However, in November 2020, the US Food and Drug Administration (FDA) removed the two years lifetime treatment limitation.[23]

The ideal therapy for patients with osteoporosis, or those at risk of developing the disease, must aim to improve coupling and balance between resorption and formation within individual BMUs. **However, little is known about the spatio-temporal regulation of a BMU.** Although it is well known that many factors affect BMU activity and contribute to osteoporosis, it is not well established how these factors impact the precise mode of a BMU advance in three-dimensional (3D) space over time (or four-dimensional - 4D). Modulation of remodeling, rather than elimination (as achieved by antiresorptive agents), represents a better strategy to prevent and potentially reverse osteoporosis. If BMUs can be closely coupled with balanced resorption and

formation, slowed in their progression, and spatially constrained to avoid coalescence into large pores, then bone tissue can be more safely preserved and even improved, reducing the risk of osteoporotic fractures. To reach this goal, it is necessary to advance our fundamental understanding of BMU spatio-temporal regulation. Only a few studies in the literature from the 1970s[24–26] and 80s[7] that have inferred the rate of progression of BMUs, defined as **longitudinal erosion rate (LER),** in dogs by 2D (histological) double-labeling techniques. In these classical studies, LER was calculated assuming that the advance of the cutting cone (unmeasurable) matched the advance of the closing cone (measurable by 2D histology). If such a relationship is valid and constant, then an increase in bone formation as observed with anabolic agents such as PTH,[27–30] for example, would concomitantly elevate LER. However, the direct measurement of LER in 3D space over time has been beyond reach for several reasons, including the small scale of cortical pores in clinical and preclinical models, and the high radiation dose necessary to detect them.[31,32] Another limitation is regarding a suitable preclinical (animal) model that exhibits cortical remodeling.

In clinical studies, high-resolution peripheral quantitative computed tomography (HR-pQCT) is the most advanced imaging method for assessing 3D microarchitecture and BMD in cortical and trabecular bone of the distal radius and tibia.[33] This modality has a nominal resolution (or standard isotropic voxel size) of 82 μm, and 61 μm in the second-generation scanners. However, the actual spatial resolution of the reconstructed images ranges from 92.5 to 154 μm (depending on the scanner generation); that said, both nominal resolutions limit this modality to image only the largest cortical pores (≥ 100 μm).[31,34] Another issue is that to measure LER, one would have to scan a patient twice in relatively quick succession, exposing the patient to two times the radiation dose. *In vivo* high-resolution X-ray microtomography (micro-CT) is well suited to provide 3D visualization of cortical bone microarchitecture, and it has the potential, from a resolution perspective, to directly measure LER accurately.[35] However, similar to HR-pQCT, a problem in acquiring LER *in vivo* with micro-CT is that the technique is based on absorption of X-rays and is directly related to radiation dose. For example, increasing the micro-CT image resolution by a factor of two increases the radiation dose by a factor of 16.[36] Even if one considers using an animal model to study LER, the relationship between resolution and radiation dose complicates *in vivo* imaging not only because it can be harmful to the animals, but also because it can potentially alter bone structure by altering BMU activities.[31] To overcome these resolution/radiation dose challenges, our group has been using **synchrotron-based phase-**

contrast micro-CT at an equivalent radiation dose of 2–3 Gy (~1–3 Gy being commonly used in laboratory micro-CT systems) to image cortical bone porosity.[32] In this technique, contrast is generated through the refractive index variations within the interface of bone tissue and pores, which allows *in vivo* images with high resolution/contrast to be acquired without the expense of radiation dose.[32] The Canadian Light Source (CLS) is located on the University of Saskatchewan campus and plays a central role in this thesis project. **Combining the use of synchrotron-based micro-CT imaging, with an appropriate animal model, can enable *in vivo* observation of BMU activity in 3D over time and the direct tracking of LER**.[37]

The ovariectomized rat is commonly used in experimental animal models for postmenopausal osteoporosis studies. However, it has several disadvantages, such as the failure to achieve true skeletal maturity (closure of the growth plates) and the low rate (or even absence) of remodeling in cortical bone.[38] These conditions limit the use of rats for the assessment of new treatments for osteoporosis, which require exploration of BMU dynamics in cortical bone remodeling. **Rabbits** are one of the smallest animal models that form Haversian systems by intracortical remodeling and reach skeletally maturity between six and nine months, when long bone growth plate closure occurs.[30,39,40] Despite the advantages of the rabbit model, it remains challenging to observe remodeling events in cortical bone because remodeling rates tend to be lower than those observed in trabecular bone. For a cortical bone model to be experimentally effective there is a need to boost the activation phase to increase the number of BMUs available for study within a given bone.[27] A recent study carried out by our group compared rabbit-based models of osteoporosis (ovariectomy [OVX], sham OVX control [SHAM], glucocorticoids [GC], and OVX+GC) with a PTH rabbit model.[27] The results showed that cortical porosity was substantially elevated in PTH rabbits relative to all other models of osteoporosis, and this was associated with increased remodeling rate and cortical pore size (Figure 1.3). PTH also increased periosteal and endosteal bone formation and osteonal mineral apposition rate (On.MAR) at the intracortical surface. On the other hand, our study also showed that PTH increased bone volume fraction (BV/TV) and trabecular number (Tb.N), whereas a pattern of loss was observed for the other groups (Figure 1.4).[27]

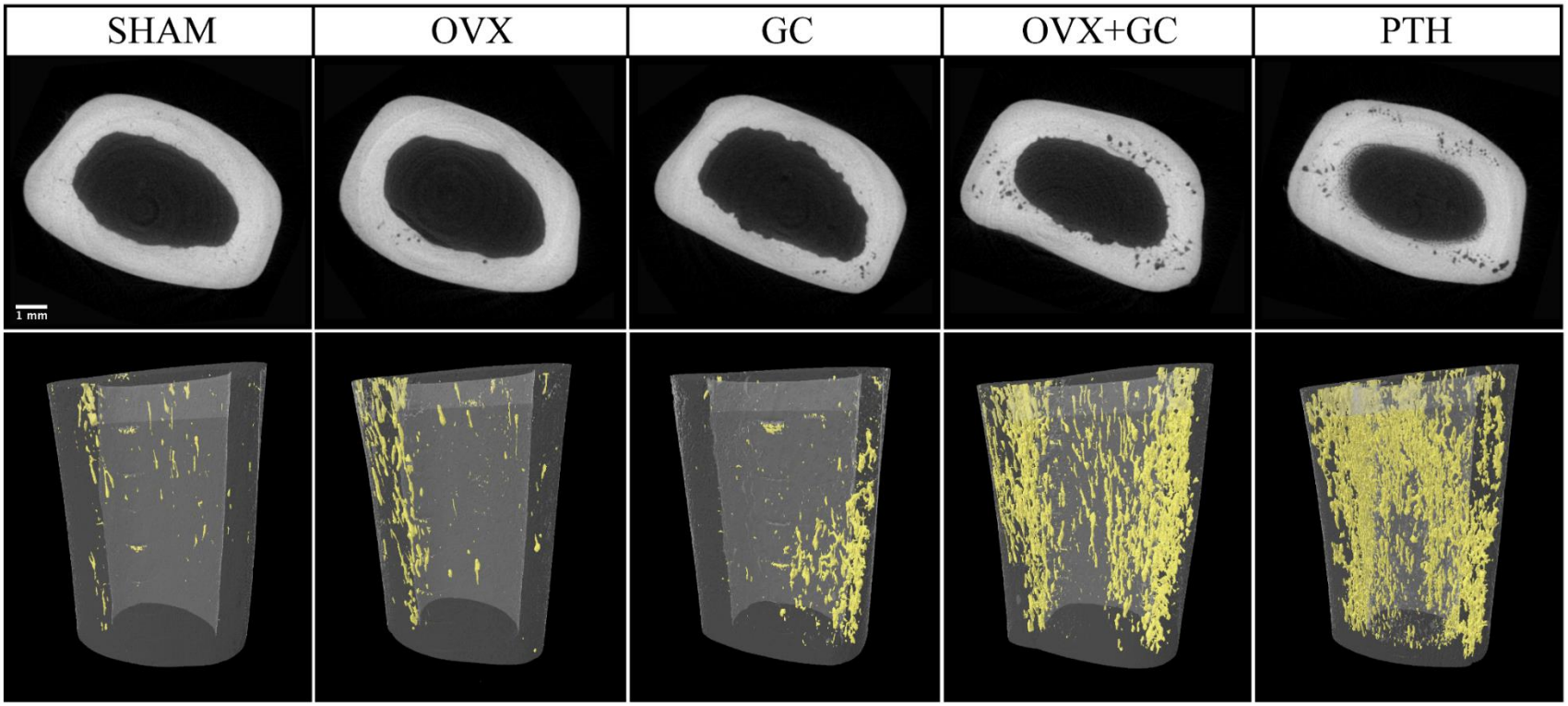

Figure 1.3. 3D micro-CT of cortical bone tibia in rabbit-based models of osteoporosis (ovariectomy [OVX], sham OVX control [SHAM], glucocorticoids [GC], and OVX+GC) and PTH, with cortical porosity highlighted in yellow. Image from Harrison et al.[27] with copyright permission to use.

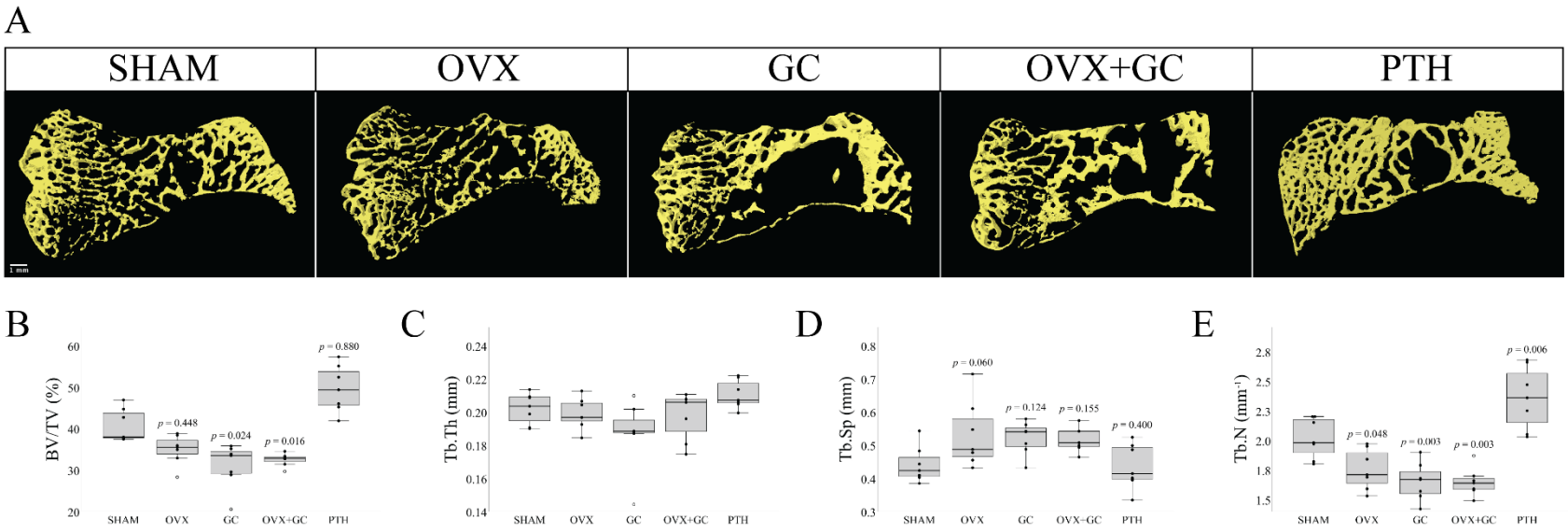

Figure 1.4. A: 3D reconstructed images of epiphyseal subchondral trabecular bone structure in rabbit-based models of osteoporosis (ovariectomy [OVX], sham OVX control [SHAM], glucocorticoids [GC], and OVX+GC) and PTH. Trabecular bone is highlighted in yellow. B-E: Trabecular bone histomorphometric quantification by micro-CT, where: BV/TV = bone volume fraction, Tb.Th = trabecular thickness, Tb.Sp = trabecular separation, and Tb.N = trabecular number. Image from Harrison et al.[27] with copyright permission to use.

These intriguing PTH-driven effects, catabolic in cortical bone and anabolic in trabecular bone, can be interpreted by the fact that PTH increases the rate of remodeling by the creation of new BMUs and by the rate of formative activities. However, it is unknown **how PTH affects spatio-temporal BMU regulation**, warranting further investigation. As mentioned above, teriparatide therapy is limited to two years to treat osteoporosis, as this agent is associated with the occurrence of osteosarcoma.[22] Additionally, there is no consensus in the literature regarding the immediate effects of PTH withdrawal on bone. A clinical study showed a degree of bone loss at the spine in postmenopausal women after teriparatide discontinuation, whereas another study showed a sustained reduction in vertebral fracture risk in postmenopausal women after 18 months of teriparatide interruption.[41,42] . In this thesis, the clinical withdrawal of PTH treatment will not be explored. However, it is of great clinical relevance to obtain information on how PTH impacts LER, which could be applied to developing efficient osteoporosis therapies that improve long-term use and limit adverse effects related to discontinuation.

1.2. Objective and Thesis Organization

A principal research goal in our group is to develop an imaging model capable of tracking remodeling events in 4D (3D over time). Currently, these efforts focus on using rabbits as our animal model and longitudinal synchrotron-based phase-contrast imaging to track BMUs.[37] This novel approach yields new insights into how BMU spatio-temporal behavior contributes to the bone tissue alterations observed in osteoporosis and, ultimately, will provide a platform for improving existing therapies and developing new ones. **In this thesis, I investigate the spatio-temporal behavior of BMUs in cortical bone of PTH-dosed rabbits.** PTH is well known to have anabolic action on bone. Therefore, an increase in bone formation by PTH should also increase LER advancement, based on the classical studies. Specifically, I manipulate BMU behavior via different dosing regimens - PTH and PTH withdrawal (PTHW) to test the hypothesis that LER is higher during active dosing compared with PTHW.

This thesis is structured into four chapters. Chapter 1 provides an introduction and the rationale regarding the problem of tracking remodeling in 4D and outlines the thesis objective. In Chapter 2, a literature review focused on the analysis of the dynamic activity of BMUs, the cellular actions of PTH in trabecular and cortical bone, and the current state of 3D cortical bone imaging

is presented. Chapter 3 describes the main experiment of my thesis project. It is presented as a manuscript entitled “PTH Reduces Longitudinal Erosion Rate of Basic Multicellular Units During Cortical Bone Remodeling”. Chapter 4 consists of a summary of the overall findings and future directions for this research.

CHAPTER 2. Literature Review

2.1. Introduction

In this chapter, I present an historical review of bone literature with a focus on cortical bone, culminating with the modern view of bone biology related to BMU remodeling. I also present how BMUs were quantified in the past and present and how 4D imaging of bone can contribute to a better understanding of BMU progression and regulation. As the objective of this thesis is to manipulate BMU behavior using PTH, an additional review of the cellular actions of this hormone in bone is presented.

2.2. From the Earliest Works in Cortical Bone to BMU Remodeling

For almost 350 years, bone has been the subject of research for many scientists. Antonie van Leeuwenhoek (1677) was the first to report the microscopic observation of cortical bone structures.[43] He described cortical bone as a collection of "pipes" joined together, and he drew what we can consider the first 3D rendering of cortical bone microstructure (Figure 2.1A).[35] In his observations, van Leeuwenhoek also noted the presence of pores arranged longitudinally and transversely. Later, in 1691, van Leeuwenhoek's observations were confirmed by Clopton Havers[44] who described two types of interconnected pores providing routes to the medullary cavity. The longitudinal pores of cortical bone are known today as Haversian canals, in honor of Havers.

At the beginning of the 19th century, the structure and disorders of bone drew the interest of a British surgeon called John Howship (1781-1841).[45] In 1815, Howship wrote about his observations of the structure and organization of bones after they attained full growth.[46] Using a solar microscope to analyze bone sections, he made his observations on cortical tissue of long

bones and described longitudinal canals as having numerous lateral communications with the internal surface (endosteum) and with the external surface (periosteum). He also observed that the canals were larger than the vessels they contain. Figure 2.1 (B and C) presents Howship's drawings of a longitudinal section of a cortical bone and its vascular canals. Two years later, Howship was in possession of a collection of diseased bones and began to study the changes that bone undergoes in pathological states. In his opinion, it was a subject neglected until that time.[47] He described that in some diseases, the longitudinal canals became uniformly larger, retaining their smooth and polished surfaces, whereas in other states they were less equally enlarged, and their cavities exhibited a rough and uneven appearance.

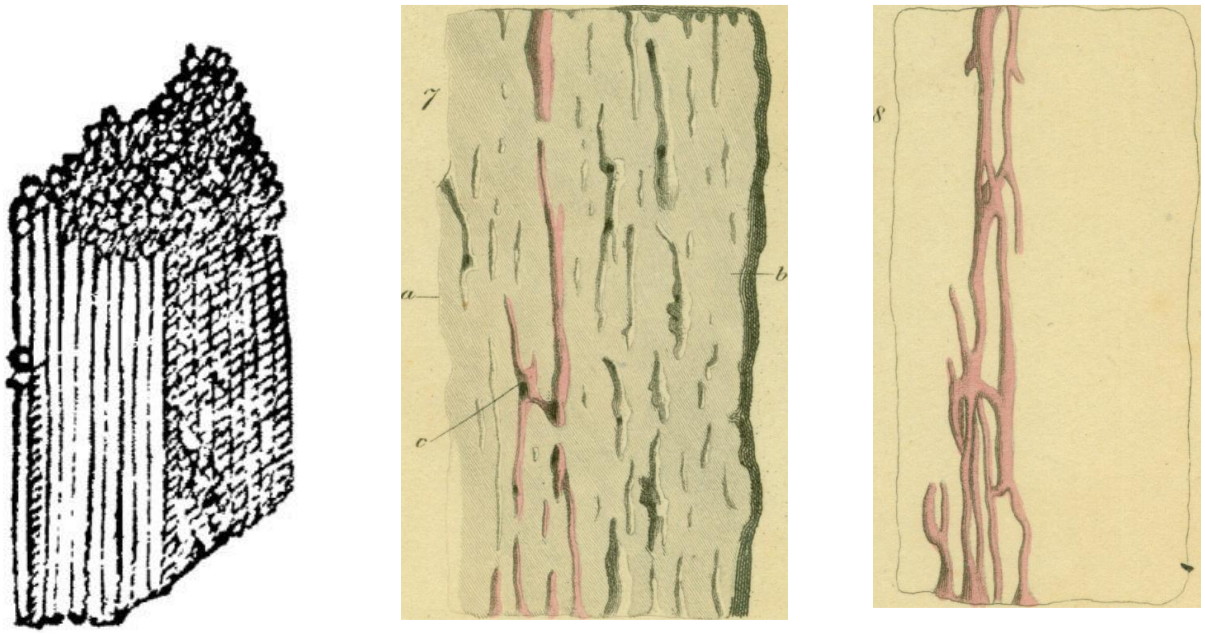

(A) (B) (C)

Figure 2.1. (A) Van Leeuwenhoek's drawing of a cortical bone. From Leeuwenhoek (1677).[43] (B) Howship's drawing of a longitudinal section of cortical bone where (a) endosteum, (b) periosteum and (c) Haversian canals are depicted. (C) Howship's drawing of vascular canals (c). From Howship (1815).[46]

More details of the structure of bone were then described by physiologists in the mid-19th century. In 1845, Todd and Bowmann[48] described cross sections of cortical bone as a patchwork

made up of Haversian systems (Haversian canals, their surrounding laminae, and their lacunae) linked by short laminae (referred to as interstitial laminae by Albert von Kölliker in 1850)[49] which occupy the spaces between the systems (Figure 2.2A). Following the work of Todd and Bowmann, Tomes and De Morgan in 1853 described the existence of spaces that are irregular in shape, corresponding to the peripheral outline of one or more Haversian systems.[49] They called them "Haversian spaces" (known today as resorption spaces) (Figure 2.2B). They pointed out that these spaces were essential to the development of Haversian systems and probably preceded the systems' formation. They also demonstrated that old bone tissue is removed in a packet, and a new one is developed in its place.

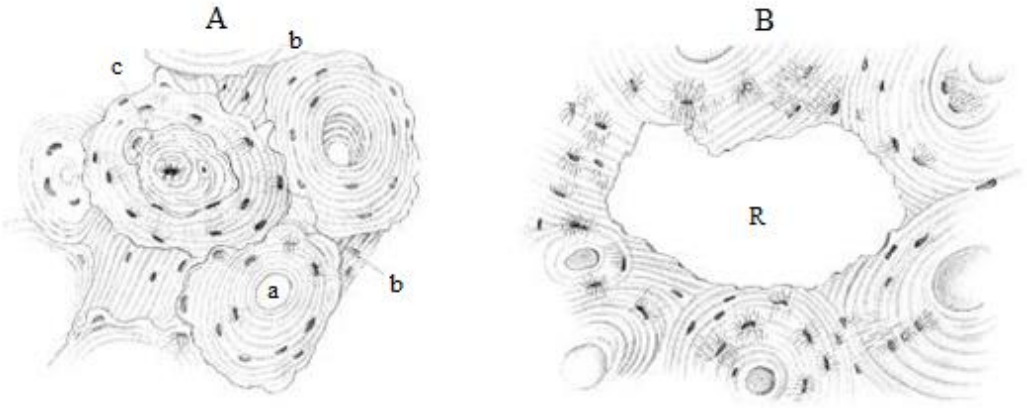

Figure 2.2. (A) a drawing of a cortical bone cross section showing a Haversian system (a), interstitial laminae (b), and a new Haversian system within an older one (c). (B) a drawing of a cortical bone cross section showing a Haversian or resorption space (R). Adapted from Tomes and De Morgan.[49]

In 1862, Volkmann,[50] studying Haversian canals in a case of osteomyelitis, noted that the canals were considerably widened, appearing like irregular marrow spaces with toothed borders (the same Haversian spaces described by Tomes and De Morgan[49]) and narrowed with a varying caliber. He also noted that the canals were not surrounded by concentric lamellae but broke through the lamellae surrounding the existing blood vessels. These canals had an irregular course, most of them horizontal but some diagonal and longitudinal. In some cases, they were extended like a "snake" through the entire cortex. Haversian spaces also caught the attention of Albert von Kölliker,[51] who applied histological methods to a study of physiological resorption and observed

the presence of multinucleated giant cells, which, in 1873, he called osteoclasts (bone breakers). In 1877, Schwalbe[50] described the transverse perforating canals linking the periosteum to the Haversian system and named them Volkmann's canals.

At the beginning of the 20th century, it was already established that osteoblasts form bone and osteoclasts resorb it[52] and that physiological resorption is important in the development of the skeleton. Pathologic resorptions started to gain more of the attention of researchers.[50,53] In 1930, Jaffe,[53] studying pathologic resorption in different specimens (experimental osteoporosis, bone tumors, and acute and inflammatory diseases), divided resorption into two processes: vascular and osteoclastic resorption. He reported a case of osteomyelitis and pointed out the same enlargement of the canals as Volkmann described in 1862. He also noted that some walls of the canals exhibited an indented appearance. Jaffe also described osteoclastic resorption as happening only in trabecular bone by a lacunar erosion (commonly known by this time as Howship's lacunae), and he believed that osteoclasts did not play any role in the vascular resorptions. However, on the other hand, he assumed the possibility that because in some cases vascular resorption was so extensive that it could overshadow osteoclastic resorption in cortical bone. The cellular mechanisms of bone were not yet understood at that time. Jaffe's vascular and osteoclast resorption theory of was then undermined by McLean and Rowland,[54] who, in 1963, pointed out the association of the "Haversian space" of Tomes and De Morgan[49] with the presence of the osteoclasts of Kölliker[51] and described that osteoclasts resorb bone cavities and extend them until they assume the form of tunnels, in which new Haversian systems form.

In 1964, Johnson,[55] studying longitudinal sections of cortical bone, confirmed McLean and Rowland's description and reported, for the first time, the cellular mechanisms by which a Haversian system is resorbed and formed. Johnson drew what he called a longitudinal and cross-sectional sketch of cavitation and refill (Figure 2.3). He described the sequence and relationship as follows:

> *"The cavity is formed by a broad, shallow, cone shaped osteoclastic wave front, the 'cutting cone', containing an average of 6 osteoclasts in the plane section. This is followed by a zone of scattered clasts planning down the jagged edges of Howship's lacunae and producing a slight further increase in diameter. The cutting cone is immediately followed by mesenchymal cell proliferation so that the spindle-shape cavity is at all times filled with connective tissue and blood*

vessels. Finally, there is a very long, slowly closing cone of osteoblastic lamellar refill."

Johnson diagrammed eight-hour intervals across 24 hours of the radial cavitation and refill (Figure 2.3 A, B, C = three generations of osteoclasts in the cutting cone seen in longitudinal and cross section; D = pause [later called reversal phase]; E, F, G = three stages of closing cone). He also stated that it takes 90 days to progress from E to G at the cross-sectional level and that the slope of the closing cone represents the same time period. Two years later, Frost[56] named the cellular sequence described by Johnson as the basic metabolizing unit and in 1969 renamed it **basic multicellular unit (BMU).**[6]

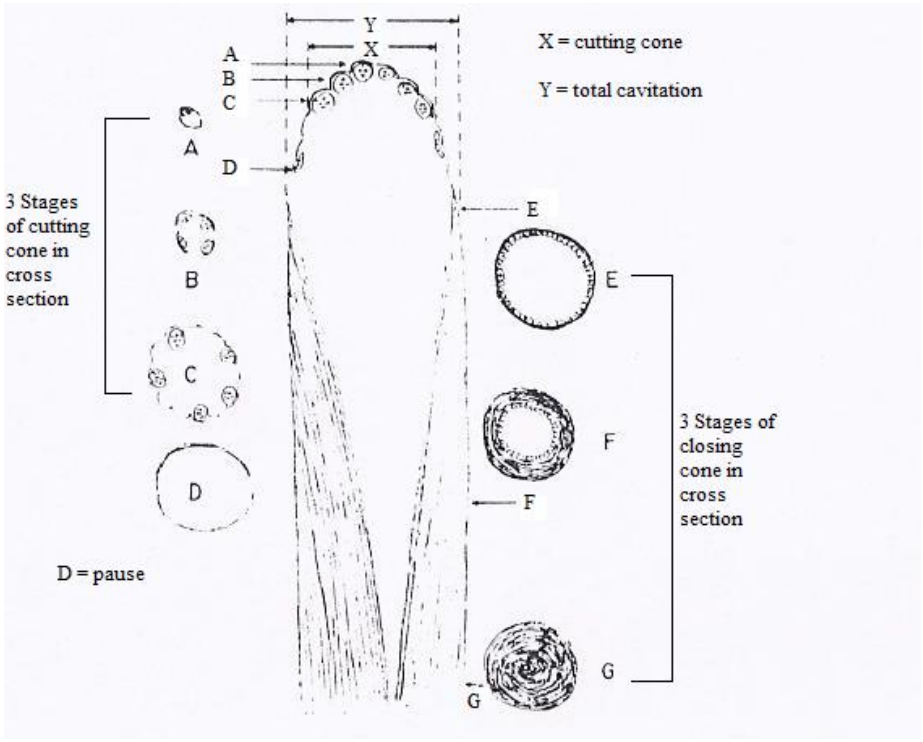

Figure 2.3. Schematic representation of cavitation and refill (latter named BMU by Frost[6]) by Lent Johnson. Adapted from Johnson.[55]

In the mid-20th century, a new era started for bone biology, and the modern concept of bone physiology can be attributed to Frost,[6] who, in 1969, developed a histomorphometric method to explore bone formational dynamics in several mammal species, including humans, using fluorescent tetracycline labels. With this method, Frost and coworkers were able to distinguish the

changes that occur in cortical bone; they also described three envelopes/surfaces: periosteal, Haversian (or intracortical), and endosteal. They coined the terms modeling and remodeling to refer to dynamic changes in bone tissue. They defined modeling as the resorptive and formative process that bone surfaces undergo during skeletal growth, and remodeling as the internal process by which bone is continually renewed by resorption and formation in the adult skeleton.[6] The former creates primary lamellae which may contain space that become primary osteons, whereas the latter creates secondary osteons. Frost divided remodeling into three fixed sequences: activation by an initial stimulus, resorption by osteoclasts, and formation by osteoblasts. He also defined remodeling as a process carried out by thousands of BMUs. It was only in the late 1970s that Roland Baron and colleagues, studying BMUs in the rat jaw, observed an intermediate phase (referred to by Johnson as a pause) between resorption and formation, which they termed the reversal phase.[12,57] This phase was characterized by the presence of mononucleated cells that they could not definitively identify as either post-osteoclasts (in the sense that they have re-emerged from osteoclasts in the cutting cone) or pre-osteoblasts (precursor cells to osteoblasts). Based on more recent discoveries, the remodeling sequence has been divided into four phases, as described in Chapter 1: activation, resorption, reversal, and formation. In 2013, Andersen et al. demonstrated that the mononucleated reversal cells are in fact osteoprogenitor cells.[58] A few years later, a follow-up study provided new insights into the cellular processes that occur during the reversal phase based on study of longitudinal sections of Haversian systems in human long bones, and they renamed it the reversal-resorption phase.[59] Details of this study are described in Section 2.2.2.

2.2.1. LER of BMUs

In the 1970s, the terms Haversian system, Volkmann's canal, and Howship's lacunae were well understood (they are still in usage today). Following Johnson's and Frost's work describing the cellular organization of BMU, more attention was given to the role of BMUs in disease states. In 1972, Jaworski and coworkers[60] studying cortical remodeling in adult individuals (healthy and diseased), noted the presence of two types of BMU resorption spaces that differed in morphology and mode of operation. They classified them as small and large cavities (Figure 2.4). They pointed out that the small cavities were outlined by Howship's lacunae and exhibited vascular resorption behavior as described by Jaffe.[53] In longitudinal section, their diameter varied between 40 and

105 µm (mean 64.5 µm) and in length between 135 and 275 µm (mean 221.8 µm). They also noted that the small cavities appeared to be more numerous in an older patient sample. Still, they could not make any age-related generalizations as the number of subjects was considerably small. The large resorption cavities were associated with secondary Haversian remodeling (BMU cutting cones) measuring longitudinally between 225 and 650 µm (mean 409.2 µm) in length, and between 155 and 245 µm (mean 187.5 µm) in diameter.

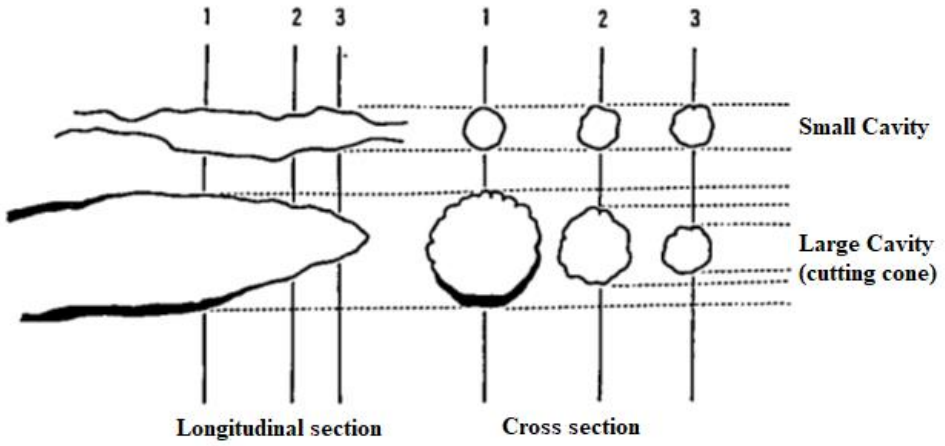

Figure 2.4. Schematic representation of the two types of BMU resorption spaces. Where on the top you can see a drawing of the small cavity, and on bottom the large cavity (BMU cutting cone). Adapted from Jaworski and co-workers.[60]

With Frost's tetracycline methodology, the mean thickness of new lamellar bone deposits was histologically measured directly and accurately in several mammal species.[6] On the other hand, the speed with which a BMU cutting cone resorbs bone could not be measured directly. Jaworski and Lok[24] developed a method based on tetracycline to measure bone dynamics in longitudinal sections of dog ribs. They labeled the bone of three dogs using two intramuscular injections, with a seven-day interval between them. The labels appeared in the longitudinal sections as two parallel bands on each side of the Haversian canal, as shown in Figure 2.5. They used two methods to infer the mean LER (µm/day), depicted in Figure 2.5.

In method one, a single animal (dog #3) underwent a double biopsy one day (biopsy one) and again eight days (biopsy two) after the second tetracycline label. When bone biopsies were

taken after labeling at intervals from the same subject, the proximal end of the second label in the longitudinal section marked the base of the cutting cone on the day of labeling. Because of the continuous advance of the cutting cones, with each subsequent biopsy, the second label was found further behind the cutting cones and separated from them by the non-labeled osteoid (segment O in Figure 2.5). The mean distance Z, from the tip of the cutting cones to the second label's proximal end, was measured within the two biopsies, where Z1 was from biopsy one and Z2 was from biopsy two. LER, the distance Y by t (Figure 2.5), was calculated as Z2-Z1/t, where t is the interval in days between biopsies one and two. In method two, Jaworski and Lok[24] used only a single biopsy (called biopsy one) that was double-labeled. The three dogs were biopsied after the second label, where dog #1 was biopsied at seven days, dog #3 at eight days, and dog # 2 at 11 days. They measured the length of the osteoid (O) formed after the second label, where O = Z – X, and divided it by the time interval between the second label and the biopsy day. According to method two (single biopsy), LER varied from 37 to 44.4 µm/days (mean 39.2 µm/day). Using methods one and two, the mean LERs from dog #3 were found to be very similar, with values of 36.7 µm/day and 37.3 µm/day, respectively. They also calculated the mean radial erosion rate (RER [µm/day]), that is, the mean speed with which each cutting cone enlarges from the tip to the maximal diameter at their base (segment D in Figure 2.5). The authors postulated that the cutting cone takes the same time to advance its whole length (X in Figure 2.5) as it expands laterally from the tip to its largest diameter. Therefore, the ratio of LER to RER must be equal to the ratio of the length of the cutting cone (segment X) to its radius (D/2) at the base. The mean RER was calculated as RER = (D x LER)/2X. Based on these calculations, the authors reported that RER varied from 6.2 to 7.8 µm/day (mean 7.1 µm/day).

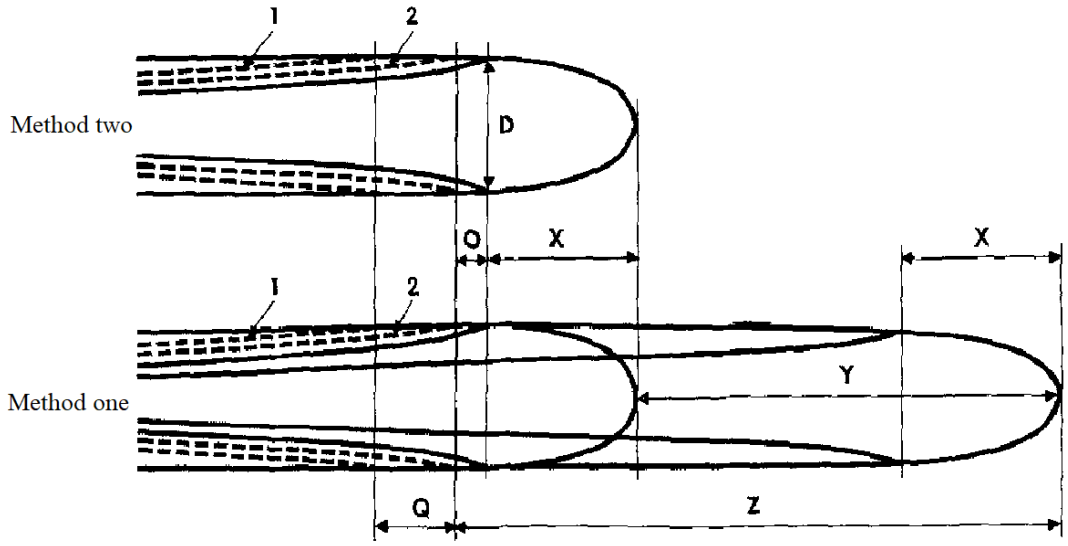

Figure 2.5. Schematic representation of a BMU illustrating method one and two from Jaworski and Lok to measure longitudinal erosion rate (LER). Where X: the length of the cutting cone, D: the diameter of the cutting cone, O: the length of osteoid seam after the second label, Z: the mean distance between the tip of cutting cones to the second label's proximal end, and Y: the distance which the cutting cones traverse during the time between two biopsies. LER was calculated as Y/t, where Y = Z2-Z1, and t is the time between biopsy one and two. Adapted from Jaworski and Lok.[24]

Following Jaworski and Lok,[24] Takahashi and Norimatsu[25] also quantified LER in the ribs of five dogs (Figure 2.6). They labeled the dogs using demethylchlortetracycline (a variant of tetracycline) injected daily for three days, and then, after a 17-day interval, they repeated the process. The animals were biopsied 14 days after the second label. LER was calculated as the mean distance between L1 and L2 (where L1 and L2 are the lengths of bone formed on each side of the BMU, between two labels, Figure 2.6) divided by 20 days (17-day time interval between the labels + 3 days of labelling). They considered that the mean bone-forming distance (L1 and L2) was correlated to the mean bone-resorbing distance (where H1 and H2 are the distances from the tip of the cutting cone (CC) to the second label, on each side of the BMU, Figure 2.6). They reported LER varying between 31.7 and 44.0 µm/day (mean 38.0 µm/day).

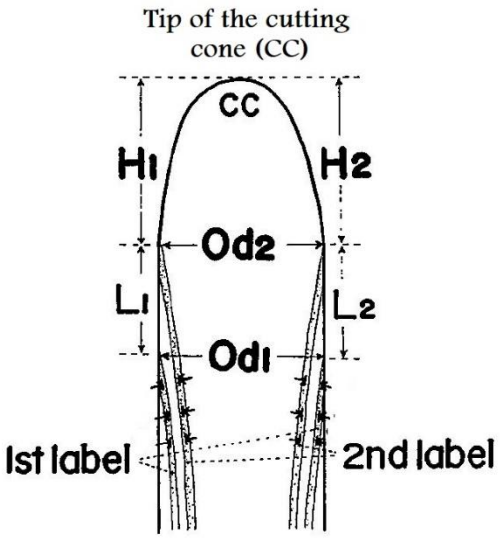

Figure 2.6. Schematic representation of a BMU by Takahashi and Norimatsu.[25] Where CC: cutting cone, H1 and H2: lengths between the tip of the cutting cone and the end of the second label, L1 and L2: lengths between the ends of the first and second labels of each side, Od1 and Od2: diameters of the osteon at the end of the first and second labels. Adapted from Takahashi and Norimatsu.[25]

In a third study, Jaworski and colleagues,[26] using the two methods developed by Jaworski and Lok,[24] measured LER and RER in uremic dogs and compared them with normal dogs. The length of the cutting cone and LER in the uremic dogs significantly decreased (from 310 µm to 225 µm, and 43.61 µm/day to 27.7 µm/day, respectively). However, cutting cone diameter and RER were not significantly reduced (D from 125 µm to 117 µm, and RER from 9.2 µm/day to 7.7 µm/day). They also calculated the segment Q (the length of bone deposited between the first and second label, Figure 2.7) and found it to be significantly decreased in uremic dogs (from 305 µm to 192 µm). A comparison of cutting cones from normal and uremic dogs, as well as humans, is shown in Figure 2.7.

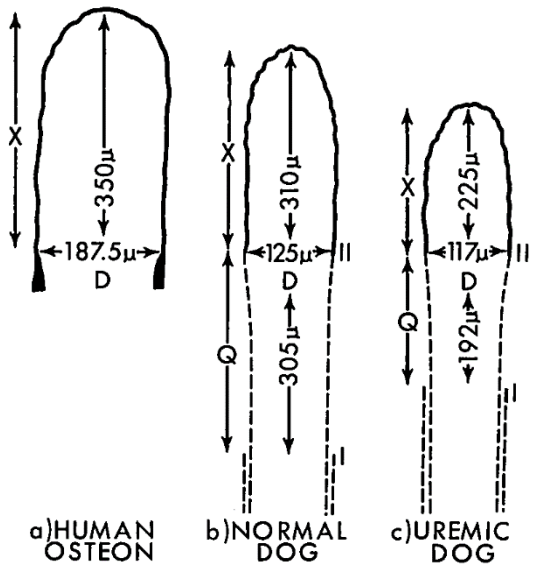

Figure 2.7. Measurement of cutting cone length and diameter (X and D, respectively) as well as the length of bone deposited between the fist and second label (Q) in: a) an adult human (male); b) normal dog; and c) uremic dog. From Jaworski and colleagues[26] with copyright permission to use.

In 1983, Parfitt[7] reported a very similar LER and RER for monkeys (36.7 μm/day and 6.2 μm/day, respectively) compared with Jaworski and Lok's[24] dogs (40 μm/day and 7 μm/day). However, Parfitt did not provide details about the monkey experiments, and he pointed out that the data were unpublished. In this work, Parfitt described what he called the "Geometric Relationship in Haversian Remodeling" presented in Figure 2.8, where R_1, R_2, and R_3 are the successive positions of the cutting cone corresponding to the cement lines C_1, C_2, and C_3, and H_3 is the boundary of the Haversian canal at timepoint 3. Parfitt postulated that in the time taken for a cutting cone to advance from R_1 to R_3, which is the length of the closing cone (LFC), new bone formation in the closing cone fills the distance between C_1 and H_3 (or the wall thickness of a completed osteon). In other words, the time of radial closure, σ_r, which can be calculated from 2D cross-sectional histology using dynamic labels dividing the wall thickness (C_1 to H_3) by On.MAR, matches the time to advance a full LFC. Assuming all these geometric relationships are constant, LER can be calculated as LFC/σ_r. In other words, if a closing cone fills more rapidly, the cutting cone must speed up if BMU geometry assumption is to be maintained. Moreover, Parfitt assumed that there is no delay between

completion of resorption and commencement of formation, and inclusion of constant delay would not alter the relationships between LER and σ_r.

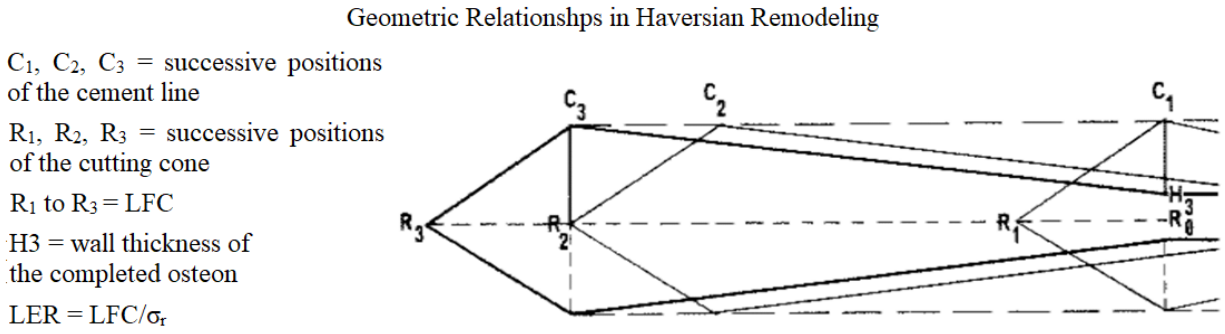

Figure 2.8. Parfitt's sketch of the geometric relationship in haversian remodeling. Where LER = LFC/σ_r. LFC: length of closing cone. σ_r: time of the radial closure. Adapted from Parfitt 1983.[7]

Overall, all these classical studies based on 2D longitudinal sections are essential to our fundamental knowledge of BMU dynamics as we know them today. However, Jaworski and Lok's method two, Takahashi and Norimatsu's study, and Parfitt's study were based on inferring LER from formation rates. They all assumed a set of geometric relationships considering the amount of bone formed equal to the amount of bone resorbed. Such a belief can be very problematic in diseases such as osteoporosis, particularly with new concepts of reversal phase arrest, and uncoupling between resorption and formation, in bone loss.[61] Indeed, one could argue that Jaworski and Lok's method one directly measured LER from cutting cones' advance using the mean values of two biopsies. However, the method suffers because LER could not be measured from the same BMU. With the new concepts in bone remodeling, it is crucial to know whether LER plays a role in BMU coupling. For example, could a lower LER improve the coupling and balance of BMU activities? Is a higher LER associated with uncoupling between formation and resorption? Another limitation in using 2D longitudinal sections to study BMUs is the difficulty of accurately positioning them as the sections rarely happen to be aligned parallel to the long axis of a BMU.[59] Ultimately, none of these methodologies has given a 3D picture of LER. These methodological issues led our group to explore image-based approaches to study cortical bone remodeling. The following section will discuss how BMUs were inferred as static in 3D serial

sections (histology) and the importance of 3D/4D imaging methodologies to quantify BMU dynamics.

2.2.2. Characterization of BMUs in 3D Studies

The first study of the 3D course of a Haversian system was performed by Cohen and Harris[62] in 1958 using the mid-femoral cortex of adult dogs. They cut bone samples into blocks and embedded them in celloidin. Then, they performed between 300 and 420 serial cross-sections (25–40 μm) and, using a phase microscope, photomicrographed each section. They then chose eight Haversian systems to trace and to reconstruct as a physical model by a time-consuming process.[62] They reported that the Haversian systems followed a spiral orientation but noted that this could be relevant only in the dog's femur because the number of segments in their study was insufficient for a confident generalization. They also pointed out the variance in the morphology of Haversian systems and their distribution, which was linked to specific sites within the bone.

In 1977, Tappen[63] studied resorption spaces in 3D and their continuation as fully developed Haversian systems, also using block staining and serial sectioning of decalcified long bone samples from dogs, baboons, and a human (male rib). By that time, the organization of BMU, including its resorption space, had already been described by Johnson[55] and Frost.[6] Tappen reported numerous features of Haversian systems and the remodeling process. For example, he described BMU resorption spaces as a continuum with Haversian canals and observed that they can tunnel in opposite directions from one another or in only one direction. Tappen recognized the new insights into pathological conditions that 3D serial cross-section studies could potentially offer clinicians compared with a single cross section or longitudinal section; however, serial sectioning is challenging and time consuming. Therefore, it was another 20 years before further work utilized this 3D approach. Robling and Stout[64] published a study in which they investigated drifting of BMUs in 3D. They found that a drifting BMU differs from the classic cutting and closing cone morphology. They also noted that drifting BMUs were more frequently observed in the bones of children. Ultimately, however, it was unclear to them what stimulus was involved in creating and guiding drifting BMUs. In the same year Stout and coworkers[65] performed a 3D digital analysis of Tappen's[63] original data. Their 3D image reconstruction did not support Cohen

and Harris's suggestion that Haversian systems had a spiral organization, but instead, they found a complex arrangement that was dominated by branching.

Lassen and colleagues[59] performed serial longitudinal sectioning in cortical bone samples from the femora and fibulae of patients who underwent surgeries from *coxa valga* and jaw reconstruction. Series of 20 to 60 adjacent (3.5 μm thick) sections were then studied to capture remodeling events from initiation of resorption to formation as a continuum (the classic cutting and closing cone shape). They found that tip of the cutting cone was followed by a period during which both reversal cells and osteoclasts were found, which they called this the reversal-resorption phase. The 3D results showed that the initial cutting cone (resorption phase) was mainly engaged in elongating the canal (LER), whereas additional events in the reversal-resorption phase were involved in widening it (RER), with the majority of the diameter of the resorption space being created by radial expansion. They also pointed out that the formation phase was linked to the density of osteoprogenitor cells and that bone formation is only initiated when this threshold (at least 39 cells/mm) is reached. They showed that the length of the reversal-resorption phase was dependent on how fast osteoprogenitors were recruited to reach the threshold, and thus, the slower the recruitment of osteoprogenitors, the more bone was resorbed. They concluded that the newly recognized reversal-resorption phase plays a central role in the coupling of resorption-formation phases.

Andreasen et al.,[66] using the same methodology as Lassen and colleagues,[59] studied the relationship between cortical vascular porosity and aging in women ranging from 16 to 78 years old with no evidence of metabolic diseases or drug treatment that could affect calcium metabolism. Their study showed that age-induced cortical porosity is related to increased pore size (widening) rather than increased pore density. They classified their finds into two types of pores: type I pores associated with remodeling events with the classic cutting closing cone tunneling into the cortex (creating a new pore) and type II pores associated with expansion of an existing pore (widening into a Haversian resorption space). They pointed out that aging and vascular porosity are associated with a shift from type I to type II pores. They concluded that increased cortical porosity related to aging results from the intracortical remodeling of existing vascular pores (type II) with an extended reversal-resorption phase (described by Lassen and colleagues[59]). The extension in the reversal-resorption phase could be linked to a delay of coupling (or uncoupling) of the resorption and formation phases. A delay in coupling between resorption and formation would make cutting cones

larger than the closing cones, making the assumptions of the classic LER studies even more problematic.

Although all these 3D studies have contributed to our understanding of the structural complexity of Haversian systems, it is important to point out that they are based on a static view of BMU morphology. As already described, the progression of BMUs has only been investigated by 2D longitudinal sections via dynamic histomorphometry of the formation phase (closing cone), drawing upon many assumptions. There is a gap in our knowledge regarding how BMUs are regulated over time, caused by the lack of efficient 3D methodologies. A better understanding of BMU spatio-temporal behavior can contribute to a better understanding of cortical bone remodeling in disease states, including osteoporosis. The methodological difficulties of 3D (serial section) histology ultimately led to the exploration of 3D and 4D imaging-based approaches to the study of cortical bone remodeling.

2.3. 3D Imaging of Cortical Bone Microstructure

With the advance in X-ray imaging technology in the later 1980s and beginning of the 1990s,[67] it was possible to image isolated bone samples in 3D using non-invasive/non-destructive X-ray micro-CT. The development of micro-CT scanners and algorithms by Feldkamp et al.[68] and Kuhn et al.[69] was the key step towards the 3D quantification of osteoporotic changes in trabecular bone microarchitecture.[67] For commercially available micro-CT scanners at that time, resolutions of 30 to 15 µm were typically used, rapidly making this technology the "gold standard" for studying osteoporotic changes in trabecular bone.[31] Cooper and coworkers[35] in 2003, pointed out the importance of choosing the right scan resolution if one is interested in studying cortical bone with micro-CT, especially vascular porosity in 3D. The length of resorption spaces sectioned longitudinally in human bone varies from 225 to 650 µm,[60] but human cortical pore size varies considerably across age, sex, and sampling site, and many vascular pores as small as 10 µm in cross-sectional diameter can be present in human bone.[35] Having that in mind, they used a high-resolution scanner (10 µm) to develop a method to quantify cortical bone microstructure in 3D based on the direct histomorphometric parameters from trabecular bone. Their method opened the door to further 3D cortical microarchitecture research.[27,35,70–77] For the study of remodeling, micro-CT is an excellent tool for the detection of BMU-related resorption spaces as the cutting

cones generally stand out from the smaller canals of completed Haversian systems (mean canal diameter reported in humans around 71 μm[78]). Cooper and colleagues[72] were the first to apply this technology to visualize the morphology of BMU-related resorption space in human cortical bone (Figure 2.9) and to quantify the distance transverse by it over time. The cohort studied included 82 human femoral midshaft samples from males and females, with ages ranging between 18 and 92 years old. Their results showed that the distance transverse by BMU-related resorption spaces did not differ between sexes and ages, and the mean value was in the order of 3,770 μm.[72] They considered that the mean BMU range measurement obtained in their study was an underestimate because in many cases BMUs extended beyond the field of view of the micro-CT scan, and thus could not be measured along their entire length. Regarding the morphology of spaces, their results showed several variations, including unidirectional, bidirectional, branched, and even highly clustered forms as identified by Johnson in 1964.

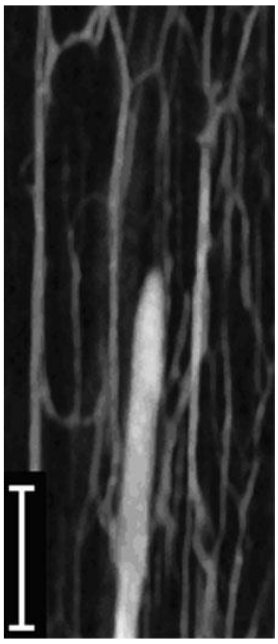

Figure 2.9. BMU-related resorption space in the cortex of a human femur. From Cooper and colleagues[72] with copyright permission to use.

Despite micro-CT's advantages of non-invasive/non-destructive 3D visualization, it has limitations. One of them is the fact that this technology remains largely limited to detecting porosity at the vascular level.[31] Synchrotron radiation (SR) micro-CT has many advantages over conventional micro-CT, such as greater flux of photons, higher brilliance, and coherence. With SR

it is also possible to focus the beam into a small size to visualize smaller-scale structures including osteocyte lacunae, microcracks, and Haversian system borders and thus their morphology.[31] Maggiano and coworkers used SR micro-CT to reconstruct Haversian system networks in 3D in human cortical bone to study aged-related changes.[79] They found two types of branching morphologies: lateral and dichotomous branching (Figure 2.10). The lateral branching was characterized by a newly formed canal that connects the Haversian canal of a previously existing Haversian system with adjacent tissue, where it extends through the formation of a new BMU. The dichotomous branching was a result of the formation of two new osteonal branches from one. Regarding age-related changes, their results showed that in younger individuals, transverse connections were most common. On the other hand, in older individuals, they found that the connections more frequently resulted from new Haversian systems growing inside previously existing systems (or the type II pores as observed by Andreasen et al.[66]).

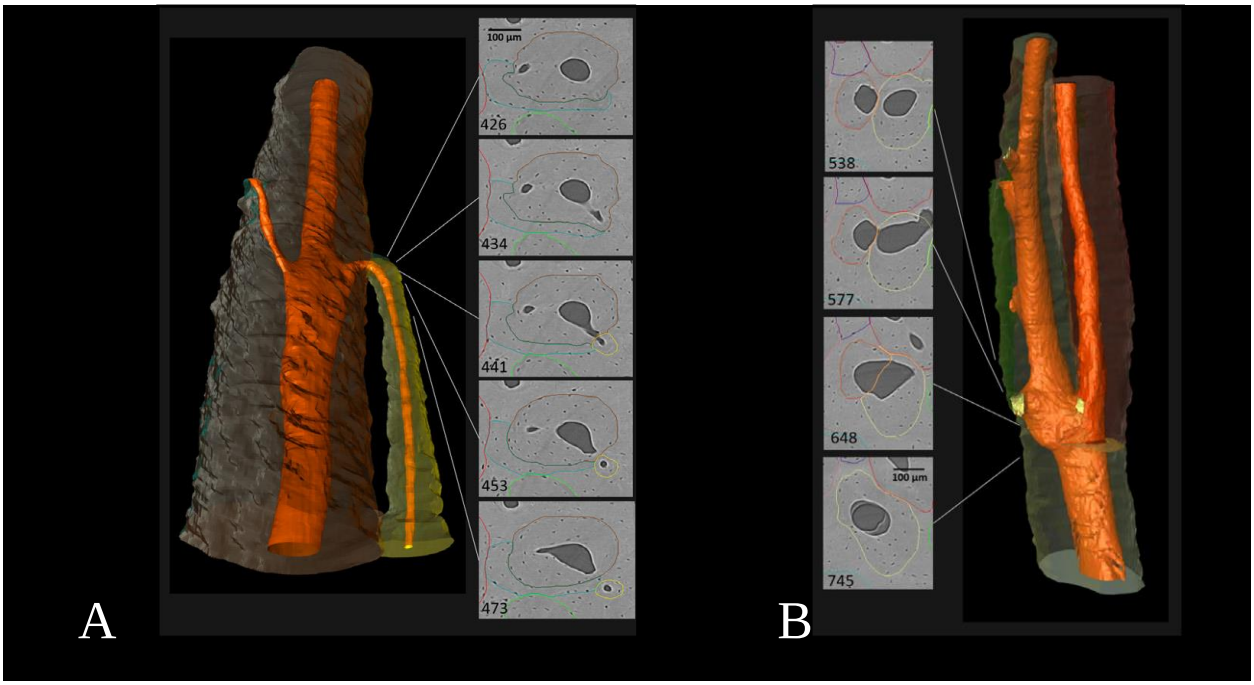

Figure 2.10. (A) Haversian canal and its lateral branching. (B) Haversian canal with dichotomous branching resulting in two osteonal branches. From Maggiano and co-workers[79] with copyright permission to use.

Even though we have gained a lot of new knowledge regarding the 3D morphology of Haversian systems, there is still a lack of knowledge regarding BMU dynamics in 4D. To detect and track BMUs, one must turn to *in vivo* imaging. In clinical studies, high-resolution peripheral quantitative computed tomography (HR-pQCT) has been used for the *in vivo* characterization of human bone in 3D since its commercially availability beginning in the mid-2000s.[34] HR-pQCT is non-invasive, and it employs a low radiation dose for assessing bone microarchitecture in cortical and trabecular tissue of the distal radius and tibia. This technique uses a standard measurement protocol with an in-plane voxel size of 82 μm and 61 μm in first- and second-generation scanners, respectively.[35] Whereas the reconstructed images have a voxel size of 61 to 82 μm, the actual spatial resolution of the images ranges from 92.5 to 154 μm (130 μm near the center of the field of view).[80] Consequently, structures less than 100 μm in scale are not typically resolved. Considering that the mean canal diameter in human cortical bone varies between 56 and 456 μm, and many cortical pores diameter are around 10 μm, this technique cannot resolve all canal sizes, and it is limited to the largest cortical pores.[35,70] One way to overcome this limitation is by increasing image resolution. However, there is a cost in terms of radiation dose. Increasing the scan resolution by factor of two increases the radiation dose employed by factor of 16 if image quality is to be maintained, with all else kept equal.[36] This limitation holds for not only the use of HR-pQCT in *in vivo* human studies but also the use of conventional micro-CT and SR micro-CT for preclinical (animal) models, as all these techniques develop contrast based on the absorption of X-rays. However, because of the monochromatic capabilities of SR, it is possible to perform micro-CT scans based on phase contrast instead of absorption. Micro-CT images are based on the differences in X-ray absorption related to the sample's internal structure that is being imaged; on the other hand, phase-contrast images exploit differences in the refractive index of the sample to differentiate the small differences in density within a sample.[81] In other words, the differences in refractive index of the sample will refract the X-ray photons as they pass through the sample and these differences can be used to generate contrast. Some examples of phase-contrast imaging applied to biomedical studies are in-line phase-contrast imaging, diffraction-enhanced imaging, and interferometer-based imaging.[32,81,82] The simplest of these techniques to implement is in-line phase, where the detection of the differences in the X-ray refractive indices of the sample can be optimized by altering the distance between the samples and the X-ray detector.[31] Our group has established the feasibility of synchrotron in-line phase-contrast micro-

CT to image cortical porosity in rats with radiation doses comparable to those used in *in vivo* imaging of trabecular bone.[32] In this preliminary work, *ex vivo* imaging, and dosimetry measurements were employed to optimize and implement an *in vivo* protocol using rats as a model. SR micro-CT images were compared against conventional micro-CT protocols and their related doses (Figure 2.11). The results showed that SR micro-CT was superior in the detection of cortical pores without a substantial increase in dose (voxel size of 11.8 µm and radiation dose of 2.53 Gy) compared with the laboratory source (voxel size of 18 µm, and radiation dose of 1.2–1.5 Gy; voxel size of 9 µm, and radiation dose of 11.7–18.2 Gy). A second step was towards tracking of individual remodeling events *in vivo*. The first trial was performed using rat forelimbs (Figure 2.12).[31] The two micro-CT scans were taken two weeks apart from each other, and it was possible to track a change in the same BMU-related resorption spaces (from image A to B [red rectangle]). A limitation in this study is the fact that the rats showed very little remodeling (few, if any, BMUs). Nevertheless, this methodology can be applied to a larger animal model than rats, such as rabbits, which are well known in the literature to exhibit cortical remodeling. However, for a rabbit model to be fully operational with many remodeling events to be studied, it is necessary to increase the activation of BMUs. Human PTH is well documented in increasing cortical porosity in rabbits. Our group has recently studied rabbit-based models of osteoporosis and compared them with a PTH rabbit model.[27] The results showed that cortical porosity was substantially elevated in PTH rabbits relative to all other rabbit-based models of osteoporosis, and this was associated with an increased remodeling rate and cortical pore size (Figure 1.3).

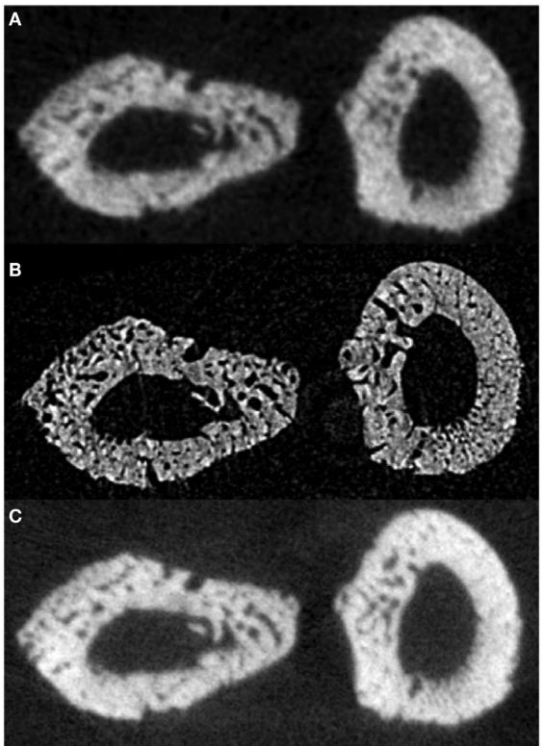

Figure 2.11. A) in vivo laboratory SkyScan 1176 micro-CT (18 μm, 1.2–1.5 Gy dose), (B) in vivo SR micro-CT (11.8 μm, 2.53 Gy dose), (C) in vivo laboratory micro-CT (SkyScan 1176; 9 μm, 11.7–18.2 Gy dose). Image from Pratt and colleagues[32] with copyright permission to use.

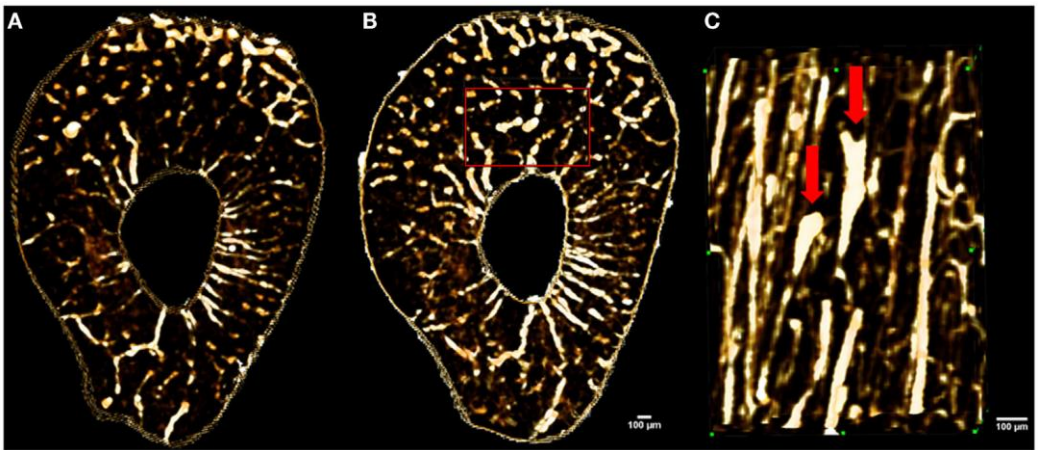

Figure 2.12. Images showing in vivo matched scans of a rat forelimb acquired with SR micro-CT (11.8 μm, 2.53 Gy). Scan (B) was carried out two weeks after scan (A) on the same rat's forelimb. Image (C) is an enlarged section of image (B) (red rectangle) displaying new remodeling events (red arrows). Image from Harrison and Cooper[31] with copyright permission to use.

Using the PTH rabbit model associated with longitudinal *in vivo* synchrotron-based phase-contrast micro-CT, we developed an imaging model capable of directly tracking remodeling events in 4D (3D over time).[37] In this thesis research, I used the same PTH protocol as described in our previous work, where the rabbits were dosed at 30 μg/kg/day.[27] LER was assessed for 185 BMUs from 12 rabbits showing a mean value of 23.79 ± 1.83 μm/day. This methodology is described in Chapter 3 with full details.

As mentioned in Chapter 1, in this thesis, I am using this novel approach to obtain new insights into **how PTH affects spatio-temporal BMU regulation.** In the next section, I provide an overview of how PTH affects cortical and trabecular bone remodeling, and more importantly, how PTH might affect LER as proposed in my hypothesis.

2.4. Effects of PTH in Cortical and Trabecular Bone

PTH, an 84-amino-acid peptide hormone (or PTH 1-84), is produced by the parathyroid glands and is essential for the maintenance of an appropriate calcium balance in the bloodstream, regulating bone remodeling.[83] At the BMU level, PTH increases the rate of remodeling as measured by activation frequency (Ac.f [1/mm^2/yr]), in other words, the number of new BMUs (or remodeling events) being initiated per unit area in a given time.[27] Takahashi and coworkers[84] described the impact of PTH as involving first an increase in the number of osteoclasts and consequently an increase in the number of resorption surfaces. Because resorption and formation are coupled,[85] the increased bone resorption is associated with an increase in bone formation, which was clearly shown by the correlation between osteoclast number and the osteoblastic surfaces found in their study.[86] At the cellular level, PTH favors bone resorption indirectly through the osteoblast. First, PTH binds to its receptor, PTH receptor 1 (PTHR1), on stromal/osteoblastic cells and thereby increases production of the RANKL.[19,87] Second, RANKL binds to its receptor RANK on the hemopoietically derived pre-osteoclasts. This interaction is essential for osteoclast recruitment, differentiation, and activation.[19] Communication between RANK and RANKL can be inhibited by the decoy receptor osteoprotegerin (OPG), and thus, ultimately, the RANKL:OPG ratio will modulate the degree of osteoclast differentiation and activation. Conversely, PTH increases both osteoblast proliferation and survival, thus increasing bone formation.[19] By acting directly on osteoblasts and indirectly on osteoclasts[88], PTH has a

double effect on bone metabolism: catabolic and anabolic. The catabolic effect was first observed in primary hyperparathyroidism (PHPT) patients, where an individual exposed to continuously high amounts of circulating PTH presents with secondary osteoporosis.[19,87] In symptomatic PHPT patients, osteoporosis was only diagnosed in the past after a bone fracture. With the advance in the diagnosis of osteoporosis in the 1980s by dual-energy X-ray absorptiometry (DXA), more insights were possible into the skeletons of subjects with PHPT.[19] Studies were performed by measuring bone mineral density (BMD) at different skeletal sites and histomorphometry of biopsies from the iliac crest.[89] Some studies conducted in the 1980s showed a catabolic effect of PTH in cortical bone, with a greater reduction of BMD,[89,90] and other investigations found an equivalent or even greater deficit in trabecular bone.[91,92] Parisien et al.[93] conducted a histomorphometric study of iliac crest biopsies from 27 patients with mild PHPT. The results showed that cortical thickness (Ct.Th, µm) was significantly lower in PHPT patients than in controls, whereas total bone density (TBD, %) was not significantly different between the two groups. In trabecular bone, bone volume fraction (BV/TV, %) and trabecular number (Tb.N, 1/mm) were significantly higher in PHPT patients. Trabecular separation (Tb.Sp, µm) was significantly lower in PHPT patients than controls, whereas trabecular thickness (Tb.Th, µm) was not significantly different between PHPT patients and controls. They concluded the study by stating that PTH could have a protective effect on trabecular bone. Several other studies since have shown that trabecular bone microarchitecture is preserved in patients with mild-PHPT.[94–97] Dempster et al.[98] extended the histomorphometric analysis of iliac crest biopsies from patients with mild PHPT to 3D analysis using micro-CT. They concluded that trabecular bone microarchitecture was also preserved in patients with mild PHPT.

The anabolic effect of PTH was first noted in 1923 by Bauer, Aub, and Albright.[99] Using parathyroid extract (PTE) in growing rats (8 U/day), they found an increased number of trabeculae, but they did not comment on the significance of the finding.[100] More convincing evidence of PTE's anabolic effect was obtained by Selye[101] and Pugsley and Selye.[102] In both studies, there was an increased proliferation of osteoclasts and osteoblasts using a single injection of 20 U PTE in rats. With continuous treatment, an increase in bone tissue and decrease in the number of osteoclasts was observed. They also noted that the treatment with a lower dose (5 U on alternative days) led to proliferation of osteoblasts only. Jaffe[103] and Burros[104] also conducted studies using similar small doses of PTE and confirmed Selye's results on the stimulation of osteoblasts.[100] The anabolic action of PTH was then confirmed in the 1970s,[100] and the first small uncontrolled

clinical trial (four patients) was conducted using low doses of a fragment of PTH, the first 34 amino-terminal acid (PTH 1-34) to treat osteoporosis in postmenopausal women for six months.[105] The results showed increased calcium isotope incorporation in the skeleton after PTH (1-34) treatment. In a multicenter trial in 1980, 21 patients with osteoporosis were also treated with PTH (1-34; daily dose of 100 μm) for six to 24 months. They found a substantial increase in iliac crest BV/TV (70 % above the baseline). They concluded that the PTH fragment 1-34 could be useful to treat patients with crush fracture syndrome.[106]

The paradox of the dual catabolic and anabolic actions of PTH remained a puzzle for a long time, until experiments using dogs and rats suggested that the difference could be related to the modes of PTH administration.[100] Podesek et al.[107,108] performed two separated studies using PTH (1-34) in dogs. Daily injections (15 U/kg/day) were compared with continuous infusions (4.5 U/kg/day). The daily dose increased bone formation and resorption, and BV/TV in the iliac crest. The authors used a daily dose similar to that used in a human study,[107] where the changes in bone parameters were very similar to their findings.[100] Tam and coworkers[109] performed their studies in rats with different doses of bovine PTH (1-84) and different regimens (daily and continuous). With both methods of administration, bone formation surfaces were increased, but resorption was only increased with PTH administered continuously. They noted an increased net result in trabecular bone by daily injection of PTH. A low dose administered continuously maintained BV/TV, but the high dose caused a decrease.[100] These observations were confirmed ten years later by Hock and Gera.[110] They also used rats as their animal model and concluded that both modes of PTH administration increased bone formation, but only intermittent daily dosing of PTH increased bone mass consistently.[100] A definitive clinical trial was conducted in postmenopausal women from 99 centers in 17 countries between 1999 and 2001.[111] The 1637 patients with prior vertebral fractures were treated with 20 or 40 μg of PTH (1-34) by subcutaneous injections daily. The results showed a decrease in the risk of vertebral and nonvertebral fractures and an increase in femoral, vertebral, and total body BMD. Regarding the doses, they found that 40 μg increased BMD more than 20 μg did, but both doses had similar effects on the fracture risk. These results led the US Food and Drug Administration to approve PTH (1-34) for use in osteoporosis in November 2002.[112,113]

The significant anabolic effects of PTH in trabecular bone were well established; however, its effects on cortical bone in humans were less clear. Studies in osteoporotic patients between

1980 and1990, showed that cortical bone mass decreased after treatment with PTH,[114–116] and the suggestion at that time was that the increase in trabecular bone was at the expense of cortical bone.[114] This catabolic effect on cortical bone provoked the curiosity of researchers who were starting to investigate this effect using rats as an animal model.[117–121] Controversially, their results showed an increase in the mechanical strength, thickness, and mass of cortical bone, and most of the PTH response was limited to the periosteal and endosteal surfaces. Rats do not normally undergo cortical remodeling, and therefore they could not show the effect of PTH on the intracortical envelop.[38] Other animals that exhibit cortical remodeling, such as ferrets, monkeys, dogs, and sheep, were used to investigate PTH effects on cortical bone.[122–126] However, the sample sizes of these studies were considered too small for a significant statistical analysis. Hirano and colleagues[30] decided to investigate the effects of biosynthetic PTH (1-34) in remodeling of cortical bone in rabbits. They pointed out that rabbits are the smallest animals that form Haversian systems by intracortical remodeling. In their study, mature New Zealand white rabbits were treated with once-daily injections of PTH (1-34) at 10 μg/kg/day or 40 μg/kg/day for 140 days. Their results showed that intracortical bone remodeling in the rabbits' tibia was activated and increased by eight-fold with the lower dose and 24-fold with the higher dose. Cortical porosity (associated with the number of BMUs) also increased using both doses. This increase was paralleled by increases in bone formation rates at the periosteal (Ps.MS/BS) and endocortical (Es.MS/BS) surfaces, as well as osteonal mineral apposition rate (On.MAR) at the intracortical surface. A second study was carried out by the same group[39] using the same biosynthetic human PTH (1-34) at a lower dose of 10 μg/kg/day for 35 and 70 days. They aimed to study if cortical porosity increases before the changes in cortical geometry. The results showed that at 35 days, the number of resorption cavities and activation frequency were significantly greater compared with the control group, and by 70 days, these parameters remained significantly elevated. Bone formation rates at the periosteal and endosteal surfaces were increased after 70 days; however, no difference was found in On.MAR in the intracortical surface by 35 or 70 days. Although intracortical remodeling increased in this study, they concluded that it did not affect cortical bone mechanical strength. As it was well established that PTH daily dosing was associated with an increase in porosity in cortical bone, Zebaze and coworkers[127] decided to investigate if a weekly dose of PTH would be beneficial to patients with structural deterioration and increased cortical porosity. They treated 17 female New Zealand rabbits aged six months for one month with PTH (1-34), divided

into five groups: (i) 20 µg/kg once daily, (ii) 40 µg/kg once daily, (iii) 140µg/kg once weekly, (iv) 280µg/kg once weekly, and (v) control. Both daily and weekly doses were comparable with the dose used clinically. They micro-CT scanned the femoral cortex (at 15 µm voxel size), and their results showed that the daily dose was associated with an increase in porosity, and the high daily dose (40 µg/kg) increased porosity five-fold. Both weekly doses were not associated with increased porosity. They concluded that the catabolic effect of intermittent PTH in cortical bone depends on the dose and frequency of administration. Yamane et al.,[128] using the same animal protocol from Zebaze and coworkers,[127] quantified not only cortical porosity but also the dynamic histomorphometric parameters. Their results showed that the daily, but not weekly, administration of PTH stimulated periosteal bone formation, and the weekly PTH regimens promoted well-organized endosteal bone formation. Cortical porosity was increased by the daily, but not weekly, PTH doses.

As mentioned in Chapter 1 (Figures 1.3 and 1.4), our group recently published a study of rabbit models of osteoporosis (ovariectomy [OVX], glucocorticoids [GC], and OVX + GC) and compared cortical remodeling and porosity in these models with that induced by PTH.[27] The PTH group was dosed by daily injections of PTH (1-34) at a concentration of 30 µg/kg for 4 weeks. The PTH dose used was intermediate to what was used by Hirano and colleagues.[30] The distal tibia was micro-CT scanned using a resolution of 10 µm (voxel size). We observed an increase in cortical porosity in all groups, but PTH had the most pronounced difference (Ct.Po = 28.8-fold increase). The PTH rabbits also showed a dramatically elevated activation frequency (Ac.f = 14.2-fold increase), with increases in periosteal and endosteal bone formation and On.MAR at the intracortical surface (Ps.MS/BS = 2.6-fold, Es.MS/BS = 3.6-fold, and On.MAR = 1.4-fold, respectively). In a second PTH trial by our group, LER was directly quantified for the first time, as mentioned in the previous section. The rabbits were dosed with the same PTH protocol used in the previous study.[37] The animals' right tibiae were imaged *in vivo* by synchrotron-based phase-contrast micro-CT halfway through the protocol (at 14 days) and then *ex vivo* (post-mortem) by conventional micro-CT at the end of the protocol (at 28 days). Results showed that cortical porosity between *in vivo* and *ex vivo* scans varied from 2.93% to 6.94%, and these values aligned with the preceding *ex vivo* study by our group[27] and also with the values reported by Zebaze and coworkers[127] and Yamane et al..[128] Notably, in our first trial involving PTH, we observed increased periosteal and endosteal bone formation, as well as Ac.f and On.MAR, as also reported

by Hirano et al.,[30] Mashiba et al.,[39] and Yamane et al..[128] None of these works had yet studied the impact of PTH on LER, with our second trial being the first to use 4D images to quantify it. Our studies and others showed that PTH increases remodeling rates and thus the number of BMUs available to be studied. These studies also showed that PTH increases On.MAR at the intracortical surface, reducing the radial closure (σ_r) time. All of the classic LER studies linked the rate of bone formation with that of resorption with Parfitt most explicitly postulating that LER could be calculated as LFC/σ_r (Section 2.2.1). Because PTH shortens σ_r, then PTH should directly impact LER advancement, making it higher than LER in a normal state.

2.5. Conclusion

There is a gap in our knowledge regarding how BMUs are regulated in space and time that is a result of the lack of 3D (spatial), let alone 4D (spatio-temporal), methodologies. The limited LER data reported in the literature were published almost 50 years ago, and they only provide 2D information of a 3D living system that changes over time. Our group has recently developed a method using longitudinal *in vivo* synchrotron-based phase-contrast micro-CT in association with a PTH rabbit model.[37] This methodology has a great potential to serve as a platform for more detailed analyses of how PTH affects spatio-temporal BMU regulation. Moreover, this new methodology can yield new insights into how PTH impacts LER, which has significant clinical relevance in understanding PTH's complex actions, this could, in turn, lead to strategies to improve responsiveness to PTH therapy. Therefore, in this thesis, I explore BMU behavior in 4D in cortical bone of rabbits using PTH to increase cortical bone remodeling rates and thus the number of BMUs available for study. Based on the classical LER studies, as discussed, I hypothesize that PTH causes a concomitant increase in LER due to increased anabolic activities in BMU. This hypothesis will be tested via a PTH versus PTH withdrawal (PTHW) study presented in detail in Chapter 3.

CHAPTER 3. PTH Reduces Longitudinal Erosion Rate of Basic Multicellular Units during Cortical Bone Remodeling

This chapter presents a manuscript entitled "PTH Reduces Longitudinal Erosion Rate of Basic Multicellular Units during Cortical Bone Remodeling" that is to be submitted to the Journal of Bone and Mineral Research (JBMR). This manuscript aims to describe the methodology used to quantify LER in 4D and how PTH can impact BMU progression. This chapter is formatted following JBMR's guidelines for manuscript submission. Researchers who contributed to this manuscript as co-authors include Kimberly Harrison, Beverly Hiebert, Gavin King, Kurtis Swekla, Ning Zhu, Peter Pivonka, Terra Arnason, and David Cooper. I was engaged in all aspects of this work, including the animal protocol, *in vivo* and *ex vivo* imaging, image processing, and data analysis, as well as the writing of this manuscript.

3.1. Introduction

The adult skeleton is continuously renewed to maintain its structure and integrity by a process known as bone remodeling.[10] Remodeling is a cyclic process, coordinated in time and space by a complex arrangement of cells first defined by Frost as basic multicellular unit (BMU),[6] although Lent Johnson[55] had previously described the same structure in 1964. BMU has been classically depicted as an elongated cylindrical structure comprising a cutting cone of osteoclasts resorbing bone matrix, followed by a reversal phase and, finally, a closing cone lined by osteoblasts behind forming new bone (Figure 1.2).[7,55] Recent research has modified this classical view, revealing that the initial cutting cone created by densely packed osteoclasts is followed by a zone of secondary resorption conducted by scattered osteoclasts intermixed with reversal/osteoprogenitor cells, and it was postulated that once a threshold of osteoprogenitor cell

density is reached, bone formation is initiated and resorption is switched off.[59,66] Thus, the reversal phase is now known as the reversal-resorption phase.[12,59] In young healthy individuals, resorption and formation are coupled and balanced within BMUs.[10,85] Coupling refers to the coordination of activities, in time and space, of osteoclasts and osteoblasts in each BMU, whereas balance refers to the net amount of bone tissue resorbed and formed. With aging or following menopause, BMUs deposit less bone than they resorb, leading to reduced bone mass.[11,13] This reduction in bone mass can be the result of either a negative balance between resorption and formation or a coupling defect (uncoupling), where the remodeling cycle is aborted, leading to a prolonged resorption-reversal phase that does not progress to the formation phase, creating an extreme case of imbalance.[10,11,58,61,85] Osteoporosis, which arises from summed bone loss across a multitude of BMUs, affects 200 million people worldwide, and the associated expenses to treat resulting fractures cost billions of dollars annually, placing a significant burden on health care systems.[129] The standard treatment for osteoporosis is based on antiresorptive agents such as bisphosphonates and denosumab that act on osteoclasts, inhibiting bone resorption and increasing bone mineral density (BMD).[15,16,18] Nevertheless, because resorption and formation are coupled within BMUs, inhibiting resorption also inhibits formation. Therefore, the increased BMD induced by such treatments occurs due to the mineralization of existing bone and not by an increase in bone formation. Thus, antiresorptive agents cannot reverse bone tissue deterioration.[16] Furthermore, such therapies are associated with adverse side effects, with rare but serious potential of osteonecrosis of the jaw and atypical fractures.[130,131] Teriparatide, a parathyroid hormone (PTH) analog (1-34), is an anabolic agent offering an alternative treatment for osteoporotic patients.[112] Intermittent PTH administration stimulates bone formation by increasing osteoblast numbers and preventing osteoblast apoptosis, therefore prolonging the time spent performing their matrix-synthesizing function.[132] PTH is an effective treatment; however, it is more expensive than antiresorptive agents[133] and its clinical administration is limited to two years, as it is associated with osteosarcoma in rats exposed to a high dose over two years.[22]

The best therapy for patients with osteoporosis or those at risk of developing the disease would entail improving coupling and balance between resorption and formation within individual BMUs. Modulation of remodeling, rather than its elimination (as achieved by antiresorptive agents), represents a better strategy to prevent and potentially treat osteoporosis. PTH has offered an anabolic alternative, but it has complex actions affecting both bone formation and

resorption.[19,27] For example, PTH has been shown to increase bone formation on trabecular, endosteal and periosteal surfaces while significantly increasing intracortical porosity.[20,27,30,127,128,134,135] The latter can be attributed to an increased remodeling rate (activation frequency; Ac.f) as observed in human[29] and animal studies.[27,30,125,136,137] Consistent with its anabolic actions, PTH has also been shown to increase intracortical bone formation, elevating osteonal mineral apposition rate (On.MAR).[28,29] Further studies of PTH's direct impact on BMUs could ultimately help improve treatment regimens – maximizing formation and minimizing resorption while potentially reducing side effects. Despite ongoing advancement in knowledge of BMU morphology at the cellular level, still little is known about BMU dynamic spatio-temporal regulation. The rate of progression of BMUs, their longitudinal erosion rate (LER), is a key example where our knowledge is lacking. Indeed, the limited information we have is from studies conducted in the 1970s and '80s, which indirectly assessed LER using double fluorochrome labeling combined with 2D histomorphometric analysis.[7,24–26] Jaworski and Lok[24] were pioneers of this approach, assessing LER in longitudinal sections of dog ribs via two different methods. In the first, the authors measured the mean distance from the tip of the cutting cones back to the second fluorochrome labels in two biopsies taken seven days apart, and LER was calculated as the difference in these mean distances divided by the time (Figure 3.1). In the second method, they inferred LER by the amount of osteoid formed after the second label by the time between the second label and the biopsy (Figure 3.1). Takahashi and Norimatsu,[25] inferred LER from dog ribs by the amount of bone formed between two labels by the time between them. In the latter two methods (Jaworski and Lok's[24] second method and that of Takahashi and Norimatsu[25]), it is assumed that the advance of the cutting cone matches that of the closing cone. Parfitt[7] took this assumption of a steady state a step further. He postulated that in the time it takes for a BMU to radially fill from the start of the closing cone, the closing cone must advance the equivalent of its original length. LER could thus be calculated as the length of the closing cone divided by the time required for radial closure (Figure 3.1). Histologically, this radial closure time can be calculated from osteonal wall thickness (µm) divided by On.MAR (µm/day). Should these spatio-temporal

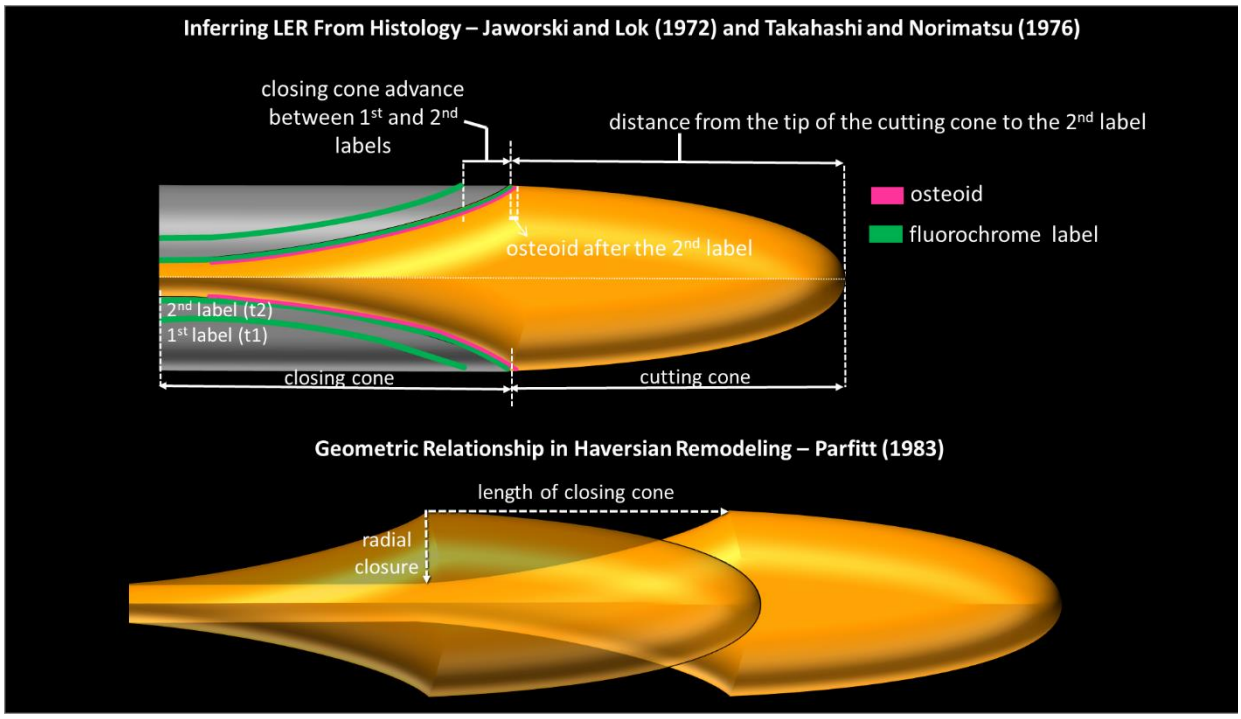

Figure 3.1. The classic BMU cutting and closing cone morphology (without the new reversal-resorption zone[59,66]). Top: Jaworski and Lok,[24] and Takahashi and Norimatsu[25] methods in classical studies for inferring longitudinal erosion rate (LER) from fluorochrome labeling. Jaworski and Lok measured LER using two methods. In the first, LER was calculated as the difference in the mean distance from the tip of the cutting cones back to the second fluorochrome labels in two biopsies (taken from the same animal) divided by the time between biopsies. And in the second method, by the length of osteoid formed after the second label by the time between the second label and the biopsy. Takahashi and Norimatsu inferred LER as the length of the closing cone advance between the first and second labels by the time between the labels (where t = t1-t2). On the bottom, Parfitt's[7] geometric relationship for inferring LER as the length of the closing cone divided by the time of radial closure (or radial infilling = osteonal wall thickness (µm) divided by On.MAR (µm/day).

relations be valid and constant, then increasing On.MAR, as observed with PTH dosing,[27–30] for example, would concomitantly elevate LER. That said, the validity of the assumed relationship between the activities of the closing cone and the rate of advance of the cutting cone is uncertain and questionable on several grounds, not the least of which is the high degree of variation evident

in the data of Jaworski and Loki[24] and Takahashi and Norimatsu.[25]Recent evidence of more complex BMU dynamics, including the presence of a reversal-resorption zone and even uncoupling of formation from resorption further undermines the assumptions underpinning these classical analyses. Due to a lack of direct assessment, it is unclear how and why LER might vary and its potential role in BMU dynamics including effects on coupling and balance. For example, does possible variation in LER impact the time required to reach the postulated cellular density[59,66] and thereby impact the size of the reversal-resorption zone? To help shed new light on such questions, we have recently developed a new methodology to quantify LER in 4D (3D over time) using *in vivo* synchrotron-based phase-contrast micro-CT imaging combined with a PTH rabbit model.[37] Rabbits are the smallest common laboratory animal that exhibits cortical remodeling similar to humans, and PTH is well known to increase cortical remodeling rate (Ac.f),[27,30] On.MAR,[27,30,39] and porosity[27,30,39,127,128] while also stimulating bone formation on trabecular,[27,30] endosteal,[27,30] and periosteal[27,30] surfaces in rabbits. In this study, we utilize this new methodology to explore whether the increased cortical remodeling activity induced by PTH, including accelerated On.MAR, leads to elevated LER as postulated by classical studies. Specifically, we aimed to manipulate BMU progression via different dosing regimens - PTH and PTH withdrawal (PTHW). We hypothesized that LER would be higher during active dosing as PTH increases bone formation rates.

3.2. Materials and Methods

3.2.1. Animal protocol

The animal protocol was reviewed and approved by the University of Saskatchewan's University Animal Care Committee and adhered to the Canadian Council on Animal Care (CCAC) guidelines for humane animal use. University veterinarians were directly engaged in the development of the protocol. Skeletally mature, six-month-old (3.4-3.9 kg), female New Zealand white rabbits (14 animals in total) were acquired from a commercial supplier (Charles River Laboratories, Quebec, Canada). The rabbits were housed individually in stainless steel rabbit racks in the Laboratory Animal Services Unit in the University of Saskatchewan. The room temperature (20–22 ºC) and humidity (40–60 %) were controlled by a computerized system, and the light cycle

was maintained at 12 hours of dark and 12 hours of light. The animals had free access to food, 18% rabbit pellets fortified with vitamins (Vitamin A (min) 15,000 IU/kg, Vitamin D (min) 6,000 IU/kg and Vitamin E (min) 150 IU/kg) and minerals (Calcium (act) 1.0%, Phosphorus (act) 0.7%, Sodium (act) 0.3% and Selenium at 0.3 mg/kg). More details of the rabbit pellets can be found elsewhere (https://www.trouwnutrition.ca/en-ca/product-lister-high-pro/18-rabbit-pellets-38713-Hi-Pro Feeds, Trouw Nutrition Canada Inc., Sherwood Park, Canada). The Rabbits were hydrated through an automated watering system (*ad libitum*). The rabbits were acclimatized for seven days before starting the PTH dosing period and weighed at the end of acclimatization (before starting the dosing period) and then weekly for a total of 28 days. The animals were randomly divided into two groups of seven animals each, with the first group undergoing 28 days of PTH (1-34) Teriparatide (Alfa Aesar, Ward Hill, MA, USA) dosing (PTH) and the second group undergoing 14 days of dosing before PTH was withdrawn (PTHW). During dosing, both groups received 30 µg/kg/day of human PTH (1-34) (Alfa Aesar, Ward Hill, MA, USA) by subcutaneous injection daily for a period of 14 days. The PTH dose used was based upon a previously establish protocol,[27] which represents an intermediate dose level when compared with similar rabbit studies.[30,127] On the 14th day the rabbits were imaged *in vivo* at the Canadian Light Source (CLS; *in vivo* imaging, see below). Beginning on the 15th day, the PTHW group was administrated 1 mL of saline at 0.9% concentration in lieu of the PTH dosing (which continued for the PTH group). At the end of the 28th day, all rabbits were euthanized by intravenous injection of pentobarbital sodium (Euthanyl; Bimeda-MTC, Animal Health Inc, Cambridge, Canada) at a dose of 0.4 mL/kg. After euthanasia, right and left tibiae were dissected and fixed in 10% formalin prior to imaging by conventional micro-CT (*ex vivo* imaging, see below). For future histological analysis, the rabbits were labeled using the fluorochrome calcein (Sigma Aldrich, St. Louis, Missouri, USA). Calcein was administered by subcutaneous injection at a dose of 10 mg/kg on days 13 and 14 (label 1) and then on days 27 and 28 (label 2) An overview of the animal protocol is presented in Figure 3.2.

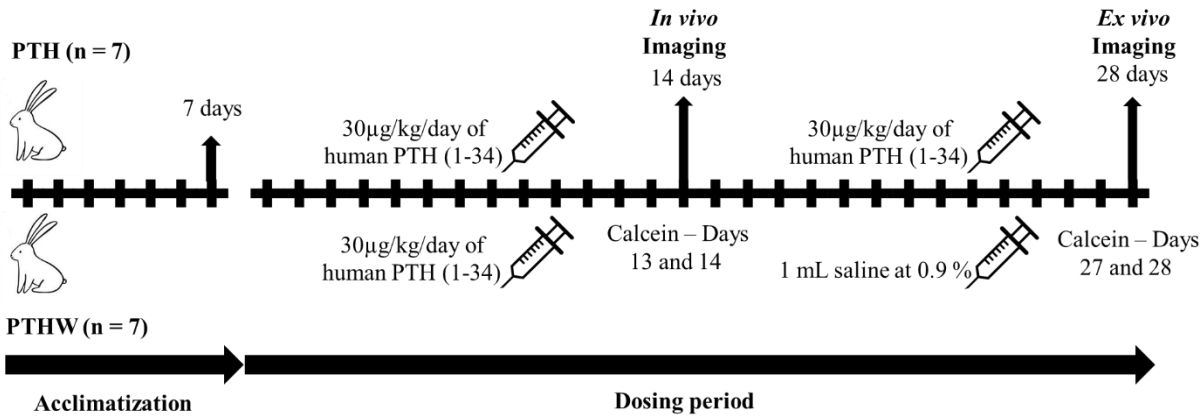

Figure 3.2. Study design for LER and cortical bone microarchitecture and geometry outcomes.

3.2.2. *In vivo* imaging at 14 days

We performed *in vivo* synchrotron-based phase-contrast micro-CT imaging at the Biomedical Imaging and Therapy (BMIT-BM 05B1-1 beamline) facility at the CLS. Rabbits were first anesthetized as per an established protocol using a sedative and anesthetic cocktail of 0.4 mg/kg of butorphanol, 2 mg/kg of midazolam, and 0.1 mg/kg of dexmedetomidine.[138] They were then brought into the imaging hutch and placed in a custom setup and kept under anesthesia with an isoflurane/oxygen gas mixture. The right leg was securely held in place using a cylindrical Lucite sample holder to avoid movement and positioned at 60 cm from the detector to give an ideal phase-contrast propagation (Figure 3.3 A and B).[32] Rectal temperature, heart rate, respiratory frequency, and pulse oximetry were monitored before starting the scans and after the experiment. Oxygen saturation and respiratory frequency were observed during imaging by CCTV video camera. After imaging, a reversal drug cocktail of 1 mg/kg of antisedan and 0.02 mg/kg of flumazenil was administered to reverse the effects of the anesthetics. The animals were kept hydrated and warm until fully recovered.

Imaging of the tibia was performed with an energy of 37.5 keV, with a sequence of 1000 projections over 180 degrees captured at an isotropic voxel size of 13 µm to enable detection of BMU cutting cones (rabbit mean canal diameter ~ 70 µm measured in 3D micro-CT[27]) and some of the larger vascular canals. The mean radiation dose applied was 2.2 Gy, with a rotation velocity of 5.75 deg/s, and exposure time of 31.3 ms. To account for ring current decay, density neutral Lucite filters of varied (20 - 60 mm) thickness were used to maintain a constant dose rate of 0.085

Gy/s. Radiation dose was estimated using a PinPoint ion chamber (model 31014, PTW, Germany).[37] Thermoluminescent dosimeter (TLD) chips (Mirion Technologies, Ontario, Canada) were used to confirm the radiation dose received in the rabbits leg. The methodology used to measure radiation dose using an ion chamber and TLD chips is described in Appendix A. A scout scan was taken first to identify the region of interest to be imaged (Figure 3.3 C). We used the ankle joint (distal tibial epiphysis) as an anatomical landmark to ensure accurate targeting of the same region of interest for the subsequent *ex vivo* imaging. From this landmark we moved 20 mm up, and from that point, we performed the first scan: View #1 = 9.5 mm in height. Immediately above that, we performed a second scan: View #2 = 9.5 mm in height with 0.21 mm of overlap with view #2 (Figure 3.3 C). Scans were filtered back projection reconstructed with flat and dark field corrections and phase retrieval using the UFO-KIT (https://ufo.kit.edu/dis) software (Appendix B), The data sets were generated as 8-bit bitmaps, and 3D renderings were generated and stitched (View #1 + View #2 ~ 19 mm) (Figure 3.4A) using the AMIRA 6.2 (FEI; https://www.fei.com) software package for image registration and LER quantification.

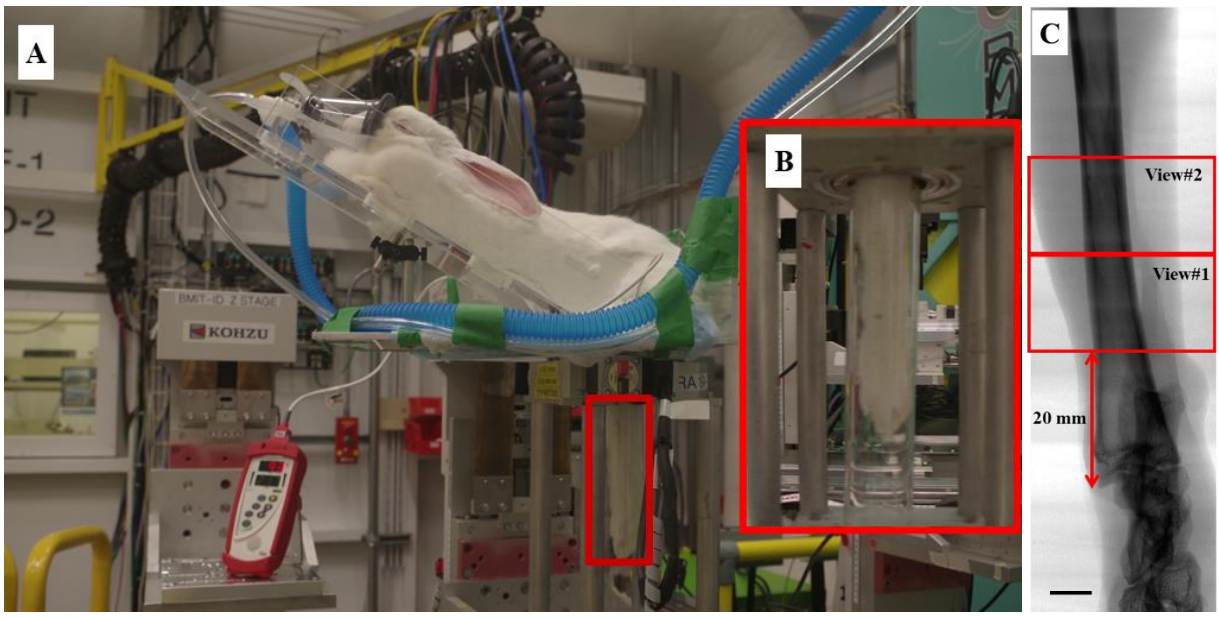

Figure 3.3. (A) Anesthetized rabbit setup for in vivo imaging at the BMIT facility at CLS. (B) Zoomed in view of the right distal tibia to be imaged by synchrotron-based phase-contrast micro-CT; (C) Scout image used to define the regions of interest (View #1 + View #2 ~ 19 mm, with a 0.21 mm of overlap). Scale bar = 5 mm

3.2.3. *Ex vivo* imaging at 28 days

On the dissected tibiae a scalpel was utilized to mark the corresponding landmarks utilized for *in vivo* imaging. A 25 mm region corresponding to Views #1 and #2 (~ 19 mm) + 3 mm below the bottom mark and + 3 mm above the top 2 marks (Figure 3.4 A) was then imaged using a SkyScan 1172 laboratory micro-CT system (Bruker SkyScan, Kontich BE) at 5 μm isotropic voxel size to resolve both remodeling-related resorption spaces and the majority of vascular canals permeating the cortex.[27,37] The latter, unchanged canals, served as stable points of reference for 3D image registration. The scan protocol included X-ray settings at 74 kVp, 135 μA, with an exposure time of 500 ms, rotation step of 0.2 over 180 degrees, and 0.5 mm aluminum filter (to remove low energy photons). The *ex vivo* micro-CT data sets were filtered back projection reconstructed using the NRecon software package (Bruker). The data sets were generated as 8-bit bitmaps, and their 3D renderings (Figure 3.4 B) were generated using AMIRA 6.2.

3.2.4. 3D image registration and LER quantification

For the right limbs, the *in vivo* and *ex vivo* (downscaled by a factor of two, to 10 μm) data sets were visually segmented using the best range threshold for each data set, separating BMU-related resorption spaces and vascular canals from the higher density bone. A step by step of the segmentation is presented in the Appendix C1. Following segmentation, the 3D volumes were registered as described:

1) The *in vivo* data set was manually aligned (translated and rotated) into position between the two marks (bottom and top) of the *ex vivo* data set, to improve the outcome of the subsequent automated registration.[139]

2) Automatic affine registration was then applied using the rigid (translation and rotation) transformation, isotropic scaling (as the images had different voxel size, even after downscaling the *ex vivo* data sets) and correlation metrics to converge on the best fit between the two data sets (Figure 3.4 C and D). After this step, the 3D registration was visually inspected, and in the case of a mismatch, manual adjustment was applied followed by another two or three iterations of automatic registration depending on the data set.

The advance of BMUs, detectable as a change in position between the two data sets, was manually landmarked with points placed on the most forward points of the cutting cones. The 3D distance (D) (Figure 3.3 F) traversed by BMUs during the time between scans was calculated as $D = \sqrt{(X2 - X1)^2 + (Y2 - Y1)^2 + (Z2 - Z1)^2}$, where, X1, Y1, and Z1 were recorded from the *in vivo* scan (t1) and X2, Y2, and Z2 were recorded from the follow-up *ex vivo* scan (t2). Daily LER (µm/day) was calculated as D/(t2 − t1). We targeted quantifying 25 BMUs in View#1 and View#2, giving a total of 50 BMUs for analysis. A step-by-step description of this methodology is presented in Appendix C.

We have also quantified BMU advance direction along the tibia diaphysis using Z1 and Z2 coordinates divided by the time intervals t1 and t2. The BMU direction going up towards the proximal tibia was calculated as Z2 – Z1/t2-t1 > 0 = + LER, and the BMU direction going down towards the distal tibia as Z2 – Z1/t2 – t1 < 0 = - LER.

3.2.5. Cortical bone microarchitecture and geometry

Analysis of cortical bone microarchitecture and geometry was conducted in the 20 mm long region of interest of the right *in vivo* and *ex vivo* scans and in the comparable region of the left *ex vivo* scans using CTAnalyser (CTAn; version 1.16.4.1; Bruker). The scan data sets were binarized using Otsu automatic thresholding to measure cortical porosity (Ct.Po, %), mean canal diameter (Ca.Dm, µm), and cortical thickness (Ct.Th, µm) in 3D. The geometric parameters of cortical area (Ct.Ar, mm^2), total area (Tt.Ar, mm^2), and medullary area (Ma.Ar, mm^2) were accessed in 2D using a single, midpoint slice of the 20 mm region of interest.[27,37] These measures facilitated both comparison both between the treatment group (PTH *vs.* PTHW) and within animals (right *vs.* left), with the latter providing an assessment of the potential impacts of the *in vivo* scan radiation.

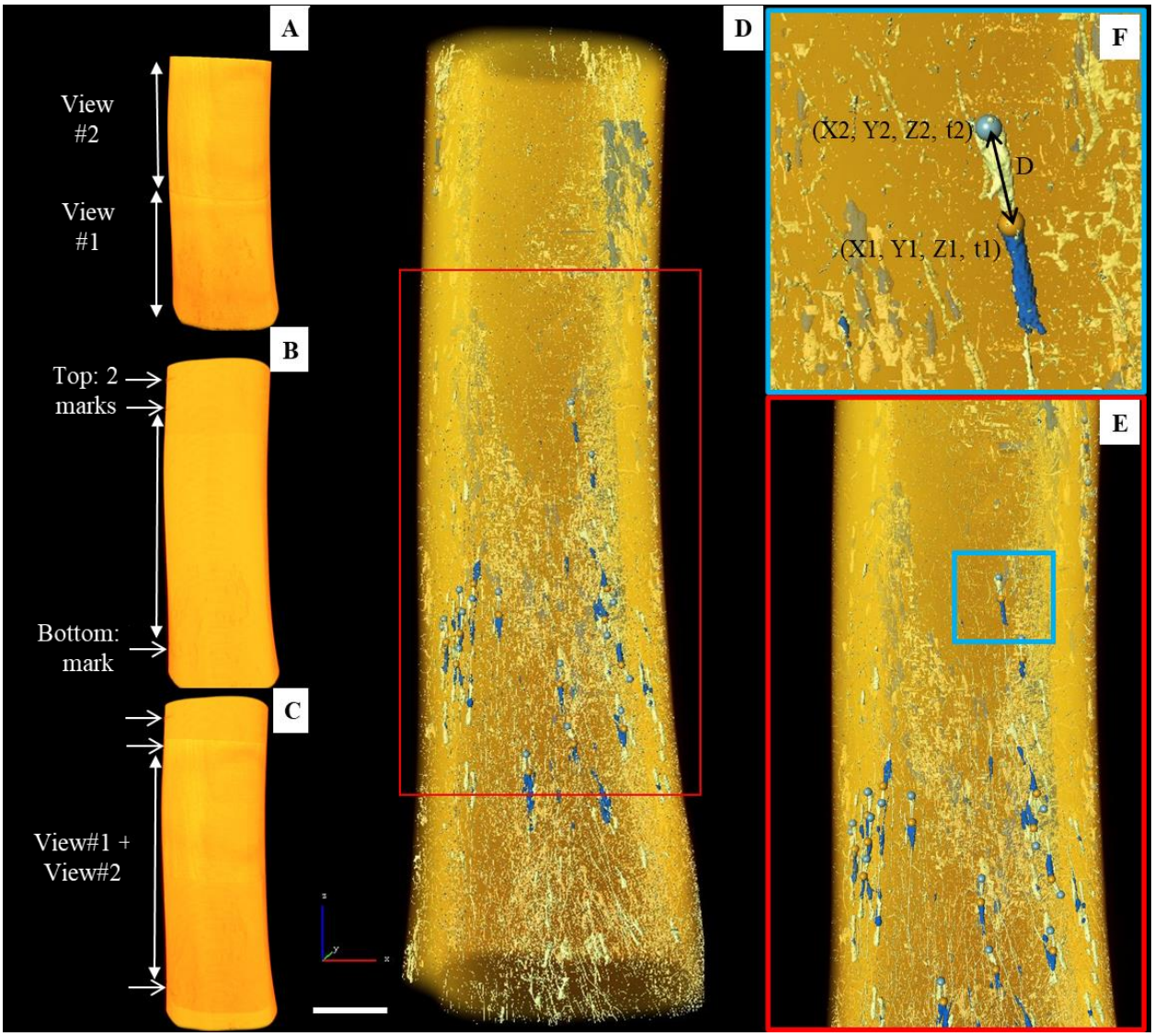

Figure 3.4. (A) 3D renderings of in vivo images with view #1 + view #2 stitched (voxel size = 13 µm). (B) 3D rendering of ex vivo image (voxel size = 5 µm). (C) 3D image registration, where the in vivo dataset was manually aligned (translated and rotated) into position between the two marks (bottom and top) of the ex vivo dataset. (D) BMUs in vivo in blue and ex vivo in white. (E) zoomed-in view showing BMU progression; (F) BMU landmarks in gold for in vivo and in blue for ex vivo,where D is the 3D distance traversed by BMUs during t1 and t2. Scale bar: 2 mm.

3.2.6. Statistical analysis

All statistical analyses were performed with IBM SPSS Statistics (v28.0; SPSS Inc., Chicago, IL). The first step was to check the assumptions of normality and homogeneity of variance using Shapiro-Wilks and Levene's tests, respectively, with $\alpha = 0.05$, to decide between parametric and nonparametric tests. As normality was not confirmed for LER and BMU direction, but the data showed the same variance between groups (Levene's test, $\alpha = 0.05$), we used the nonparametric Mann-Whitney test ($\alpha = 0.05$) and the Wilcoxon signed-rank test ($\alpha = 0.05$), respectively. The assumptions of homogeneity of variance and normality were met for body weight and the cortical microarchitecture and geometry outcomes from PTH and PTHW, and we compared the data using two-way mixed ANOVA (one within and one between-subjects factor, $\alpha = 0.05$), where dosing time was the within-subjects factor, treatment group was the between-subjects factor, and dosing time *vs.* group was tested for an interaction between factors. As our data had only two levels of repeated measures (14 and 28 days), the concept of sphericity was considered met (Greenhouse-Geisser epsilon [ε] = 1, sphericity assumed).[140] The equality of covariance matrices was measured by a Box's M test ($\alpha = 0.05$), and the data were also assessed for outliers by examination of studentized residuals for values greater than ± 3. For the parameters that presented a statistically significant interaction, we performed the analysis using simple main effects with pairwise comparisons.

3.3. Results

3.3.1. PTH reduces LER relative to PTHW

LER was assessed for 651 BMUs (seven PTH rabbits with 50 BMUs each: N = 350, five PTHW rabbits with 50 BMUs each, one with 33 BMUs and another one with 17 BMUs: N = 301) from the 14 registered scan sets. LER distributions for PTH and PTHW were similar, and both were skewed left, as assessed by visual inspection of histograms (Figure 3.5 A). Counter to our hypothesis, the median LER was higher for PTHW than for PTH ($p < 0.01$, Figure 3.5 B and Table 3.1).

Table 3. 1. LER quantification

	Group		Mann-Whitney U Test (α = 0.05)		
	PTH (N= 350)	PTHW (N = 301)			
Parameter	Mean ± sd (Minimum – Maximum)	Mean ± sd (Minimum – Maximum)	PTH Median (IQR)	PTHW Median (IQR)	p
LER (µm/day)	34.61 ± 10.61 (14.20 – 76.50)	39.37 ± 11.01 (17.70 – 79.80)	32.55 (12.03)	37.80 (12.35)	< 0.01*

LER = longitudinal erosion rate. PTH = parathyroid hormone. PTHW = parathyroid hormone withdrawal. sd = standard deviation. IQR = interquartile range. *Statistically significant.

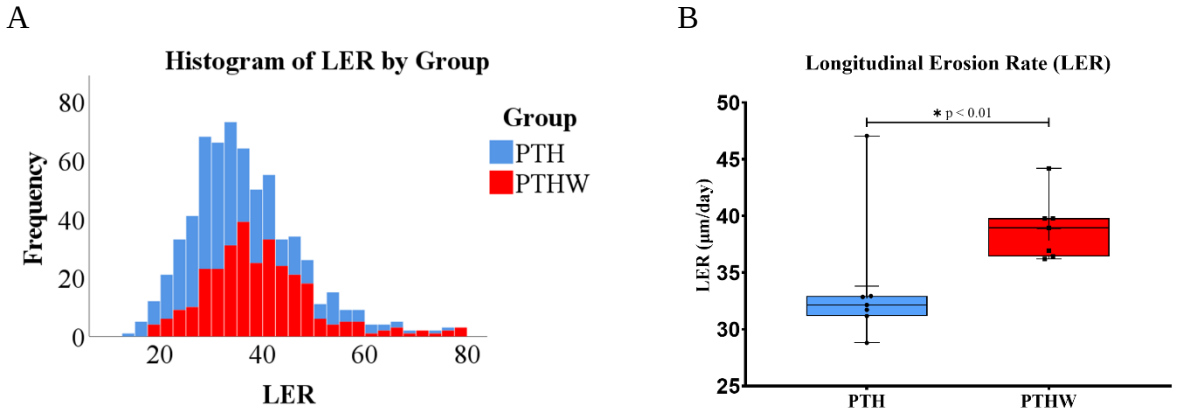

Figure 3.5. (A) LER distribution. Both PTH (N = 350) and PTHW (N = 301) are skewed left. (B) LER data are presented as boxplot (n = 7/group) with median, interquartile range, max and min values plotted as dots, and mean as a cross. A Mann-Whitney U test (α = 0.05) was used to compare medians.

BMU direction along the diaphysis was divided as + LER and – LER (Table 3.2). PTH showed + 166 LER and - 184 LER (p = 0.097) while PTHW showed + 150 LER and - 151 LER (p = 0.061). We also analyzed BMU direction in relation to the scan views (Table 3.3). PTH showed differences in - LER in View# 1 and View 2 (p = 0.027) as well as + LER in View#1 and View#2 (p = 0.027). PTHW did not present differences in - LER in View# 1 and View 2 (p = 0.262) or + LER in View#1 and View#2 (p = 0.931).

Table 3. 2. BMU direction along the tibia diaphysis

Group	BMU Direction		Wilcoxon Signed-Rank Test (α = 0.05)
	Z2 – Z1/t2 – t1 > 0 = + LER	Z2 – Z1/t2 – t1 < 0 = - LER	p
PTH (N = 350)	166	184	0.097
PTHW (N = 301)	150	151	0.061

LER = longitudinal erosion rate. PTH = parathyroid hormone. PTHW = parathyroid hormone withdrawal.

Table 3. 3. BMU direction in View# 1 and View# 2

Group	Scan Views		Wilcoxon Signed-Rank Test (α = 0.05)
	View# 1	View# 2	p
PTH + LER	97	70	0.027*
PTH - LER	78	105	0.027*
PTHW + LER	75	77	0.931
PTHW – LER	70	79	0.262

LER = longitudinal erosion rate. PTH = parathyroid hormone. PTHW = parathyroid hormone withdrawal. *Statistically significant.

3.3.2. Cortical porosity increases with PTH dosing but remains stable after withdrawal, and cortical geometry measures differ by dosing time

Micro-CT 3D renderings and 2D cross-sectional images are presented in Figure 3.6. Figure 3.6A shows in 2D that PTH induced periosteal and endosteal bone formation, and intracortical remodeling (Figure 3.6 A 2D a,b,c). Table 3.4 shows the results of the microstructural and geometric measures. Ct.Po differed by time and group ($p < 0.01$ and $p = 0.006$, respectively), and there was an interaction between these factors ($p < 0.01$) (Table 3.4). Simple main effect analysis reveled that Ct.Po was increased for PTH at day 28 *vs.* day 14 ($p < 0.01$, Table 3.3 and Figure 3.4B 2D a,b,c); however, for PTHW, Ct.Po did not differ by time ($p = 0.620$). Between groups, Ct.Po was increased at 28 days for PTH compared with PTHW ($p < 0.01$, Table 3.5 and Figure 3.7 A). Ca.Dm (Table 3.4, Figure 3.7 B and Figure 3.8) was decreased over time (day 28 *vs.* day 14) in both groups ($p < 0.01$,), but the decrease was not different between PTH and PTHW ($p = 0.122$). Ct.Th, Tt.Ar, Ct.Ar and Ma.Ar did not differ by group (Table 3.4 and Figure 3.7 C-F). Intriguingly, dosing time was statistically significant showing a slight increase in Ct.Th ($p < 0.01$), Tt.Ar ($p = 0.025$), and Ct.Ar ($p < 0.01$) and a slight decrease in Ma.Ar ($p = 0.009$).

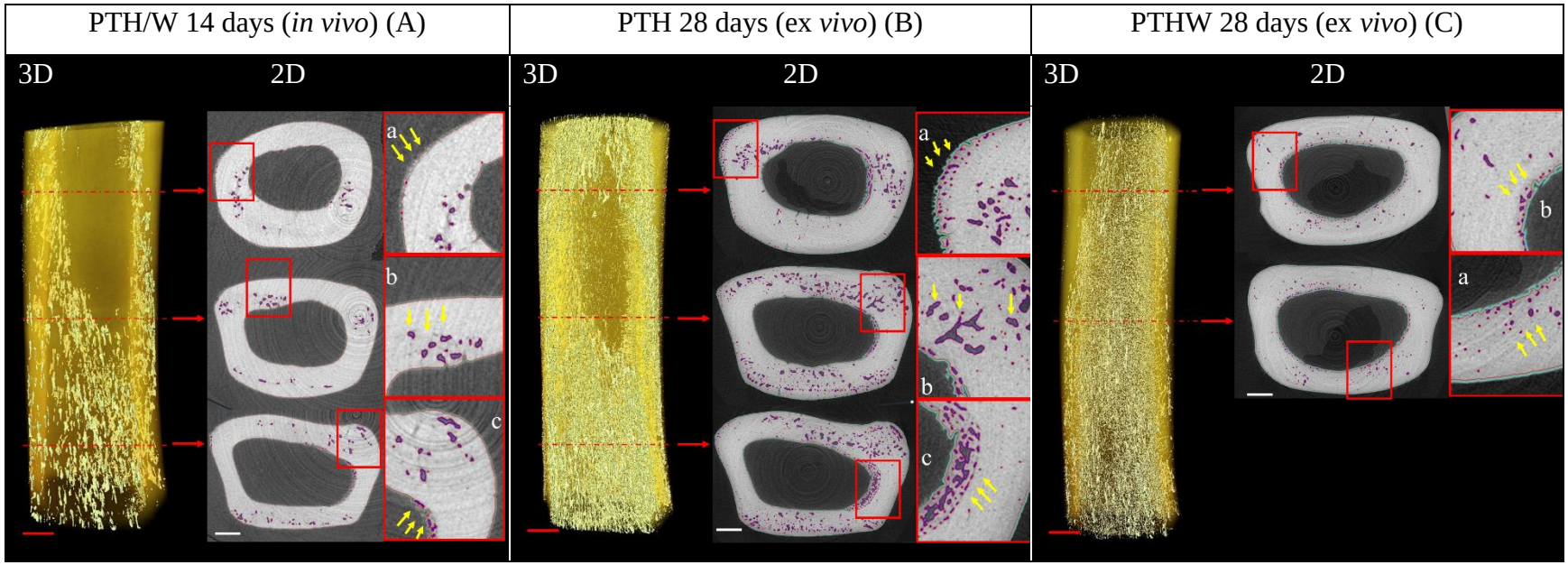

Figure 3.6. 3D renderings with vascular canals highlighted in light yellow (red scale bar = 2 mm) and 2D cross sectional images with pores highlighted in purple (white scale bar = 1 mm), where (A) 3D and 2D images of PTH/W at 14 days, (B) 3D and 2D images of PTH at 28 days, and (C) 3D and 2D images of PTHW at 28 days. Regions a, b and c = zoom in of 2D images with yellow arrows showing periosteal formation, intracortical remodeling and endocortical formation (respectively) in A and B. In C, regions a and b showing intracortical remodeling and endocortical formation (respectively).

Table 3. 4. Statistical analysis of cortical bone microarchitecture and geometric parameters by dosing time and group for the right tibiae

	Dosing Time				Two-way Mixed ANOVA ($\alpha = 0.05$)		
	Day 14 (*in vivo*)		Day 28 (*ex vivo*)				
	PTH (n= 7)	PTHW (n = 7)	PTH (n= 7)	PTHW (n = 7)	Dosing Time	Group	Dosing Time *vs.* Group
Parameters	**Mean ± sd**	**Mean ± sd**	**Mean ± sd**	**Mean ± sd**	**p**	**p**	**p**
Ct.Po (%)	1.03 ± 0.50	1.00 ± 0.70	2.97 ± 0.88	0.90 ± 0.40	< 0.01*	0.006*	< 0.01*
Ca.Dm (µm)	101.48 ± 19.24	98.34 ± 16.00	73.12 ± 12.60	54.31 ± 3.50	< 0.01*	0.122	0.053
Ct.Th (µm)	1320.51 ± 87.25	1362.35 ± 91.73	1423.64 ± 103.87	1442.03 ± 97.00	< 0.01*	0.550	0.418
Tt.Ar (mm^2)	34.08 ± 3.17	35.58 ± 0.71	34.62 ± 3.57	35.67 ± 0.75	0.025*	0.348	0.088
Ct.Ar (mm^2)	21.56 ± 1.72	22.76 ± 1.11	22.66 ± 1.78	23.42 ± 1.29	< 0.01*	0.242	0.135
Ma.Ar (mm^2)	12.51 ± 1.96	12.82 ± 1.16	11.97 ± 2.43	12.25 ± 1.13	0.009*	0.754	0.941

Ct.Po = cortical porosity. Ca.Dm = canal diameter. Ct.Th = cortical thickness. Tt.Ar = total tissue area. Ct.Ar = cortical area. Ma.Ar = marrow area. PTH = parathyroid hormone. PTHW = parathyroid hormone withdrawal. sd = standard deviation. CI = confidence interval. *Statistically significant.

Table 3. 5. Statistical analysis of cortical bone porosity (Ct.Po) by pairwise comparisons (two-way mixed ANOVA with simple main effects)

	Dosing Time				**Two-way Mixed ANOVA (α = 0.05) - Pairwise Comparisons**			
	Day 14 (*in vivo*)		**Day 28 (*ex vivo*)**					
	PTH	**PTHW**	**PTH**	**PTHW**	**Day 14**	**Day 28**	**PTH**	**PTHW**
	(n= 7)	**(n = 7)**	**(n= 7)**	**(n = 7)**	**PTH *vs* PTHW**	**PTH *vs* PTHW**	**Day 14 *vs* 28**	**Day 14 *vs* 28**
Parameters	**Mean ± sd**	**Mean ± sd**	**Mean ± sd**	**Mean ± sd**	**p (95 % CI)**	**p (95 % CI)**	**p (95 % CI)**	**p (95 % CI)**
Ct.Po (%)	1.03 ± 0.50	1.00 ± 0.70	2.97 ± 0.88	0.90 ± 0.40	0.889 (-0.65 - 0.75)	< 0.01 (1.28 - 2.87)	< 0.01 (-2.33 - -1.56)	0.620 (-0.29 - 0.47)

Ct.Po = cortical porosity. PTHW = parathyroid hormone withdrawal. sd = standard deviation. CI = confidence interval. *Statistically significant.

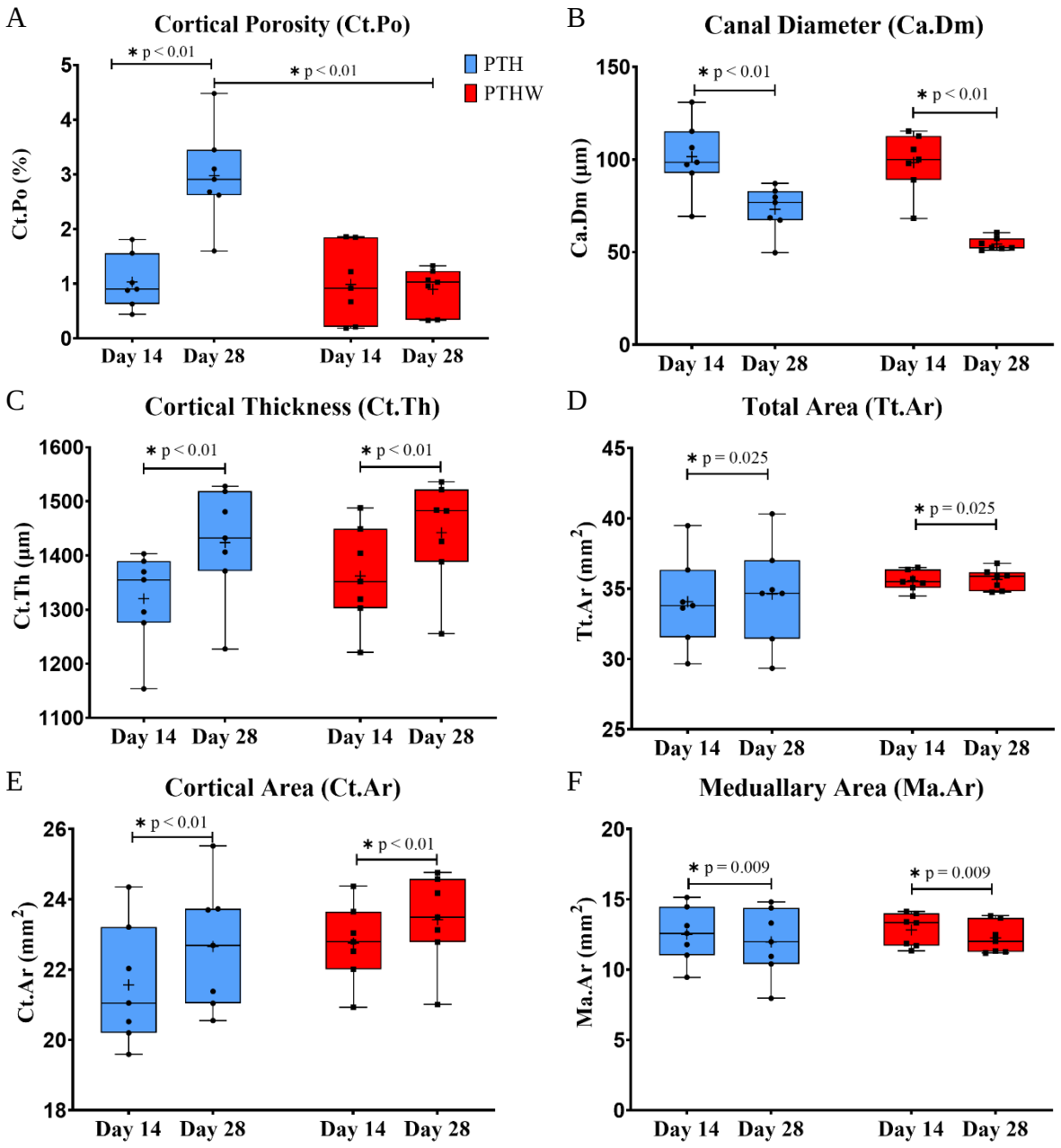

Figure 3.7. Cortical bone microarchitecture and geometry analysis by time (day 14 vs. day 28) and group (PTH vs. PTHW). Where A represents Cortical porosity (Ct. Po) results (bars showing statistically significant difference ($\alpha = 0.05$) for simple main effect). B-F show comparison of canal diameter (Ca.Dm), cortical thickness (Ct.Th), total area (Tt.Ar), cortical area (Ct.Ar) and medullary area (Ma.Ar) results (bars showing statistically significant difference ($\alpha = 0.05$) for main effect time). Data are presented as boxplot (n = 7/group) with median, interquartile range, max and min values plotted as dots, and mean as a cross.

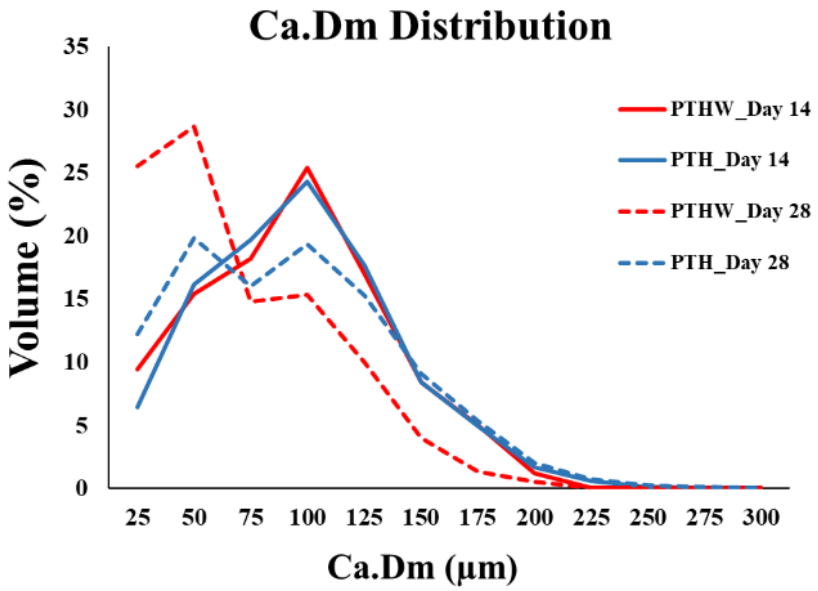

Figure 3.8. Cortical canal diameter (Ca.Dm) distribution in PTHW and PTH by time.

3.3.3. Radiation dose employed does not affect cortical bone microarchitecture and geometry in a time frame of 14 days

The effect of radiation dose on cortical bone microarchitecture and geometry, comparing body side and group at 28 days (*ex vivo*; left tibia *vs.* right tibia, and PTH *vs.* PTHW), is presented in Table 3.6 and Figure 3.9. There was no difference between body sides (contralateral left *vs.* right tibiae) nor an interaction with group ($p \geq 0.099$, Table 3.6). The groups only differed for Ct.Po ($p < 0.01$) and Ca.Dm ($p < 0.01$), reflecting intergroup differences as previously discussed in Section 3.3.2. Importantly, these results showed no radiation effects in cortical bone microarchitecture and geometry parameters for the period of 14 days between *in vivo* and *ex vivo* images.

Table 3. 6. Statistical analysis of radiation dose effect in cortical bone microarchitecture and geometry parameters by body side and group

	Body Side (*ex vivo*)				**Two-way Mixed ANOVA (α = 0.05)**		
	Left Tibiae		**Right Tibiae**				
	PTH (n= 7)	**PTHW (n = 7)**	**PTH (n= 7)**	**PTHW (n = 7)**	**Body Side**	**Group**	**Body Side *vs.* Group**
Parameters	**Mean ± sd**	**Mean ± sd**	**Mean ± sd**	**Mean ± sd**	**p**	**p**	**p**
Ct.Po (%)	3.31 ± 1.21	0.82 ± 0.33	2.98 ± 0.88	0.90 ± 0.40	0.313	< 0.01*	0.125
Ca.Dm (µm)	75.4 ± 8.82	53.97 ± 3.95	73.13 ± 12.59	54.31 ± 3.49	0.461	< 0.01*	0.322
Ct.Th (µm)	1424.99 ± 127.98	1441.99 ± 85.33	1423.64 ± 103.87	1442.03 ± 97.01	0.929	0.755	0.926
Tt.Ar (mm^2)	35.40 ± 2.84	35.68 ± 1.50	34.63 ± 3.57	35.67 ± 0.75	0.202	0.611	0.215
Ct.Ar (mm^2)	22.85 ± 1.85	23.38 ± 1.23	22.66 ± 1.78	23.42 ± 1.29	0.655	0.446	0.520
Ma.Ar (mm^2)	12.54 ± 2.11	12.30 ± 1.27	11.97 ± 2.43	12.25 ± 1.13	0.099	0.984	0.156

Ct.Po = cortical porosity. Ca.Dm = canal diameter. Ct.Th = cortical thickness. Tt.Ar = total tissue area. Ct.Ar = cortical area. Ma.Ar = marrow area. PTH = parathyroid hormone. PTHW = parathyroid hormone withdrawal. Sd = standard deviation. *Statistically significant.

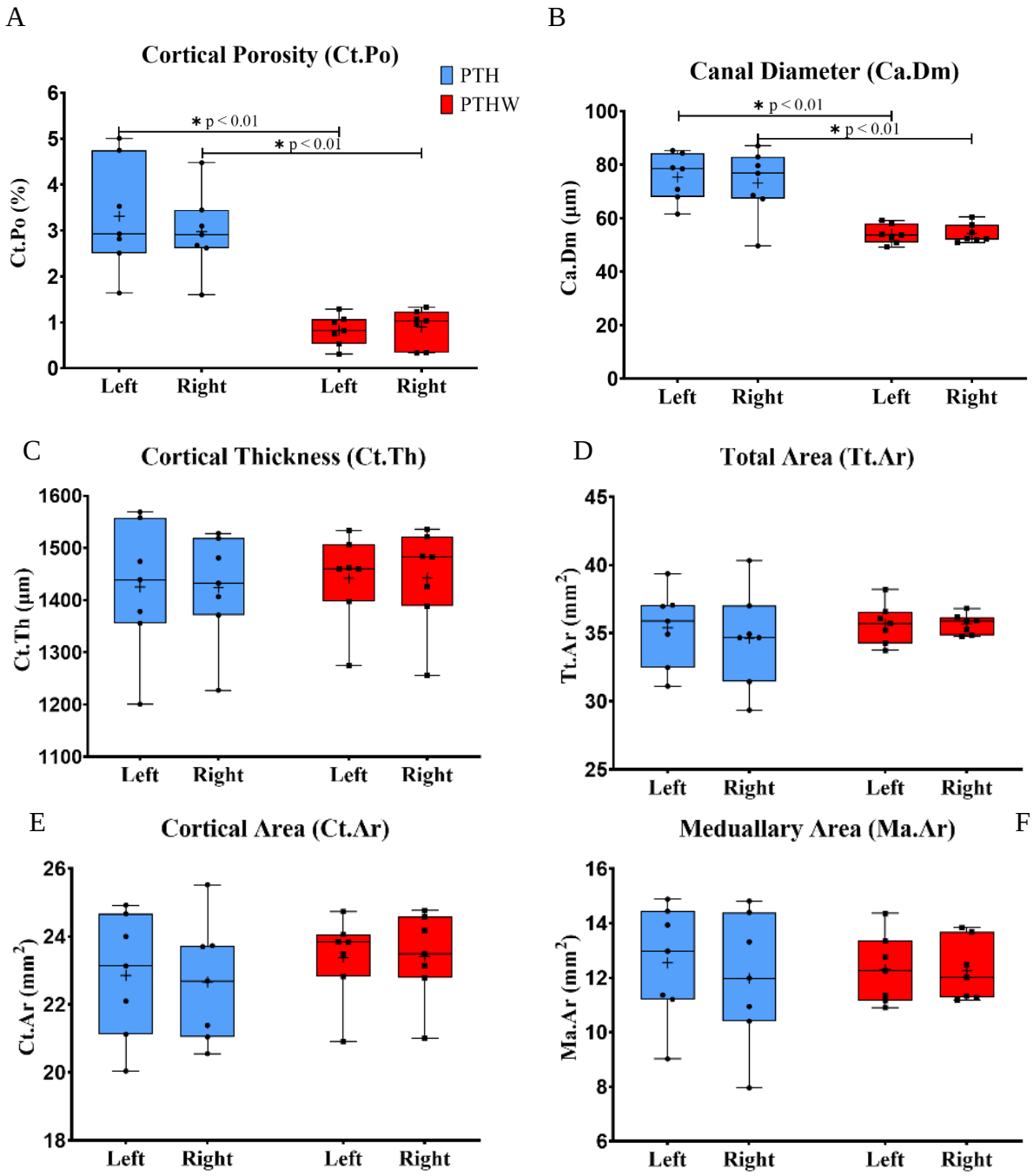

Figure 3.9. (A-F) comparison of cortical bone microarchitecture and geometry by body side (contralateral left vs. right tibiae) and group (PTH vs. PTHW) at 28 days (ex vivo). Data are presented as boxplot (n = 7/group) with median, interquartile range, max and min values plotted as dots, and mean as a cross. With bars showing statistically significant difference ($\alpha = 0.05$) for main effect, group.

3.3.4. No difference in body weight

The rabbits' weight did not differ by time (p = 0.378), nor group (p = 0.081), and there was no interaction between dosing time and treatments (p = 0.201). Moreover, the results revealed that all animals tolerated the experimental conditions (PTH dosing and *in vivo* synchrotron imaging) very well with neither group changing between day 0 and 28 (Table 3.7).

Table 3. 7. Rabbit weight at day 0 and day 28 during dosing period

	Dosing Time				**Two-way Mixed ANOVA (α = 0.05)**		
	Day 0		**Day 28**				
	PTH (n= 7)	**PTHW (n = 7)**	**PTH (n= 7)**	**PTHW (n = 7)**	**Dosing Time**	**Group**	**Dosing Time *vs.* Group**
Parameter	**Mean ± sd**	**Mean ± sd**	**Mean ± sd**	**Mean ± sd**	**p**	**p**	**p**
Weight (kg)	3.72 ± 0.16	3.76 ± 0.13	3.68 ± 0.22	3.88 ±0.14	0.378	0.081	0.201

PTH = parathyroid hormone. PTHW = parathyroid hormone withdrawal. sd = standard deviation. CI = confidence interval.

3.4. Discussion

In the present work, we studied the effect of PTH on LER using our recently developed methodology to quantify BMU LER in 4D (3D over time), combining longitudinal *in vivo* synchrotron-based phase-contrast micro-CT with a PTH rabbit model.[37] More specifically, we aimed to study how PTH impacts BMU progression *via* two different dosing regimens, PTH and PTH withdrawal (PTHW). Counter to our hypothesis, we found that LER was lower in PTH (34.61 µm/day) compared with PTHW (39.37 µm/day). This result is inconsistent with the underlying assumptions of the classic LER studies of Jaworski and Lok,[24] Takahashi and Norimatsu,[25] and Parfitt,[7] who all assumed that the advances of the cutting and closing cones are equal and function in ways that do not change over time. Cortical bone loss in osteoporosis and aging has been shown to be a result of an imbalance between the cutting and closing cones due to premature termination of bone formation, resulting in increased porosity.[66] Recent studies have shown that cortical bone

loss also reflects that the reversal-resorption phase is generally prolonged, leading to a delay or absence of initiation of bone formation, resulting in an enlargement of the pores.[59] Moreover, it was postulated that the coupling/uncoupling mechanism between the reversal-resorption phase and formation is governed by an osteoprogenitor density threshold. If the cell threshold is not reached, bone formation cannot start, and its absence is a significant contributor to bone loss.[59,66] In trabecular bone studies, PTH has been shown to favor the availability of osteoprogenitors cells,[141,142] to reduce the time for initiation of bone formation,[58,143] and to decrease resorption depth.[143] Our results in cortical bone suggest that PTH slows LER compared with PTHW, whereas it speeds bone formation (according to several rabbit studies PTH increases On.MAR[27,30,39,127,128]). A recent follow up study performed by our group using sham ovariohysterectomy (OVH) rabbits found a mean LER of 39.9 µm/day (unpublished data). If PTH slows down LER and simultaneously increases the closing cone advance, then the size of the reversal-resorption phase can be considered shorter, as well as the time required to reach the postulated cellular density, therefore decreasing the overall volume of remodeling space. In other words, PTH appears to have an important role in enhancing the coupling between the cutting and closing cones. One could ask, but what happens if the closing cone increase outpaces the cutting cone going beyond coupling? We can argue that if at some point the closing cone is faster than the cutting cone, then the volume of the resorption space will change. In our study, we noticed in the *ex vivo* scans that some *in vivo* BMUs seemed to be resolved, that the resorption space was filled and no clear BMU continued. Future analysis could examine if PTH leads to a shorter BMU lifespan.

In the present work, we did not measure Ac.f. However, we know from our previous work[27] and other studies[30,39] that PTH increases Ac.f in rabbits. Martin,[144] using mathematical analysis, showed that if Ac.f is decreased, the number of new remodeling spaces will decline relative to the number of refilling BMUs, yielding a decline in porosity. On the other hand, if Ac.f is increased (as occurs with PTH), the number of remodeling spaces will increase in proportion to refilling BMUs, and there will be an increase in porosity. Cortical porosity can be increased by an enlargement of the remodeling spaces related to a defect in balance and coupling, as discussed above, by an increase in the number of remodeling spaces related to an increase in Ac.f, or both. Our result suggests that PTH slows LER and enhances coupling, which yields a positive bone remodeling balance. Therefore, we can argue that PTH increases bone formation rates in the

periosteal, endosteal, and intracortical surfaces, as shown in rabbit studies,[27,30,39] which produces an overall anabolic outcome despite increases in Ac.f. Further studies of PTH, or any other osteoporosis treatment, directly impacting BMUs could help improve treatment and potentially reduce adverse effects.

Our LER previous study[37] found a mean LER of 23.8 µm/day over the 14 days between *in vivo* and *ex vivo* imaging (Supplemental Figure 3.10). Here, we have used the same animal protocol as previously (30 µg/kg/day of human PTH [1-34]),[37] and the only difference was the scan views. In the present study, the region of interest was larger (View #1 + View #2 ~ 19 mm) than that used in the previous study (View #1 ~ 10 mm). As such, we sought to rule out the possibility of LER variation along the diaphysis. We plotted the distribution of individual BMU LER values and BMU counts in relation to their mid-Z coordination position (Supplemental Figures 3.10 A and B, respectively). There was no apparent relationship in LER distribution along the diaphysis. PTH showed a similar distribution in the total number of BMUs (View #1 = 178 and View #2 = 172) along the diaphysis, whereas PTHW showed a higher number of BMUs in the more proximal view (View #1 = 119 and View #2 = 182). However, the total number of BMUs were not different by view ($p = 0.606$) or group ($p = 0.534$). In the literature, LER was inferred in dogs by longitudinal histological sections using 2D labeling techniques. Jaworski and Lok[24] reported LER varying between 37 and 44.4 µm/day. In a second study Jaworski and colleagues,[26] using the same methodology, found that LER was reduced in uremic (27.7 µm/day) *vs.* normal (43.61 µm/day) dogs. Differences in our first and second LER measurements could be attributed to differences in intraspecies variation. However, they could also be due to a sampling issue, as in this study, we measured more BMUs (n = 651) compared with our first LER study (n = 186). Supplemental Figure 3.10 shows a few high LER values from PTH and PTHW in the distribution, which shifted the mean to the right compared with our previous study. Additionally, with respect to other classical studies, we cannot rule out interspecies variation between our rabbits and the dogs in other studies, as well as intraspecies variations (type of bone and age differences). Jaworski and Lok's[24] work, for example, showed a high variation in the length of cutting cones (using their first method) and in the length of osteoid (using their second method) in the dog ribs.

Heřt and colleagues,[145] studying osteon orientation in the diaphysis of long human bone, observed that osteons are aligned along the dominant local mechanical loading (longitudinal) direction. Such observation was confirmed by Petryl et al.[146] that also indicated that cutting cone

tunnelling is guided by mechanical stimuli. On the other hand, the absence of mechanical load seems to deregulate the orientation and sizes of resorption spaces.[147] Studies using the finite element (FE) model in 2D[148] and 3D[149,150] have shown that BMU trajectories are influenced by mechanical load and microdamage. It is not the scope of this paper to discuss bone biomechanics. However, our data allowed us to quantify the BMU advance direction in a way that was not explored before. We have not found differences in the BMU direction along the diaphysis in both PTH and PTHW (Table 3.2 and Supplemental Figure 3.11 C). However, when we divided the analysis by scan view, we found that PTH showed differences in - LER in View# 1 and View 2 ($p = 0.027$) and + LER in View#1 and View#2 ($p = 0.027$) (Table 3.3). Martinez-Reina and colleagues[150] have used 3D strain-based and strain and damaged-based FE models to study BMU trajectories and orientation along a human femur's diaphysis. The angle α orientation defined the BMU trajectories with respect to the long bone axis (or Z coordinate in 3D). The authors divided the diaphysis into two halves, distal and proximal (or View#1 and View# 2, respectively, in the present work). Their results showed differences in BMU orientation in the distal and proximal halves using bone models. However, the authors did not differ BMU trajectory as going up (+ LER) and going down (- LER).

Beyond LER, our additional measures of cortical bone microarchitecture and geometric parameters are consistent with past studies. Our PTH rabbits dosed for 28 days showed a mean Ct.Po of 2.97%. This result is consistent with two other PTH rabbit studies performed by our group (LER PTH_previous(a)[37]: Ct.Po = 2.93% to 6.94%, *ex vivo* PTH_previous(b)[27]: Ct.Po = 1.51% to 6.00%) (Supplemental Figure 3.12 A) and a third study by Yamane et al.,[128] who dosed their rabbits with 40 µg/kg/day for 4 weeks, and they found a Ct.Po of 3.62% in the tibiae using micro-CT. Our Ca.Dm decreased in both of our groups (Table 3.4). The differences can be attributed to the anabolic effects of PTH, but also to the difference in imaging modalities (synchrotron micro-CT *in vivo* and conventional micro-CT *ex vivo*) and their respective voxel sizes (13 µm and 10 µm) used in our method. As shown in Figures 3.6 B and C, both PTH and PTHW at 28 days (*ex vivo* scans) showed an elevated presence of small structures compared with the images taken at 14 days (Figure 3.6 A). This is most likely primarily due the higher resolution used in the *ex vivo* scans that allowed the small structures to be detected, as well as to the Otsu's automatic segmentation applied that included many smaller canals in the quantification. In our previous studies, we used a fixed global threshold to segment only the larger canals. Therefore, the tiny

structures detected in this study contribute to the decrease in Ca.Dm, as this parameter is calculated by Hildebrand's[151] sphere-fitting method. We also compared Ca.Dm distribution of PTH and PTHW with our two other studies (Supplemental Figure 3.12 C). There was a peak in values at 50 µm and another one at 100 µm in PTHW. PTH showed two peaks with similar distributions at 50 µm and 100 µm; this result is very similar to that of our LER PTH_previous(a) study (a).[37] The 100 µm values match the expected size of rabbit osteons/BMUs,[27] and the lower values can be related to the increased scan resolution at 28 days (*ex vivo* scan). Our *ex vivo* PTH_previous(b) study[27] also showed a peak at 100 µm and a second one skewed right to large pores (125 µm), suggesting coalescence of canals. Zebaze and coworkers[127] reported that PTH produces larger pores by enlarging existing canals, which we also observed in both of our studies. Some studies have shown that cortical bone can be remodeled by two types of processes.[60,66] One is associated with remodeling events with the classic cutting and closing cones tunneling into the cortex (called type I pores), and the other one is associated with enlargement of existing pores (widening into Haversian resorption spaces, called type II pores). The PTH rabbits seem to show both types of remodeling. Intriguingly, Ct.Th, Tt.Ar, Ct.Ar and Ma.Ar differed over time, but not by group (Table 3.4 and Figure 3.7 C-F). Such differences can be attributed to the anabolic effects of PTH in the endosteal and periosteal surfaces but also to the difference in imaging modalities, as mentioned above. We observed modeling activities on the endosteal and periosteal surfaces at 14 days (Figure 3.6 A), and they were more pronounced at 28 days (Figure 3.6 B). The endosteal activities are linked to new bone formation as reported in our two other studies[27,37] and studies conducted by different groups.[30,39,127] We also can not rule out the possibility that the rabbits were still growing.

Our LER, cortical bone microarchitecture, and geometric outcomes showed high levels of variation that were also observed in our previous studies (LER PTH_previous(a)[37] and *ex vivo* PTH_previous(b)[27]), as shown in in Supplemental Figures 3.9 and 3.11. However, the variations in the present study were not identified as outliers when assessed by examination of studentized residuals for values greater than ± 3, and thus, all the data were retained for analysis.

To rule out any impact of radiation dose in our cortical remodeling outcomes, we compared the *ex vivo* scans of the right tibiae (irradiated *in vivo*) with their contralateral left. The radiation dose of 2.2 Gy used in our study did not affect the cortical parameters from both groups in the 14-day interval between *in vivo* and *ex vivo* scans, as presented in Table 3.6 and Figure 3.9. Our

previous LER study investigated potential radiation dose impacts on LER advancement and cortical bone microarchitecture employing 1 Gy, 2.5 Gy and 5 Gy in the *in vivo* scan. LER did not differ across radiation dose groups, nor did cortical microarchitecture outcomes comparing right *vs.* left (contralateral) tibiae. The 2.5 Gy dose provided sufficient image quality and 3D registration capacity and thus was selected for the present study.[37] As the dose was below 5 Gy (even in the region of overlap between scans), and no radiation impact was found in the previous LER study and most other measures, this enabled the possibility to scan the region of interest twice in the present study, unlike in the previous one. Furthermore, the rabbits used in this study did not present weight loss or changes in behavior such as loss of appetite or decrease in water intake. Mashiba and colleagues[39] treated their rabbits with PTH at 10 µg/kg/day for 35 and 70 days, and both control and PTH groups showed normal body weight gain, with no significant difference between them. Hirano and colleagues[30] found a small decrease in weight after dosing their rabbits at 40 µg/kg/day 5 days a week for 20 weeks. On the other hand, the rabbits that were treated with PTH at 10 µg/kg/day 5 days a week for 20 weeks showed a small increase in body weight. An increase in body weight was also found in their control rabbits. In our previous LER study, the rabbits showed overall weight loss between week 0 and week 4, which we also observed in another (*ex vivo*; no LER assessment) study by our group, *ex vivo* PTH_previous(b).[27] However, in our previous LER study, when radiation dose groups were compared, no difference in weight was found. These rabbits also did not show changes in behavior, such as loss of appetite and decrease in water intake.

We did not have a control group in the present study, which certainly is a limitation. However, in our *ex vivo* PTH_previous(b) study,[27] we had a sham ovariectomy control (SHAM) group that showed very low Ac.f compared with the PTH group (14.2-fold increase). In our PTH group, we measured 350 BMUs in 7 rabbits, which is equal to 50 BMUs/rabbit. Thus, if we used a similar control group in the present study with 7 rabbits and Ac.f was 1/14.2 that of PTH, it would only provide 3.5 BMUs/rabbit As the objective of the present research was to study the effect of PTH on LER and the use of a control was not feasible due to the low remodeling rate, we adopted a withdrawal model as an alternative. This approach had the advantage of increasing remodeling in a similar manner in both groups from the beginning of the experiment. The withdrawal group, although certainly not a control, represents a return towards a more normal state, with the caveat that the continuing effects cannot be ruled out and certainly warrant further

study. A second limitation to be considered is the fact that we used different modalities for *in vivo* and *ex vivo* imaging. However, multiple *in vivo* assessments would increase the complexity of the experiment for several reasons that include acquiring two different synchrotron beam time allotments in a short time interval and, more importantly, would have increased the animals' radiation exposure.

Another limitation in our study is that certain assumptions such as PTH increasing Ac.f and On.MAR, are based only on our previous work and others in the literature. Because of the pandemic, we were not able to perform a histology analysis in this study. We have ensured registration repeatability in our method, which means that the entire 3D registration was repeated by the same operator under the same conditions and using the same measurement procedure. However, we have not yet measured the reproducibility (the degree of agreement between the 3D registrations measured by different individuals), representing another limitation.

The present study is the first to study the impact of PTH on LER progression. Counter to our hypothesis, we found that LER was lower in the actively dosed PTH group and higher in the PTHW group. This apparent slowing of BMU progression by PTH has intriguing implications for BMU dynamics. This finding suggests that PTH slows the cutting cone advancement but speeds up that of the closing cone. We thus hypothesize that PTH shortens the size of the resorption-reversal phase and decreases the volume of remodeling-related resorption spaces, yielding an overall positive bone balance despite increased Ac.f. Therefore, this study shows that slowing of BMU progression could play an essential role in how PTH enhances coupling and produces an overall anabolic outcome despite transient increases in porosity. This makes PTH a powerful drug to treat osteoporosis. Further investigation into LER modulation is warranted, with potential benefits for treating remodeling-related diseases, improving treatment, and possibly reducing the adverse effects of drugs.

3.5. Supplementary Materials

Figure 3.10 (A) shows the histogram of LER and (B) the mean LER by group in the present study and in the LER PTH_previous(a) study.[37] LER was higher in the present study (PTH = 34.61 µm/day and PTHW = 39.37 µm/day) compared with the previous PTH study (LER PTH_previous(a) = 23.8 µm/day). The discrepancy between studies can be attributed to the

differences within species, such as the cortical bone microarchitecture variation. However, it can also be attributed to a sampling issue. As it is shown in Figure 3.10 A, the present study measured more BMUs (651 BMUs) compared with our first PTH-previous(a) (186 BMUs) study. A few high LER values from PTH and PTHW in the distribution could shift from the mean to the right side of the graph.

A

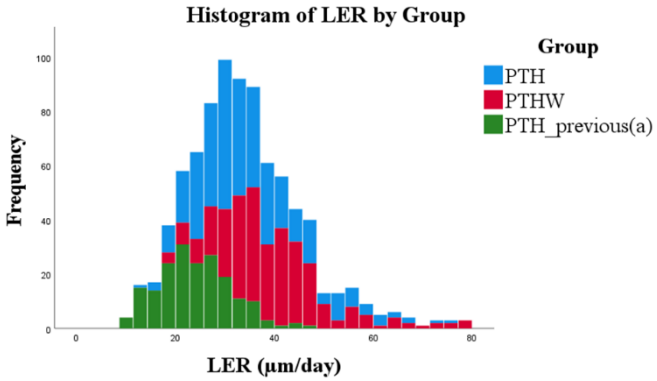

B

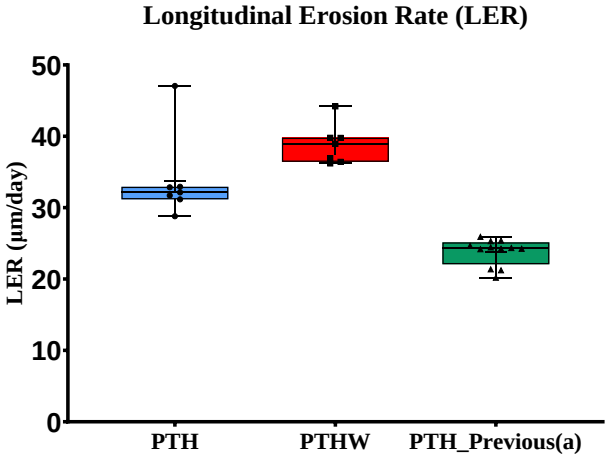

Figure 3.10. Comparison of LER in PTH and PTHW groups with our previous work (LER PTH_previous(a)[37]). (A) Histogram of LER distribution for PTH (N = 350), PTHW (N = 301) and PTH_previous(a) = 186. (B) LER data are presented as boxplot with median, interquartile range, max and min values plotted as dots, and mean as a cross.

In the present study, the region of interest was larger (View #1 + View #2 ~ 19 mm) than that used in LER PTH_previous(a)[37] (View #1 ~ 10 mm). We sought to rule out the possibility of LER variation along the diaphysis. Figure 3.11 A shows LER distribution and Figure 3.11 B the

numbers of BMUs by group in the present study by the mid Z coordinate position along the diaphysis. LER was equally distributed along the diaphysis in both PTH and PTHW. The total numbers of BMUs were also equally distributed in PTH (View #1 = 178 and View #2 = 172), whereas PTHW showed a higher number of BMUs in View #2 (n = 182) compared with View # 1 (n = 119). However, the total number of BMUs were not different by view ($p = 0.606$) or group ($p = 0.534$). We have also analyzed LER direction as going up to the proximal region (Z2 - Z1/t2 – t1 > 0 = + LER) and going down to the distal region (Z2 - Z1/t2 - t1> 0 = - LER) along the diaphysis (Figure 3.11 C). We have not found differences in the BMU direction along the diaphysis in both PTH and PTHW (Table 3.2 and Figure 3.11 C). However, when we divided the analysis by scan view, we found that PTH showed differences in - LER in View# 1 and View 2 ($p = 0.027$) and + LER in View#1 and View#2 ($p = 0.027$) (Table 3.3).

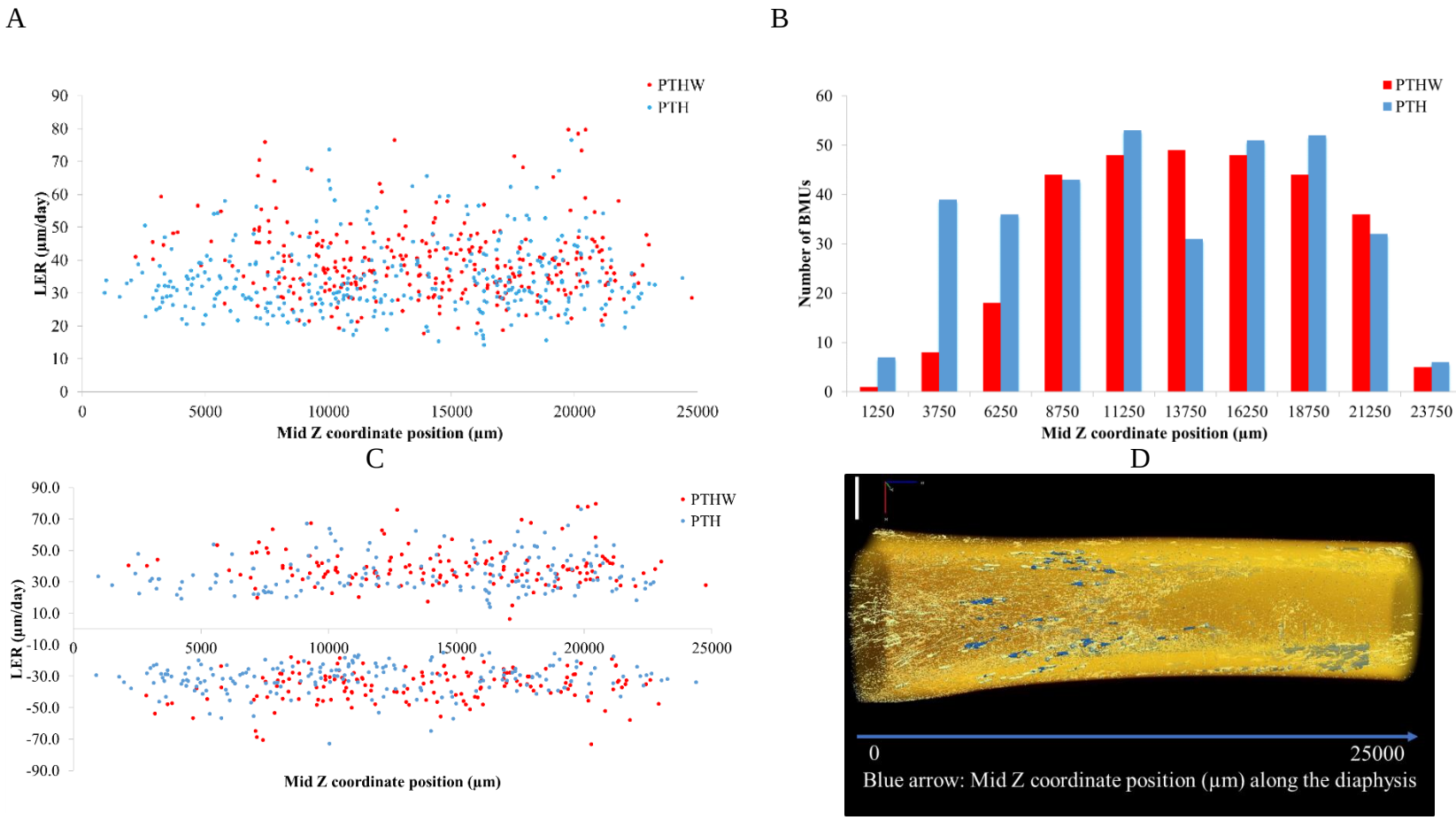

Figure 3.11. PTH and PTHW LER distribution (A), number of BMUs (B), and BMU direction (+LER going up to the proximal region and -LER going down to the distal region) (C) along the mid Z coordinate position in the rabbit tibia diaphysis (D).

Figure 3.12 shows comparisons of (A) cortical porosity, (B) canal diameter and (C) canal diameter distribution at 14 and 28 days of PTH dosing in the present study (PTH *vs.* PTHW) compared with the two previous studies (LER PTH_previous(a) and *ex vivo* PTH_previous(b)) conducted by our group. Previous(a)[37] was our first LER study using PTH to increase the number of BMUs, and the data were collected *in vivo* at 14 days and *ex vivo* at 28 days of PTH dosing. Previous(b)[27] was our first PTH rabbit study in which the rabbits were dosed for 28 days, and the data were collected *ex vivo*.

At 14 days mean Ct.Po was similar between PTH and PTHW, with PTH_previous(a)_Day 14 showing a high variation attributed to a microarchitecture difference between rabbits. At 28 days, mean Ct.Po was similar between PTH, LER PTH_previous(a)_Day 28, and *ex vivo* PTH_previous(b)_Day 28, again with LER PTH_previous(a)_Day 28 showing high variation. We used an automatic threshold to segment the pores in the present study. However, LER PTH_previous(a) and *ex vivo* PTH_previous(b) used the same fixed global threshold value. Therefore, the high degree of variation in the LER PTH_previous(a) study can be explained by differences in cortical bone microarchitecture between rabbits. Regarding mean Ca.Dm both PTH and PTHW showed decreased values between 14 and 28 days. As explained before, this decrease can be attributed to the scan resolution and type of segmentation used in the present study. On the other hand, the mean Ca.Dm in the LER PTH_previous(a) study at 14 days and 28 days was similar. Comparing Ca.Dm between studies at 28 days, the present study and LER PTH_previous(a) showed similar values. All studies showed a similar peak in Ca.Dm distribution (Figure 3.12 C) at 100 μm.

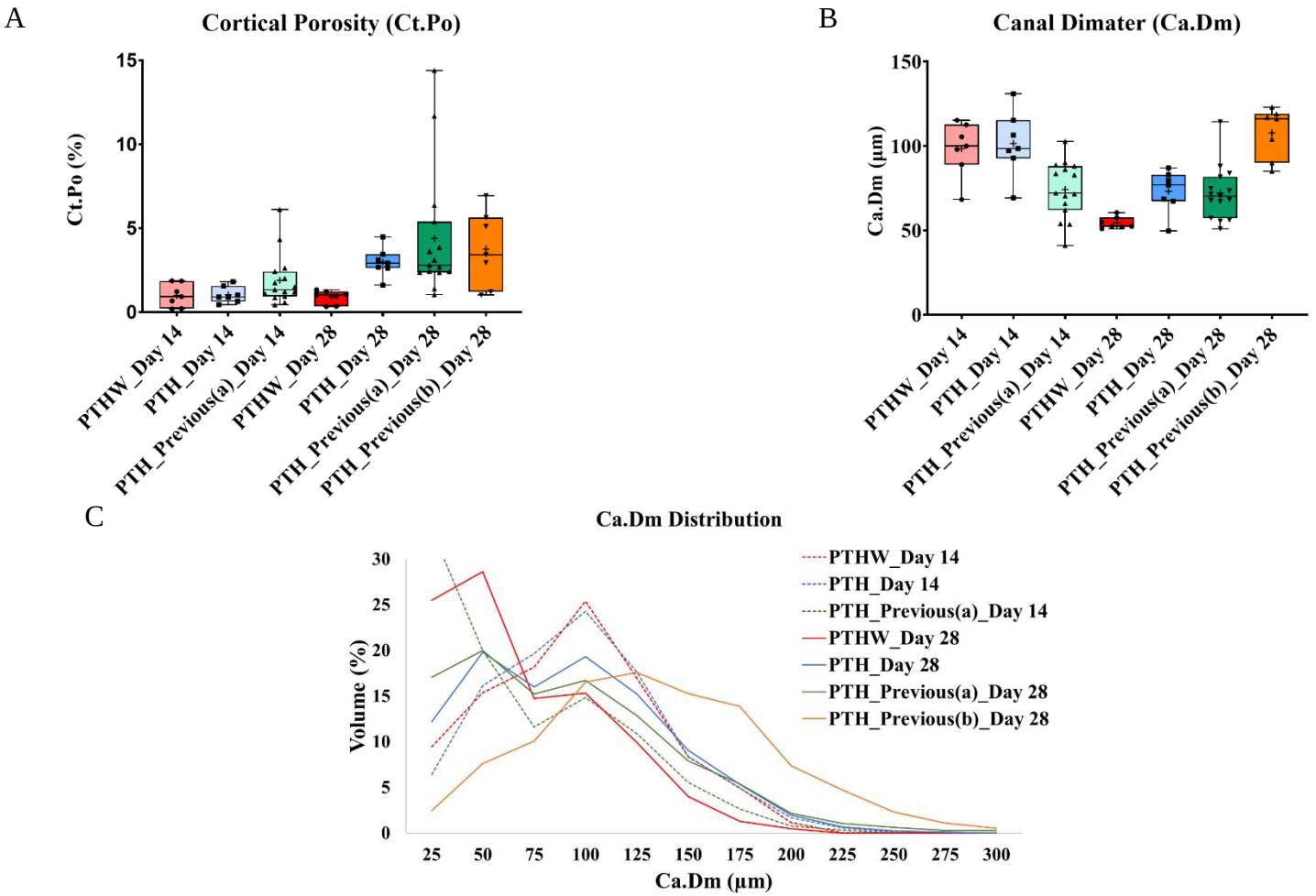

Figure 3.12. (A-C) Comparison of cortical porosity (Ct.Po), canal diameter (Ca.Dm) and Ca.Dm distribution in rabbit tibiae of PTH and PTHW groups, and with our two previous work (LER PTH_previous(a)[37] and ex vivo PTH_previous(b)[27]). All data were compared at 28 days.

CHAPTER 4. Conclusion

4.1. Thesis Overview

The rate of progression of a basic multicellular unit (BMU), their longitudinal erosion rate (LER), was first described by Jaworski and Lok[24] in 1972 using 2D double tetracycline labeling. Still, little is known about BMU spatio-temporal regulation. This knowledge gap is due to a lack of efficient 3D methodologies that include a suitable 3D imaging technique that balances high resolution and radiation dose and accommodates a preclinical model that exhibits cortical remodeling.[21,27] Our group has developed a novel approach combining longitudinal *in vivo* synchrotron-based phase-contrast micro-CT in association with a parathyroid hormone (PTH) rabbit model.[37] PTH is well documented in the literature to exert both catabolic (increased resorption) and anabolic (increased bone formation) actions on the cortical bone of rabbits.[27,30,39,127,128] These complex effects can be reconciled by the interpretation that PTH increases the rate of remodeling – both the creation of new BMUs (activation frequency, Ac.f) and the rate of formative activities (osteonal mineral apposition rate, On.MAR).[27] However, how PTH affects BMU spatio-temporal behavior is unknown, warranting further investigation. In the classic studies from the 1970s[24–26] and ‘80s,[7] LER was inferred using 2D double tetracycline labeling. The measure was based on an assumed steady state where the cutting cone progression is equal to that of the closing cone. Based on this assumption, Parfitt[7] postulated that LER could be calculated as the length of the closing cone divided by the time required for the radial infilling. In 2D sections, radial infilling is calculated from osteonal wall thickness divided by osteonal mineral apposition rate (On.MAR). If this spatio-temporal relationship is valid and constant, increasing On.MAR, as observed with PTH,[27–30] would concomitantly elevate LER. The aim of this thesis was to use the novel approach developed by our group to explore whether the increased On.MAR generated by PTH extends to the progression of individual BMUs. Specifically, I manipulated BMU progression via different dosing regimens: PTH and PTH withdrawal (PTHW). I hypothesized that LER would be higher during active dosing, as PTH is also known to increase On.MAR.[132]

Chapter 2 presents a literature review. It starts with a historical overview to consider how important terminologies in cortical bone that are still used today, such as the Haversian system,

Volkmann's canal, and Howship's lacunae, were discovered. Early studies on the Haversian system and Volkmann's canal led to the first description of a cortical BMU and the bone remodeling concepts used in modern biology. LER studies from the 1970s and '80s using 2D longitudinal sections with double-labeling techniques played an essential role in our fundamental understanding of BMU dynamics as we know them today. However, such studies were based on a steady state, where LER could be inferred considering a constant relationship between the cutting cone and the closing cone. Therefore, the amount of bone formed was equal to the amount of bone resorbed, and BMU functioned in ways that did not change over time. However, with new concepts of uncoupling between resorption and formation playing a role in bone loss, such an assumption is problematic. Advancement in X-ray imaging regarding resolution and radiation dose led our group to explore 4D (or 3D over time) imaging in the study of BMU progression.[22,28] 4D imaging can contribute to a better understanding of BMU regulation in disease states, including osteoporosis. The first trial was performed using rat forelimbs.[31] However, rats showed very little cortical remodeling leading our group to rabbits, which are known in the literature to exhibit cortical remodeling. However, because a normal rabbit has very few BMUs to be explored at any one time, it was necessary to increase the activation of BMUs. PTH is well known in the literature to increase cortical porosity in rabbits.[27,30,39,127,128] None of the studies presented in the literature examined how PTH impacts BMU progression, warranting further investigation, as PTH is used to treat osteoporosis in humans. Our group has combined PTH rabbits with *in vivo* synchrotron-based phase-contrast micro-CT to serve as a platform for more detailed analyses of how PTH affects spatio-temporal BMU regulation. The new methodology presented in this thesis offers new insights into how PTH impacts LER, which has significant clinical relevance in understanding PTH's complex actions that could, in turn, lead to strategies to improve responsiveness to PTH therapy.

Chapter 3 presents the main experimental study, which aimed to investigate the spatio-temporal behavior of BMUs (specifically, LER in 4D) in the cortical bone of PTH-dosed rabbits. LER was quantified in PTH and PTH withdrawal (PTHW) groups and compared over 14 days. The hypothesis was that PTH would elevate LER as this agent is known to increase bone formation. The mean PTHW LER was higher than PTH, countering the thesis hypothesis. The thesis results suggest that PTH enhances the coupling between resorption and formation by slowing cutting cone advancement and speeding up bone formation. Therefore, the size of the

reversal-resorption phase can be shorter and thus the time required to reach the postulated cellular density to switch from reversal-resorption phase to formation, which consequently decreases the overall volume of the remodeling space, yielding a positive bone balance despite increased Ac.f. The results presented in this thesis suggest that slowing BMU progression could play an important role in how PTH produces an overall anabolic outcome despite transient increases in porosity, which makes PTH a powerful drug to treat osteoporosis. This apparent slowing of BMU progression by PTH has intriguing implications for BMU dynamics, and further investigation is warranted, consequently for combatting remodeling-related diseases.

4.2. Future Directions

Our group's new method has been established as a platform by which cortical bone remodeling can be tracked and studied. My thesis is the first to use this model to manipulate BMU behavior and shed light on how PTH affects BMU coordination in time and space. This study has clinical relevance, as PTH is an anabolic agent used to treat osteoporosis. Other aspects of PTH's actions on bone remodeling, such as its combination with antiresorptive agents, can be investigated using the novel approach employed in this thesis. Experiments utilizing this platform could involve the following:

1. Studying the temporal nature of PTH bone effects *in vivo* at multiple time points to detect changes in microarchitecture and geometry over time. Researchers state that the anabolic window induced by PTH occurs early in treatment.[152,153] Thus, PTH anabolic effects would be maximal at early time points during the experiment, and this hypothesis could be tested.
2. Studying PTH low-dose regimens to maximize the beneficial aspects of PTH while minimizing the negative. Our group has been dosing the rabbits at 30 µg/day, and results have shown that PTH highly increased cortical porosity. Using this model approach, we could compare BMU behaviour using PTH at 20 µg/day (dose used to treat osteoporotic patients) and at 10 µg/day (lower dose employed in rabbits[30,39]), which could be translated into the clinical setting and improve osteoporosis treatment.

In addition to the PTH-rabbits, other clinically relevant models, such as ovariectomized (OVX) rabbits, can be used to study the actions of glucocorticoids (GC) and osteoporosis treatments in BMU behavior. Currently, we have two projects in progress in this regard.

1. Investigation of glucocorticoids. OVX, GC, OVX+GC, and sham OVX control (SHAM) rabbits combined with longitudinal *in vivo* synchrotron-based phase-contrast micro-CT. During my master's, I had the opportunity to work on these experiments performed at the Canadian Light Source, where the rabbits' right tibiae were imaged at 14 days *in vivo* and then imaged *ex vivo* (post-mortem) after 28 days of GC dosing. This study outcome will give more insights into how GC affects BMU uncoupling. A second outcome is regarding how estrogen suppression affects BMU behaviour.
2. Investigation of antiresorptive (alendronate) and anabolic (PTH) agents using OVX, OVX+Alendronate, and OVX+PTH rabbits combined with longitudinal *in vivo* synchrotron-based phase-contrast micro-CT. This study aims to examine BMU behavior using the two main osteoporosis agents in varied doses (clinical and higher). The hypothesis is that alendronate will slow and/or stop BMU progression and inhibit the initiation of new BMUs, whereas PTH will slow BMU progression and enhance formation.

Another relevant topic for future study is 3D BMU-related resorption space morphology or BMU shape analysis. Our BMU data can provide a more comprehensive measurement of each remodeling phase, such as the length and radius of the cutting cone and reversal zone. Such measures can indicate the changes in volume within each phase, and their slope will give the radial rate of changes. Such analysis can provide more insights into how bone resorption and formation are spatially and temporarily synchronized in diseases states, as well as the impact of drug interventions such as GC, alendronate, and PTH. This project is also in progress.

In summary, this thesis represents the first application of a 4D method that enables the study of BMUs behavior and establishes it as a platform to study cortical bone remodeling. LER was higher in PTHW than in PTH, counter to the thesis hypothesis. This find suggests that PTH slows cutting cone advancement while simultaneously speeding up the advancement of closing cone, making the reversal-resorption phase shorter. The new insights into BMU dynamics gained from this work indicate a novel way in which PTH enhances coupling that is beyond increased formation, which yields an overall positive bone balance despite an increase in cortical porosity.

This makes PTH a powerful treatment for osteoporosis. Further investigation of BMU modulation is warranted, with potential implications for combatting remodeling-related disease, improving treatment, and potentially reducing drug adverse effects.

REFERENCES

1. Feng X, McDonald JM. Disorders of bone remodeling. Annu. Rev. Pathol. 2011;6:121–45.
2. No Title [Internet]. Available from: https://osteoporosis.ca
3. Shreyasse A. Epidemiology of Fractures. In: Orwoll ES, Bilezikian JP, Vanderschueren D, editors. Osteoporos. Men Eff. Gend. Skelet. Heal. Elsevier Inc.; 2010. p. 351–60.
4. Kendler DL, Adachi JD, Brown JP, Juby AG, Kovacs CS, Duperrouzel C, McTavish RK, Cameron C, Slatkovska L, Burke N. A scorecard for osteoporosis in Canada and seven Canadian provinces. Osteoporos. Int. [Internet]. 2021;32(1):123–32. Available from: https://doi.org/10.1007/s00198-020-05554-2
5. Burr DB. Bone Morphology and Organization. In: Burr Da, Allen M, editors. Basic Appl. Bone Biol. Second. Academic Press; 2019. p. 3–26.
6. Frost HM. Tetracycline-based histological analysis of bone remodeling. Calcif. Tissue Res. [Internet]. 1969;3(1):211–37. Available from: https://doi.org/10.1007/BF02058664
7. Parfitt AM. The physiologic and clinical significance of bone histomorphometric data. Bone Histomorphometry Tech. Interpret. [Internet]. CRC Press; 1983;143–223. Available from: http://ci.nii.ac.jp/naid/10012405084/en/
8. Parfitt AM. Osteonal and hemi-osteonal remodeling: the spatial and temporal framework for signal traffic in adult human bone. J. Cell. Biochem. United States; 1994 Jul;55(3):273–86.
9. Raggatt LJ, Partridge NC. Cellular and molecular mechanisms of bone remodeling. J. Biol. Chem. 2010 Aug;285(33):25103–8.
10. Allen M, Burr DB. Bone Growth, Modeling and Remodeling. In: Burr DB, Allen M, editors. Basic Appl. Bone Biol. Second. Academic Press; 2019. p. 85–100.
11. Gasser JA, Kneissel M. Bone physiology and biology. Mol. Integr. Toxicol. [Internet]. 2017. p. 27–94. Available from: http://link.springer.com/10.1007/978-3-319-56192-9_2
12. Dempster DW. Tethering Formation to Resorption: Reversal Revisited. J. Bone Miner. Res. [Internet]. 2017;32(7):1389–90. Available from: http://www.ncbi.nlm.nih.gov/pubmed/28498616
13. Langdahl B. Pathophysiology of Osteoporosis. Osteoporos. Sarcopenia [Internet]. 2018

Dec;4(4):S2. Available from: https://linkinghub.elsevier.com/retrieve/pii/S240552551830102X

14. Canalis E, Delany AM. Mechanisms of glucocorticoid action in bone. Ann. N. Y. Acad. Sci. [Internet]. 2002 Jun;966:73–81. Available from: http://www.ncbi.nlm.nih.gov/pubmed/12114261
15. Alejandro P, Constantinescu F. A Review of Osteoporosis in the Older Adult. Rheum. Dis. Clin. North Am. [Internet]. 2018 Aug;44(3):437–51. Available from: https://linkinghub.elsevier.com/retrieve/pii/S0889857X18300292
16. Bandeira L, Bilezikian JP. Novel Therapies for Postmenopausal Osteoporosis. Endocrinol. Metab. Clin. North Am. [Internet]. 2017 Mar;46(1):207–19. Available from: https://linkinghub.elsevier.com/retrieve/pii/S0889852916301232
17. Lyu H, Jundi B, Xu C, Tedeschi SK, Yoshida K, Zhao S, Nigwekar SU, Leder BZ, Solomon DH. Comparison of Denosumab and Bisphosphonates in Patients With Osteoporosis: A Meta-Analysis of Randomized Controlled Trials. J. Clin. Endocrinol. Metab. [Internet]. 2019 May 1;104(5):1753–65. Available from: https://academic.oup.com/jcem/article/104/5/1753/5235617
18. Zebaze RM, Libanati C, Austin M, Ghasem-Zadeh A, Hanley DA, Zanchetta JR, Thomas T, Boutroy S, Bogado CE, Bilezikian JP, Seeman E. Differing effects of denosumab and alendronate on cortical and trabecular bone. Bone [Internet]. 2014 Feb;59:173–9. Available from: https://linkinghub.elsevier.com/retrieve/pii/S8756328213004778
19. Silva BC, Costa AG, Cusano NE, Kousteni S, Bilezikian JP. Catabolic and anabolic actions of parathyroid hormone on the skeleton. J. Endocrinol. Invest. [Internet]. 2011 Nov;34(10):801–10. Available from: http://www.ncbi.nlm.nih.gov/pubmed/21946081
20. Jiang Y, Zhao JJ, Mitlak BH, Wang O, Genant HK, Eriksen EF. Recombinant human parathyroid hormone (1-34) [teriparatide] improves both cortical and cancellous bone structure. J. bone Miner. Res. Off. J. Am. Soc. Bone Miner. Res. United States; 2003 Nov;18(11):1932–41.
21. Dempster DW, Cosman F, Kurland ES, Zhou H, Nieves J, Woelfert L, Shane E, Plavetić K, Müller R, Bilezikian J, Lindsay R. Effects of Daily Treatment with Parathyroid Hormone on Bone Microarchitecture and Turnover in Patients with Osteoporosis: A Paired Biopsy Study*. J. Bone Miner. Res. [Internet]. 2001 Oct 1;16(10):1846–53.

Available from: http://doi.wiley.com/10.1359/jbmr.2001.16.10.1846

22. Vahle JL, Sato M, Long GG, Young JK, Francis PC, Engelhardt JA, Westmore MS, Ma YL, Nold JB. Skeletal Changes in Rats Given Daily Subcutaneous Injections of Recombinant Human Parathyroid Hormone (1-34) for 2 Years and Relevance to Human Safety. Toxicol. Pathol. [Internet]. 2002 Apr 2;30(3):312–21. Available from: http://journals.sagepub.com/doi/10.1080/01926230252929882
23. Miller PD, Lewiecki EM, Krohn K, Schwartz E. Teriparatide: Label changes and identifying patients for long-term use. Cleve. Clin. J. Med. [Internet]. 2021 Sep 1;88(9):489–93. Available from: https://www.ccjm.org//lookup/doi/10.3949/ccjm.88a.21011
24. Jaworski ZF, Lok E. The rate of osteoclastic bone erosion in Haversian remodeling sites of adult dog's rib. Calcif. Tissue Res. [Internet]. 1972;10(1):103–12. Available from: https://doi.org/10.1007/BF02012540
25. Takahashi H, Norimatsu H. The longitudinal and transverse rate of resorption of the Haversian systems in canine bone. In: Jaworski Z, editor. First Work. Bone Morphometry. Univ Ottawa Pres; 1976. p. 143–7.
26. Jaworski ZF, Lok E, Wellington JL. Impaired osteoclastic function and linear bone erosion rate in secondary hyperparathyroidism associated with chronic renal failure. Clin. Orthop. Relat. Res. United States; 1975;(107):298–310.
27. Harrison KD, Hiebert BD, Panahifar A, Andronowski JM, Ashique AM, King GA, Arnason T, Swekla KJ, Pivonka P, Cooper DM. Cortical Bone Porosity in Rabbit Models of Osteoporosis. J. Bone Miner. Res. [Internet]. 2020 Nov 22;35(11):2211–28. Available from: https://onlinelibrary.wiley.com/doi/10.1002/jbmr.4124
28. Dempster DW, Cosman F, Zhou H, Nieves JW, Bostrom M, Lindsay R. Effects of Daily or Cyclic Teriparatide on Bone Formation in the Iliac Crest in Women on No Prior Therapy and in Women on Alendronate. J. Bone Miner. Res. [Internet]. 2016 Aug;31(8):1518–26. Available from: https://onlinelibrary.wiley.com/doi/10.1002/jbmr.2822
29. Ma YL, Zeng QQ, Chiang AY, Burr D, Li J, Dobnig H, Fahrleitner-Pammer A, Michalská D, Marin F, Pavo I, Stepan JJ. Effects of teriparatide on cortical histomorphometric variables in postmenopausal women with or without prior alendronate treatment. Bone

[Internet]. 2014 Feb;59:139–47. Available from: https://linkinghub.elsevier.com/retrieve/pii/S8756328213004729

30. Hirano T, Burr DB, Turner CH, Sato M, Cain RL, Hock JM. Anabolic Effects of Human Biosynthetic Parathyroid Hormone Fragment (1-34), LY333334, on Remodeling and Mechanical Properties of Cortical Bone in Rabbits. J. Bone Miner. Res. [Internet]. 1999 Apr 1;14(4):536–45. Available from: http://doi.wiley.com/10.1359/jbmr.1999.14.4.536
31. Harrison KD, Cooper DML. Modalities for Visualization of Cortical Bone Remodeling: The Past, Present, and Future. Front. Endocrinol. (Lausanne). [Internet]. 2015 Aug 11;6. Available from: http://journal.frontiersin.org/Article/10.3389/fendo.2015.00122/abstract
32. Pratt I V, Belev G, Zhu N, Chapman LD, Cooper DML. In vivo imaging of rat cortical bone porosity by synchrotron phase contrast micro computed tomography. Phys. Med. Biol. England; 2015 Jan;60(1):211–32.
33. Cheung AM, Adachi JD, Hanley DA, Kendler DL, Davison KS, Josse R, Brown JP, Ste-Marie L-G, Kremer R, Erlandson MC, Dian L, Burghardt AJ, Boyd SK. High-resolution peripheral quantitative computed tomography for the assessment of bone strength and structure: a review by the Canadian Bone Strength Working Group. Curr. Osteoporos. Rep. 2013 Jun;11(2):136–46.
34. Whittier DE, Boyd SK, Burghardt AJ, Paccou J, Ghasem-Zadeh A, Chapurlat R, Engelke K, Bouxsein ML. Guidelines for the assessment of bone density and microarchitecture in vivo using high-resolution peripheral quantitative computed tomography. Osteoporos. Int. [Internet]. 2020 Sep 26;31(9):1607–27. Available from: https://link.springer.com/10.1007/s00198-020-05438-5
35. Cooper DML, Turinsky AL, Sensen CW, Hallgrímsson B. Quantitative 3D analysis of the canal network in cortical bone by micro-computed tomography. Anat. Rec. - Part B New Anat. [Internet]. 2003 Sep;274(1):169–79. Available from: http://doi.wiley.com/10.1002/ar.b.10024
36. Ford NL, Thornton MM, Holdsworth DW. Fundamental image quality limits for microcomputed tomography in small animals. Med. Phys. United States; 2003 Nov;30(11):2869–77.
37. Harrison K, Sales E, Hiebert B, Panahifar A, Zhu N, Arnason T, Pivonka P, Swekla K, Cooper D. Direct Four-Dimensional Assessment of Cortical Bone Basic Multicellular

Unit Longitudinal Erosion Rate in PTH-Dosed Rabbits: A Novel Synchrotron X-Ray Imaging Approach. J. Bone Miner. Res. BONE Miner. Res. WILEY; 2020. p. 275.

38. Komori T. Animal models for osteoporosis. Eur. J. Pharmacol. Netherlands; 2015 Jul;759:287–94.

39. Mashiba T, Burr D., Turner C., Sato M, Cain R., Hock J. Effects of human parathyroid hormone (1-34), LY333334, on bone mass, remodeling, and mechanical properties of cortical bone during the first remodeling cycle in rabbits. Bone [Internet]. 2001 May;28(5):538–47. Available from: https://linkinghub.elsevier.com/retrieve/pii/S8756328201004331

40. Baofeng L, Zhi Y, Bei C, Guolin M, Qingshui Y, Jian L. Characterization of a rabbit osteoporosis model induced by ovariectomy and glucocorticoid. Acta Orthop. 2010 Jun;81(3):396–401.

41. Leder BZ, Neer RM, Wyland JJ, Lee HW, Burnett-Bowie S-AM, Finkelstein JS. Effects of teriparatide treatment and discontinuation in postmenopausal women and eugonadal men with osteoporosis. J. Clin. Endocrinol. Metab. [Internet]. 2009 Aug;94(8):2915–21. Available from: http://www.ncbi.nlm.nih.gov/pubmed/19435827

42. Lindsay R, Scheele WH, Neer R, Pohl G, Adami S, Mautalen C, Reginster J-Y, Stepan JJ, Myers SL, Mitlak BH. Sustained Vertebral Fracture Risk Reduction After Withdrawal of Teriparatide in Postmenopausal Women With Osteoporosis. Arch. Intern. Med. [Internet]. 2004 Oct 11;164(18):2024. Available from: http://archinte.jamanetwork.com/article.aspx?doi=10.1001/archinte.164.18.2024

43. Leeuwenhoek A. Microscopical observations of the structure of Teeth and other Bones: made and communicated, in a letter by Mr. Anthony Leeuwenhoeck. Philos. Trans. R. Soc. London [Internet]. 1677 Mar 25;12(140):1002–3. Available from: https://royalsocietypublishing.org/doi/10.1098/rstl.1677.0052

44. Havers C. Osteologia Nova, Or Some New Observations of the Bones, and the Parts Belonging to Them [Internet]. Lea P: B and, editor. London : Printed for Samuel Smith ...; 1845. Available from: https://books.google.co.uk/books?id=j_hbAAAAcAAJ

45. Bir SC, Kalakoti P, Notarianni C, Nanda A. John Howship (1781-1841) and growing skull fracture: historical perspective. J. Neurosurg. Pediatr. [Internet]. 2015 Oct;16(4):472–6. Available from: http://www.ncbi.nlm.nih.gov/pubmed/26186359

46. Howship J. Experiments and Observations in order to ascertain the means employed by the animal economy in the formation of bone. Med. Chir. Trans. [Internet]. 1815;6:263-676.5. Available from: http://www.ncbi.nlm.nih.gov/pubmed/20895250
47. Howship J. Observations on the morbid structure of Bones, and an attempt at an arrangement of their Diseases. Med. Chir. Trans. [Internet]. 1817;8:57-596.5. Available from: http://www.ncbi.nlm.nih.gov/pubmed/20895334
48. Todd RB. The physiological anatomy and physiology of man. [Internet]. Physiol. Anat. Physiol. man. 1845. Available from: https://play.google.com/books/reader?id=TUNJAAAAYAAJ&hl=en&pg=GBS.PA109
49. Tomes J, De Morgan C. The Structure and Development of Bone. Am. J. Dent. Sci. 1853 Apr;3(3):447–53.
50. Jaffe HL. The Vessel Canals in Normal and Pathological Bone. Am. J. Pathol. [Internet]. 1929 May;5(3):323-332.5. Available from: http://www.ncbi.nlm.nih.gov/pubmed/19969855
51. Kölliker A von. Die normale Resorption des Knochengewebes und ihre Bedeutung für die Entstehung der typischen Knochenformen [Internet]. Leipzig: von F.C.W. Vogel; 1873. Available from: http://archive.org/details/b22392610
52. Stöhr's P, Lewis FT. Stöhr's histology : arranged upon an embroyological basis. Philadelphia: P. Blakiston's Son & Co.; 1906.
53. Jaffe HL. The Resorption of Bone. Arch. Surg. [Internet]. 1930 Mar 1;20(3):355. Available from: http://archsurg.jamanetwork.com/article.aspx?doi=10.1001/archsurg.1930.01150090002001
54. McLean FC, Rowland RE. Internal remodeling of compact bone. Mech. Hard Tissue Destr. AAAS, Washington; 1963. p. 371–83.
55. Johnson L. Morphological analysis of pathology. Frost HM, Ed. Bone Biodyn. Boston: Little, Brown; 1964. p. 543–654.
56. Frost HM (Harold M. The bone dynamics in osteoporosis and osteomalacia. Springfield, Ill.: Springfield, Ill. : Thomas; 1966.
57. Baron R. Importance of the intermediate phases between resorption and formation in the measurement and understanding of the bone remodeling sequence. In: Meunier P, editor.

Bone Histomorphometry Second Int. Work. Lyon Armour Montagu. Toulouse; 1977. p. 179–83.

58. Andersen TL, Abdelgawad ME, Kristensen HB, Hauge EM, Rolighed L, Bollerslev J, Kjærsgaard-Andersen P, Delaisse J-M. Understanding Coupling between Bone Resorption and Formation. Am. J. Pathol. [Internet]. 2013 Jul;183(1):235–46. Available from: https://linkinghub.elsevier.com/retrieve/pii/S0002944013002629
59. Lassen NE, Andersen TL, Pløen GG, Søe K, Hauge EM, Harving S, Eschen GET, Delaisse J-M. Coupling of Bone Resorption and Formation in Real Time: New Knowledge Gained From Human Haversian BMUs. J. Bone Miner. Res. [Internet]. 2017 Jul;32(7):1395–405. Available from: http://www.ncbi.nlm.nih.gov/pubmed/28177141
60. Jaworski ZF, Meunier P, Frost HM. Observations on two types of resorption cavities in human lamellar cortical bone. Clin. Orthop. Relat. Res. United States; 1972;83:279–85.
61. Andersen TL, Hauge EM, Rolighed L, Bollerslev J, Kjærsgaard-Andersen P, Delaisse J-M. Correlation between Absence of Bone Remodeling Compartment Canopies, Reversal Phase Arrest, and Deficient Bone Formation in Post-Menopausal Osteoporosis. Am. J. Pathol. [Internet]. 2014 Apr;184(4):1142–51. Available from: https://linkinghub.elsevier.com/retrieve/pii/S0002944014000108
62. Cohen J, Harris WH. The three-dimensional anatomy of haversian systems. J. Bone Joint Surg. Am. United States; 1958 Apr;40-A(2):419–34.
63. Tappen NC. Three-dimensional studies on resorption spaces and developing osteons. Am. J. Anat. United States; 1977 Jul;149(3):301–17.
64. Robling AG, Stout SD. Morphology of the drifting osteon. Cells. Tissues. Organs. Switzerland; 1999;164(4):192–204.
65. Stout SD, Brunsden BS, Hildebolt CF, Commean PK, Smith KE, Tappen NC. Computer-Assisted 3D Reconstruction of Serial Sections of Cortical Bone to Determine the 3D Structure of Osteons. Calcif. Tissue Int. [Internet]. 1999 Oct 6;65(4):280–4. Available from: http://link.springer.com/10.1007/s002239900699
66. Andreasen CM, Delaisse J-M, van der Eerden BC, van Leeuwen JP, Ding M, Andersen TL. Understanding Age-Induced Cortical Porosity in Women: The Accumulation and Coalescence of Eroded Cavities Upon Existing Intracortical Canals Is the Main Contributor. J. Bone Miner. Res. [Internet]. 2018;33(4):606–20. Available from:

http://www.ncbi.nlm.nih.gov/pubmed/29193312

67. Genant HK, Gordon C, Jiang Y, Link TM, Hans D, Majumdar S, Lang TF. Advanced imaging of the macrostructure and microstructure of bone. Horm. Res. 2000;54(SUPPL. 1):24–30.

68. Feldkamp LA, Goldstein SA, Parfitt AM, Jesion G, Kleerekoper M. The direct examination of three-dimensional bone architecture in vitro by computed tomography. J. Bone Miner. Res. United States; 1989 Feb;4(1):3–11.

69. Kuhn JL, Goldstein SA, Feldkamp LA, Goulet RW, Jesion G. Evaluation of a microcomputed tomography system to study trabecular bone structure. J. Orthop. Res. Off. Publ. Orthop. Res. Soc. United States; 1990 Nov;8(6):833–42.

70. Cooper DML, Thomas CDL, Clement JG, Turinsky AL, Sensen CW, Hallgrímsson B. Age-dependent change in the 3D structure of cortical porosity at the human femoral midshaft. Bone [Internet]. 2007 Apr;40(4):957–65. Available from: https://linkinghub.elsevier.com/retrieve/pii/S8756328206008465

71. Basillais A, Bensamoun S, Chappard C, Brunet-Imbault B, Lemineur G, Ilharreborde B, Ho Ba Tho MC, Benhamou CL. Three-dimensional characterization of cortical bone microstructure by microcomputed tomography: Validation with ultrasonic and microscopic measurements. J. Orthop. Sci. 2007;12(2):141–8.

72. Cooper DML, Thomas CDL, Clement JG, Hallgrímsson B. Three-dimensional microcomputed tomography imaging of basic multicellular unit-related resorption spaces in human cortical bone. Anat. Rec. Part A Discov. Mol. Cell. Evol. Biol. [Internet]. 2006 Jul;288A(7):806–16. Available from: http://doi.wiley.com/10.1002/ar.a.20344

73. Britz HM, Jokihaara J, Leppanen OV, Jarvinen T, Cooper DML. 3D visualization and quantification of rat cortical bone porosity using a desktop micro-CT system: a case study in the tibia. J. Microsc. [Internet]. 2010 Oct;240(1):32–7. Available from: http://doi.wiley.com/10.1111/j.1365-2818.2010.03381.x

74. Pazzaglia UE, Zarattini G, Giacomini D, Rodella L, Menti AM, Feltrin G. Morphometric Analysis of the Canal System of Cortical Bone: An Experimental Study in the Rabbit Femur Carried Out with Standard Histology and Micro-CT. Anat. Histol. Embryol. [Internet]. 2010 Feb;39(1):17–26. Available from: http://doi.wiley.com/10.1111/j.1439-0264.2009.00973.x

75. Chen H, Zhou X, Shoumura S, Emura S, Bunai Y. Age- and gender-dependent changes in three-dimensional microstructure of cortical and trabecular bone at the human femoral neck. Osteoporos. Int. [Internet]. 2010 Apr 19;21(4):627–36. Available from: http://link.springer.com/10.1007/s00198-009-0993-z
76. Palacio-Mancheno PE, Larriera AI, Doty SB, Cardoso L, Fritton SP. 3D Assessment of Cortical Bone Porosity and Tissue Mineral Density Using High-Resolution μCT: Effects of Resolution and Threshold Method. J. Bone Miner. Res. [Internet]. 2014 Jan;29(1):142–50. Available from: http://doi.wiley.com/10.1002/jbmr.2012
77. Bousson V, Peyrin F, Bergot C, Hausard M, Sautet A, Laredo J-D. Cortical Bone in the Human Femoral Neck: Three-Dimensional Appearance and Porosity Using Synchrotron Radiation. J. Bone Miner. Res. [Internet]. 2004 Jan 19;19(5):794–801. Available from: http://doi.wiley.com/10.1359/jbmr.040124
78. Frost HM. Human Haversian System Measurements. Hosp. Med. Bull. 1961;9(1):145–7.
79. Maggiano IS, Maggiano CM, Clement JG, Thomas CDL, Carter Y, Cooper DML. Three-dimensional reconstruction of Haversian systems in human cortical bone using synchrotron radiation-based micro-CT: morphology and quantification of branching and transverse connections across age. J. Anat. [Internet]. 2016 May;228(5):719–32. Available from: http://www.ncbi.nlm.nih.gov/pubmed/26749084
80. Tjong W, Kazakia GJ, Burghardt AJ, Majumdar S. The effect of voxel size on high-resolution peripheral computed tomography measurements of trabecular and cortical bone microstructure. Med. Phys. 2012 Apr;39(4):1893–903.
81. Zhou S-A, Brahme A. Development of phase-contrast X-ray imaging techniques and potential medical applications. Phys. medica PM an Int. J. devoted to Appl. Phys. to Med. Biol. Off. J. Ital. Assoc. Biomed. Phys. Italy; 2008 Sep;24(3):129–48.
82. Arfelli F, Assante M, Bonvicini V, Bravin A, Cantatore G, Castelli E, Palma LD, Michiel M Di, Longo R, Olivo A, Pani S, Pontoni D, Poropat P, Prest M, Rashevsky A, Tromba G, Vacchi A, Vallazza E, Zanconati F. Low-dose phase contrast x-ray medical imaging. Phys. Med. Biol. [Internet]. 1998 Oct 1;43(10):2845–52. Available from: https://iopscience.iop.org/article/10.1088/0031-9155/43/10/013
83. Qin L, Raggatt LJ, Partridge NC. Parathyroid hormone: a double-edged sword for bone metabolism. Trends Endocrinol. Metab. [Internet]. 2004 Mar;15(2):60–5. Available from:

https://linkinghub.elsevier.com/retrieve/pii/S1043276004000074

84. Takahashi H, Hattner R, Epker BN, Frost HM. Evidence That Bone Resorption Precedes Formation At The Cellular Level. Henry Ford Hosp. Med. Bull. 1964;12(3):359–64.

85. Parfitt AM. The coupling of bone formation to bone resorption: a critical analysis of the concept and of its relevance to the pathogenesis of osteoporosis. Metab. Bone Dis. Relat. Res. France; 1982;4(1):1–6.

86. Charhon SA, Berland YF, Olmer MJ, Delawari E, Traeger J, Meunier PJ. Effects of parathyroidectomy on bone formation and mineralization in hemodialyzed patients. Kidney Int. [Internet]. 1985 Feb;27(2):426–35. Available from: http://www.ncbi.nlm.nih.gov/pubmed/2581010

87. O'Brien CA, Plotkin LI, Galli C, Goellner JJ, Gortazar AR, Allen MR, Robling AG, Bouxsein M, Schipani E, Turner CH, Jilka RL, Weinstein RS, Manolagas SC, Bellido T. Control of bone mass and remodeling by PTH receptor signaling in osteocytes. PLoS One. 2008 Aug;3(8):e2942.

88. Zhao W, Byrne MH, Boyce BF, Krane SM. Bone resorption induced by parathyroid hormone is strikingly diminished in collagenase-resistant mutant mice. J. Clin. Invest. [Internet]. 1999 Feb 15;103(4):517–24. Available from: http://www.jci.org/articles/view/5481

89. Richardson ML, Pozzi-Mucelli RS, Kanter AS, Kolb FO, Ettinger B, Genant HK. Bone mineral changes in primary hyperparathyroidism. Skeletal Radiol. [Internet]. 1986;15(2):85–95. Available from: https://doi.org/10.1007/BF00350200

90. Mautalen C, Reyes HR, Ghiringhelli G, Fromm G. Cortical bone mineral content in primary hyperparathyroidism. Changes after parathyroidectomy. Acta Endocrinol. (Copenh). Denmark; 1986 Apr;111(4):494–7.

91. Seeman E, Wahner HW, Offord KP, Kumar R, Johnson WJ, Riggs BL. Differential effects of endocrine dysfunction on the axial and the appendicular skeleton. J. Clin. Invest. [Internet]. 1982 Jun 1;69(6):1302–9. Available from: http://www.jci.org/articles/view/110570

92. Hesp R, Tellez M, Davidson L, Elton A, Reeve J. Trabecular and cortical bone in the radii of women with parathyroid adenomata: a greater trabecular deficit, with a preliminary assessment of recovery after parathyroidectomy. Bone Miner. Ireland; 1987 Jul;2(4):301–

10.

93. Parisien M, Silverberg SJ, Shane E, de la Cruz L, Lindsay R, Bilezikian JP, Dempster DW. The histomorphometry of bone in primary hyperparathyroidism: preservation of cancellous bone structure. J. Clin. Endocrinol. Metab. United States; 1990 Apr;70(4):930–8.
94. Parisien M, Mellish RW, Silverberg SJ, Shane E, Lindsay R, Bilezikian JP, Dempster DW. Maintenance of cancellous bone connectivity in primary hyperparathyroidism: trabecular strut analysis. J. Bone Miner. Res. United States; 1992 Aug;7(8):913–9.
95. Parisien M, Cosman F, Mellish RW, Schnitzer M, Nieves J, Silverberg SJ, Shane E, Kimmel D, Recker RR, Bilezikian JP. Bone structure in postmenopausal hyperparathyroid, osteoporotic, and normal women. J. bone Miner. Res. Off. J. Am. Soc. Bone Miner. Res. United States; 1995 Sep;10(9):1393–9.
96. Dempster DW, Parisien M, Silverberg SJ, Liang XG, Schnitzer M, Shen V, Shane E, Kimmel DB, Recker R, Lindsay R, Bilezikian JP. On the mechanism of cancellous bone preservation in postmenopausal women with mild primary hyperparathyroidism. J. Clin. Endocrinol. Metab. United States; 1999 May;84(5):1562–6.
97. Steiniche T, Christiansen P, Vesterby A, Ullerup R, Hessov I, Mosekilde LE, Melsen F. Primary hyperparathyroidism: bone structure, balance, and remodeling before and 3 years after surgical treatment. Bone. United States; 2000 May;26(5):535–43.
98. Dempster DW, Müller R, Zhou H, Kohler T, Shane E, Parisien M, Silverberg SJ, Bilezikian JP. Preserved three-dimensional cancellous bone structure in mild primary hyperparathyroidism. Bone [Internet]. 2007 Jul;41(1):19–24. Available from: https://linkinghub.elsevier.com/retrieve/pii/S8756328207003390
99. Bauer W, Aub JC, Albright F. Studies of Calcium and Phosphorus Metabolism: V. A Study of the Bone Trabeculae as a Readily Available Reserve Supply of Calcium. J. Exp. Med. 1929 Jan;49(1):145–62.
100. Dempster DW, Cosman F, Parisien M, Shen V, Lindday R. Anabolic Actions of Parathyroid Hormone on Bone*. Endocr. Rev. [Internet]. 1993 Dec;14(6):690–709. Available from: https://academic.oup.com/edrv/article-lookup/doi/10.1210/edrv-14-6-690
101. Selye H. On the Stimulation of New Bone-Formation with Parathyroid Extract and Irradiated Ergosterol. Endocrinology [Internet]. 1932 Sep;16(5):547–58. Available from:

https://academic.oup.com/endo/article-lookup/doi/10.1210/endo-16-5-547

102. Pugsley LI, Selye H. The histological changes in the bone responsible for the action of parathyroid hormone on the calcium metabolism of the rat. J. Physiol. 1933 Jul;79(1):113–7.

103. Jaffe H. Hyperparathyroidism (Recklinghausen's disease of bone). Arch Pathol. 1933;16:236–58.

104. Burrows RB. Variations produced in bones of growing rats by parathyroid extracts. Am. J. Anat. 1938;62(2):237–90.

105. Reeve J, Hesp R, Williams D, Hulme P, Klenerman L, Zanelli JM, Darby AJ, Tregear GW, Parsons JA. Anabolic effect of low doses of a fragment of human parathyroid hormone on the skeleton in postmenopausal osteoporosis. Lancet (London, England). England; 1976 May;1(7968):1035–8.

106. Reeve J, Meunier PJ, Parsons JA, Bernat M, Bijvoet OL, Courpron P, Edouard C, Klenerman L, Neer RM, Renier JC, Slovik D, Vismans FJ, Potts JT. Anabolic effect of human parathyroid hormone fragment on trabecular bone in involutional osteoporosis: a multicentre trial. Br. Med. J. [Internet]. 1980 Jun 7;280(6228):1340–4. Available from: http://www.ncbi.nlm.nih.gov/pubmed/6992932

107. Podbesek R, Edouard C, Meunier PJ, Parsons JA, Reeve J, Stevenson RW, Zanelli JM. Effects of two treatment regimes with synthetic human parathyroid hormone fragment on bone formation and the tissue balance of trabecular bone in greyhounds. Endocrinology. United States; 1983 Mar;112(3):1000–6.

108. Podesek R, Stevenson R, Zanelli G, Edovard C, Meunier P, Reeve J, Parsons J. Treatment with human parathyroid hormone fragment (hPTH 1-34) stimulates bone formation and intestinal calcium absorption in the greyhound: comparison with data from the osteoporosis trial. Horm. Control Calcium Metab. Excerpta Medica, Amsterdam,. 1980;118–23.

109. Tam CS, Heersche JN, Murray TM, Parsons JA. Parathyroid hormone stimulates the bone apposition rate independently of its resorptive action: differential effects of intermittent and continuous administration. Endocrinology. United States; 1982 Feb;110(2):506–12.

110. Hock JM, Gera I. Effects of continuous and intermittent administration and inhibition of resorption on the anabolic response of bone to parathyroid hormone. J. Bone Miner. Res.

United States; 1992 Jan;7(1):65–72.

111. Neer RM, Arnaud CD, Zanchetta JR, Prince R, Gaich GA, Reginster JY, Hodsman AB, Eriksen EF, Ish-Shalom S, Genant HK, Wang O, Mitlak BH. Effect of parathyroid hormone (1-34) on fractures and bone mineral density in postmenopausal women with osteoporosis. N. Engl. J. Med. [Internet]. 2001 May 10;344(19):1434–41. Available from: http://www.ncbi.nlm.nih.gov/pubmed/11346808
112. Hodsman AB, Bauer DC, Dempster DW, Dian L, Hanley DA, Harris ST, Kendler DL, McClung MR, Miller PD, Olszynski WP, Orwoll E, Yuen CK. Parathyroid Hormone and Teriparatide for the Treatment of Osteoporosis: A Review of the Evidence and Suggested Guidelines for Its Use. Endocr. Rev. [Internet]. 2005 Aug 1;26(5):688–703. Available from: https://academic.oup.com/edrv/article/26/5/688/2355192
113. "Drug Approval Package: Forteo [teriparatide (rDNA origin)] Injection; NDA #021318" [Internet]. U.S. Food Drug Adm. Available from: https://www.accessdata.fda.gov/drugsatfda_docs/nda/2002/21-318_Forteo.cfm
114. Hesp R, Hulme P, Williams D, Reeve J. The relationship between changes in femoral bone density and calcium balance in patients with involutional osteoporosis treated with human parathyroid hormone fragment (hPTH 1-34). Metab. Bone Dis. Relat. Res. 1981;2(5):331–4.
115. Slovik DM, Rosenthal DI, Doppelt SH, Potts JTJ, Daly MA, Campbell JA, Neer RM. Restoration of spinal bone in osteoporotic men by treatment with human parathyroid hormone (1-34) and 1,25-dihydroxyvitamin D. J. bone Miner. Res. Off. J. Am. Soc. Bone Miner. Res. United States; 1986 Aug;1(4):377–81.
116. Hodsman AB, Steer BM, Fraher LJ, Drost DJ. Bone densitometric and histomorphometric responses to sequential human parathyroid hormone (1-38) and salmon calcitonin in osteoporotic patients. Bone Miner. Ireland; 1991 Jul;14(1):67–83.
117. Ejersted C, Andreassen TT, Oxlund H, Jørgensen PH, Bak B, Häggblad J, Tørring O, Nilsson MH. Human parathyroid hormone (1-34) and (1-84) increase the mechanical strength and thickness of cortical bone in rats. J. bone Miner. Res. Off. J. Am. Soc. Bone Miner. Res. United States; 1993 Sep;8(9):1097–101.
118. Oxlund H, Ejersted C, Andreassen TT, Tørring O, Nilsson MH. Parathyroid hormone (1-34) and (1-84) stimulate cortical bone formation both from periosteum and endosteum.

Calcif. Tissue Int. United States; 1993 Dec;53(6):394–9.

119. Wronski TJ, Yen CF. Anabolic effects of parathyroid hormone on cortical bone in ovariectomized rats. Bone. United States; 1994;15(1):51–8.

120. Baumann BD, Wronski TJ. Response of cortical bone to antiresorptive agents and parathyroid hormone in aged ovariectomized rats. Bone. United States; 1995 Feb;16(2):247–53.

121. Mosekilde L, Danielsen CC, Søgaard CH, McOsker JE, Wronski TJ. The anabolic effects of parathyroid hormone on cortical bone mass, dimensions and strength--assessed in a sexually mature, ovariectomized rat model. Bone. United States; 1995 Feb;16(2):223–30.

122. Mackey MS, Stevens ML, Ebert DC, Tressler DL, Combs KS, Lowry CK, Smith PN, McOsker JE. The ferret as a small animal model with BMU-based remodeling for skeletal research. Bone [Internet]. 1995 Oct;17(4 Suppl):191S-196S. Available from: http://www.ncbi.nlm.nih.gov/pubmed/8579916

123. Jerome CP, Johnson CS, Lees CJ. Effect of treatment for 3 months with human parathyroid hormone 1-34 peptide in ovariectomized cynomolgus monkeys (Macaca fascicularis). Bone. United States; 1995 Oct;17(4 Suppl):415S-420S.

124. Inoue J. [Bone changes with long term administration of low dose 1-34 human PTH on adult beagles]. Nihon Seikeigeka Gakkai Zasshi. Japan; 1985 Apr;59(4):409–27.

125. Boyce RW, Paddock CL, Franks AF, Jankowsky ML, Eriksen EF. Effects of intermittent hPTH(1-34) alone and in combination with 1,25(OH)(2)D(3) or risedronate on endosteal bone remodeling in canine cancellous and cortical bone. J. bone Miner. Res. Off. J. Am. Soc. Bone Miner. Res. United States; 1996 May;11(5):600–13.

126. Delmas PD, Vergnaud P, Arlot ME, Pastoureau P, Meunier PJ, Nilssen MH. The anabolic effect of human PTH (1-34) on bone formation is blunted when bone resorption is inhibited by the bisphosphonate tiludronate--is activated resorption a prerequisite for the in vivo effect of PTH on formation in a remodeling system? Bone. United States; 1995 Jun;16(6):603–10.

127. Zebaze R, Takao-Kawabata R, Peng Y, Zadeh AG, Hirano K, Yamane H, Takakura A, Isogai Y, Ishizuya T, Seeman E. Increased cortical porosity is associated with daily, not weekly, administration of equivalent doses of teriparatide. Bone [Internet]. 2017 Jun;99:80–4. Available from:

https://linkinghub.elsevier.com/retrieve/pii/S8756328217301114

128. Yamane H, Takakura A, Shimadzu Y, Kodama T, Lee J-W, Isogai Y, Ishizuya T, Takao-Kawabata R, Iimura T. Acute development of cortical porosity and endosteal naïve bone formation from the daily but not weekly short-term administration of PTH in rabbit. Tintut Y, editor. PLoS One [Internet]. 2017 Apr 10;12(4):e0175329. Available from: https://dx.plos.org/10.1371/journal.pone.0175329

129. International Osteoporosis Foundation [Internet]. [cited 2021 May 31]. Available from: https://www.iofbonehealth.org

130. Khan AA, Morrison A, Kendler DL, Rizzoli R, Hanley DA, Felsenberg D, McCauley LK, O'Ryan F, Reid IR, Ruggiero SL, Taguchi A, Tetradis S, Watts NB, Brandi ML, Peters E, Guise T, Eastell R, Cheung AM, Morin SN, Masri B, Cooper C, Morgan SL, Obermayer-Pietsch B, Langdahl BL, Dabagh R Al, Davison KS, Sándor GK, Josse RG, Bhandari M, El Rabbany M, Pierroz DD, Sulimani R, Saunders DP, Brown JP, Compston J, International Task Force on Osteonecrosis of the Jaw. Case-Based Review of Osteonecrosis of the Jaw (ONJ) and Application of the International Recommendations for Management From the International Task Force on ONJ. J. Clin. Densitom. [Internet]. 20(1):8–24. Available from: http://www.ncbi.nlm.nih.gov/pubmed/27956123

131. Khow KSF, Shibu P, Yu SCY, Chehade MJ, Visvanathan R. Epidemiology and postoperative outcomes of atypical femoral fractures in older adults: A systematic review. J. Nutr. Health Aging [Internet]. 2017 Jan 28;21(1):83–91. Available from: http://link.springer.com/10.1007/s12603-015-0652-3

132. Jilka RL, Weinstein RS, Bellido T, Roberson P, Parfitt AM, Manolagas SC. Increased bone formation by prevention of osteoblast apoptosis with parathyroid hormone. J. Clin. Invest. [Internet]. 1999 Aug 15;104(4):439–46. Available from: http://www.jci.org/articles/view/6610

133. Institute for Clinical and Economic Review. Anabolic Therapies for Osteoporosis : Effectiveness and Value [Internet]. 2017. Available from: https://icer.org/wp-content/uploads/2020/10/CTAF_Osteoporosis_Evidence_Report_061617.pdf

134. Yamamoto T, Hasegawa T, Sasaki M, Hongo H, Tsuboi K, Shimizu T, Ota M, Haraguchi M, Takahata M, Oda K, Luiz de Freitas PH, Takakura A, Takao-Kawabata R, Isogai Y, Amizuka N. Frequency of Teriparatide Administration Affects the Histological Pattern of

Bone Formation in Young Adult Male Mice. Endocrinology. United States; 2016 Jul;157(7):2604–20.

135. Hansen S, Hauge EM, Beck Jensen J-E, Brixen K. Differing effects of PTH 1-34, PTH 1-84, and zoledronic acid on bone microarchitecture and estimated strength in postmenopausal women with osteoporosis: an 18-month open-labeled observational study using HR-pQCT. J. bone Miner. Res. Off. J. Am. Soc. Bone Miner. Res. United States; 2013 Apr;28(4):736–45.
136. Burr DB, Hirano T, Turner CH, Hotchkiss C, Brommage R, Hock JM. Intermittently Administered Human Parathyroid Hormone(1-34) Treatment Increases Intracortical Bone Turnover and Porosity Without Reducing Bone Strength in the Humerus of Ovariectomized Cynomolgus Monkeys. J. Bone Miner. Res. [Internet]. 2001 Jan 1;16(1):157–65. Available from: http://doi.wiley.com/10.1359/jbmr.2001.16.1.157
137. Sato M, Westmore M, Ma YL, Schmidt A, Zeng QQ, Glass E V, Vahle J, Brommage R, Jerome CP, Turner CH. Teriparatide [PTH(1-34)] strengthens the proximal femur of ovariectomized nonhuman primates despite increasing porosity. J. bone Miner. Res. Off. J. Am. Soc. Bone Miner. Res. United States; 2004 Apr;19(4):623–9.
138. Santangelo B, Micieli F, Mozzillo T, Reynaud F, Marino F, Auletta L, Vesce G. Transnasal administration of a combination of dexmedetomidine, midazolam and butorphanol produces deep sedation in New Zealand White rabbits. Vet. Anaesth. Analg. United States; 2016 Mar;43(2):209–14.
139. Woods RP. Validation of Registration Accuracy. Handb. Med. Imaging [Internet]. Elsevier; 2000. p. 491–7. Available from: https://linkinghub.elsevier.com/retrieve/pii/B9780120777907500369
140. Weinfurt KP. Repeated measures analysis: ANOVA, MANOVA, and HLM. Read. Underst. MORE Multivar. Stat. Washington, DC, US: American Psychological Association; 2000. p. 317–61.
141. Lotinun S, Sibonga JD, Turner RT. Differential effects of intermittent and continuous administration of parathyroid hormone on bone histomorphometry and gene expression. Endocrine [Internet]. 2002 Feb;17(1):29–36. Available from: http://www.ncbi.nlm.nih.gov/pubmed/12014700
142. Kim SW, Pajevic PD, Selig M, Barry KJ, Yang J-Y, Shin CS, Baek W-Y, Kim J-E,

Kronenberg HM. Intermittent parathyroid hormone administration converts quiescent lining cells to active osteoblasts. J. Bone Miner. Res. [Internet]. 2012 Oct;27(10):2075–84. Available from: http://www.ncbi.nlm.nih.gov/pubmed/22623172

143. Eriksen EF. Normal and pathological remodeling of human trabecular bone: three dimensional reconstruction of the remodeling sequence in normals and in metabolic bone disease. Endocr. Rev. [Internet]. 1986 Nov;7(4):379–408. Available from: http://www.ncbi.nlm.nih.gov/pubmed/3536460
144. Martin RB. On the significance of remodeling space and activation rate changes in bone remodeling. Bone [Internet]. 1991 Jan;12(6):391–400. Available from: https://linkinghub.elsevier.com/retrieve/pii/875632829190028H
145. Heřt J, Fiala P, Petrtýl M. Osteon orientation of the diaphysis of the long bones in man. Bone [Internet]. 1994 May;15(3):269–77. Available from: https://linkinghub.elsevier.com/retrieve/pii/8756328294902887
146. Petrtýl M, Heřt J, Fiala P. Spatial organization of the haversian bone in man. J. Biomech. [Internet]. 1996 Feb;29(2):161–9. Available from: https://linkinghub.elsevier.com/retrieve/pii/0021929094000352
147. Young DR, Niklowitz WJ, Brown RJ, Jee WSS. Immobilization-associated osteoporosis in primates. Bone [Internet]. 1986 Jan;7(2):109–17. Available from: https://linkinghub.elsevier.com/retrieve/pii/8756328286906824
148. van Oers RFM, Ruimerman R, Tanck E, Hilbers PAJ, Huiskes R. A unified theory for osteonal and hemi-osteonal remodeling. Bone [Internet]. 2008 Feb;42(2):250–9. Available from: https://linkinghub.elsevier.com/retrieve/pii/S8756328207007740
149. Martínez-Reina J, García-Aznar JM, Domínguez J, Doblaré M. A bone remodelling model including the directional activity of BMUs. Biomech. Model. Mechanobiol. [Internet]. 2009 Apr 15;8(2):111–27. Available from: http://link.springer.com/10.1007/s10237-008-0122-5
150. Martínez-Reina J, Reina I, Domínguez J, García-Aznar JM. A bone remodelling model including the effect of damage on the steering of BMUs. J. Mech. Behav. Biomed. Mater. [Internet]. 2014 Apr;32:99–112. Available from: https://linkinghub.elsevier.com/retrieve/pii/S1751616113004451
151. Hildebrand T, Ruegsegger P. Quantification of Bone Microarchitecture with the Structure

Model Index. Comput. Methods Biomech. Biomed. Engin. [Internet]. 1997 Jan;1(1):15–23. Available from: http://www.tandfonline.com/doi/abs/10.1080/01495739708936692

152. Bilezikian JP. Combination anabolic and antiresorptive therapy for osteoporosis: opening the anabolic window. Curr. Osteoporos. Rep. [Internet]. 2008 Mar;6(1):24–30. Available from: http://www.ncbi.nlm.nih.gov/pubmed/18430397

153. Rubin MR, Bilezikian JP. The anabolic effects of parathyroid hormone therapy. Clin. Geriatr. Med. [Internet]. 2003 May;19(2):415–32. Available from: http://www.ncbi.nlm.nih.gov/pubmed/12916294

154. Paganin D, Mayo SC, Gureyev TE, Miller PR, Wilkins SW. Simultaneous phase and amplitude extraction from a single defocused image of a homogeneous object. J. Microsc. [Internet]. 2002 Apr;206(1):33–40. Available from: http://doi.wiley.com/10.1046/j.1365-2818.2002.01010.x

APPENDIX A

This appendix presents the methodology used to measure the *in vivo* radiation dose applied to the rabbits during the experiments in the BMIT-BM 05B1-1 beamline at the Canadian Light Source.

A.1. *In vivo* radiation dose measurements

The radiation dose applied to rabbits during the *in vivo* images was measured using a PinPoint ion chamber (model 31014, PTW, Germany) and Thermoluminescent dosimeter (TLD) chips (Mirion Technologies, Ontario, Canada). Before starting the *in vivo* imaging acquisition, the ion chamber was positioned in the middle of the beam (position#1 - distance from the source to the ion chamber = 51 m) behind the slits (Figure A1.a) and then inside the Lucite tube used as the rabbit leg holder (position#2 - distance from the source to the sample = 58.8 m, Figure A1.b). The dose rate was estimated as 79.9 mGy/s (current:163 mA) at position#1 and 42.2 mGy/s (current: 160mA) at position#2. The ion chamber was used during the experiment to estimate each rabbit's dose rate and keep the desired radiation dose at 2 Gy using 1000 projections.

A total of eight TLD chips (TLD chip size = 3.15 x 3.15 mm) were scanned using the same parameters as the *in vivo* images to confirm the radiation dose applied to the rabbits. The chips were wrapped and taped using Kapton film. We positioned one chip (6ARE-A) in the same position as the ion chamber (position#1, Figure A2.a, one scan), and three chips (5ARE-A, B and C, three subsequent scans) were taped outside the Lucite tube (position#2, Figure A2.b). Using a rabbit carcass (the right tibia was dissected from a previous experiment), we wrapped four chips (4 AREA-A, B, C and D) on the right leg to position the rabbit leg inside of the Lucite tube (Figures A3. a and b). Three sequential scans were performed to map the radiation dose applied to the rabbit leg. Table A1 summarizes each TLD chip radiation dose with corresponding ion chamber readings.

a

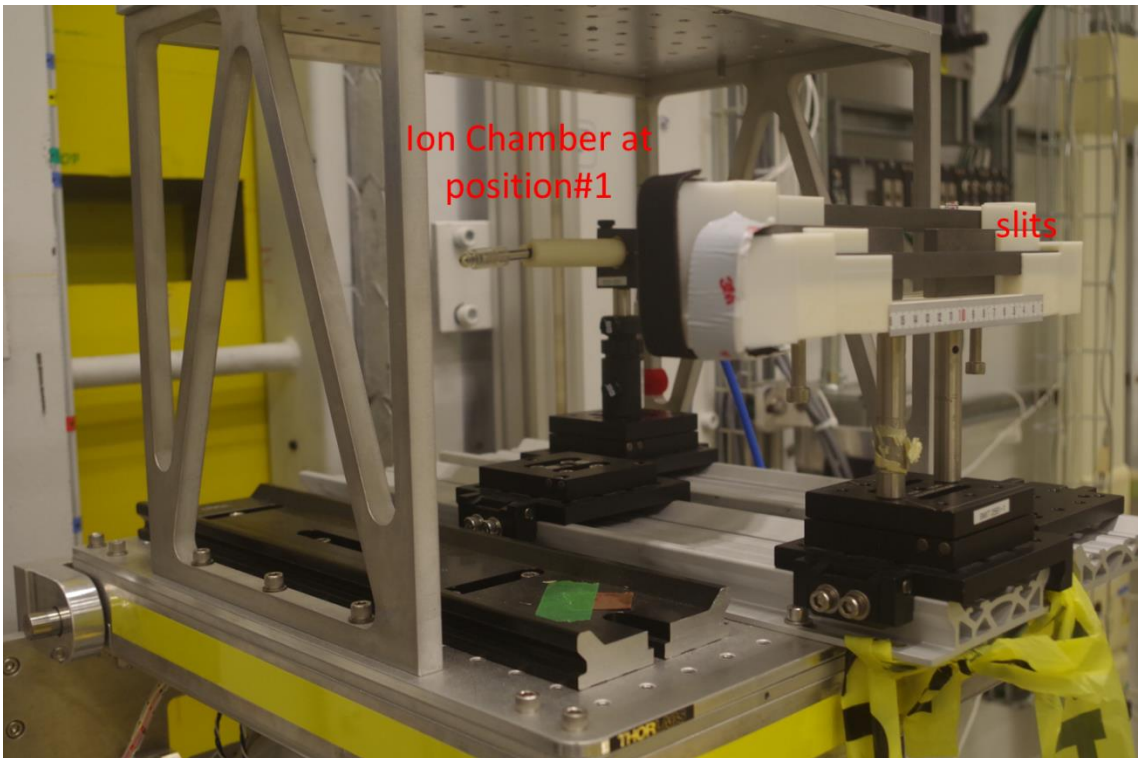

b

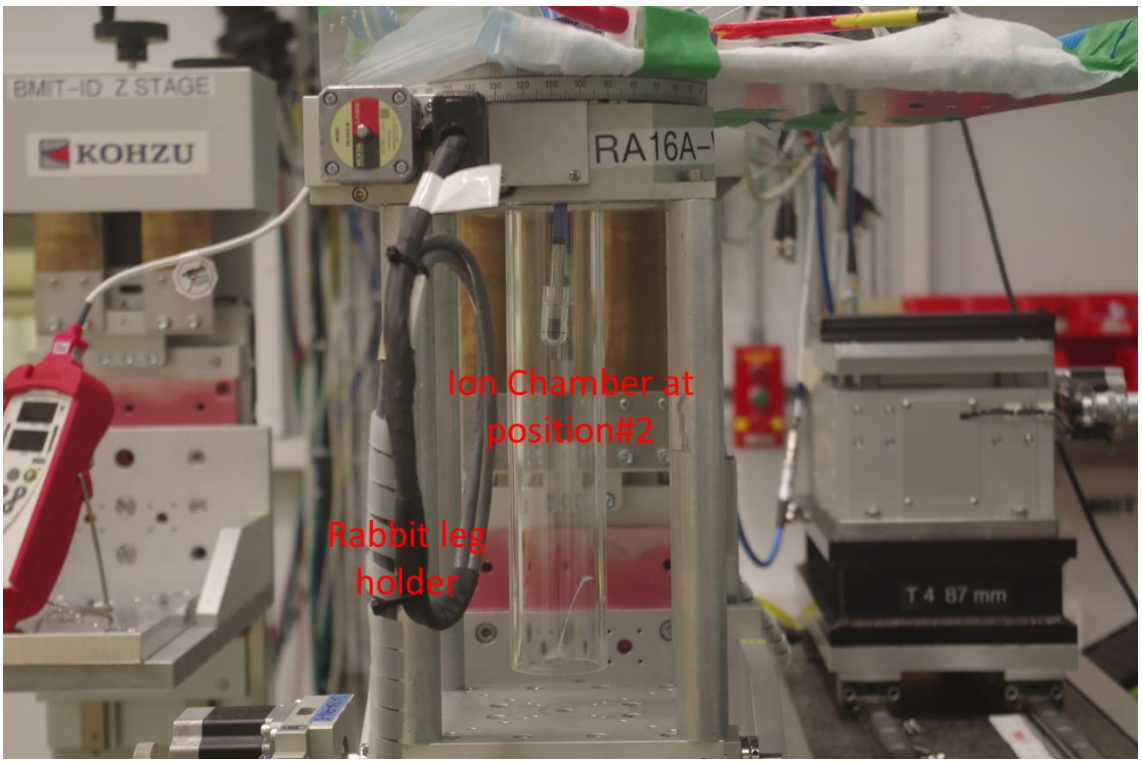

Figure A. 1. The PinPoint ion chamber (a) at position#1 and (b) at position#2.

a

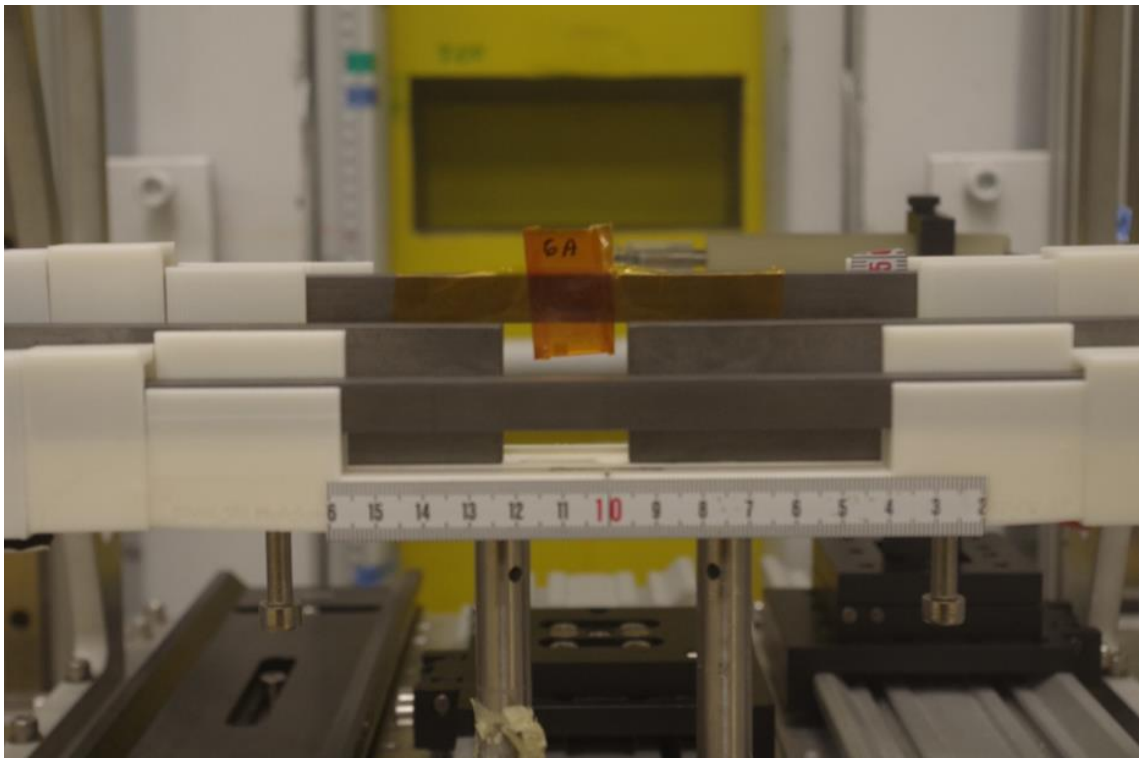

b

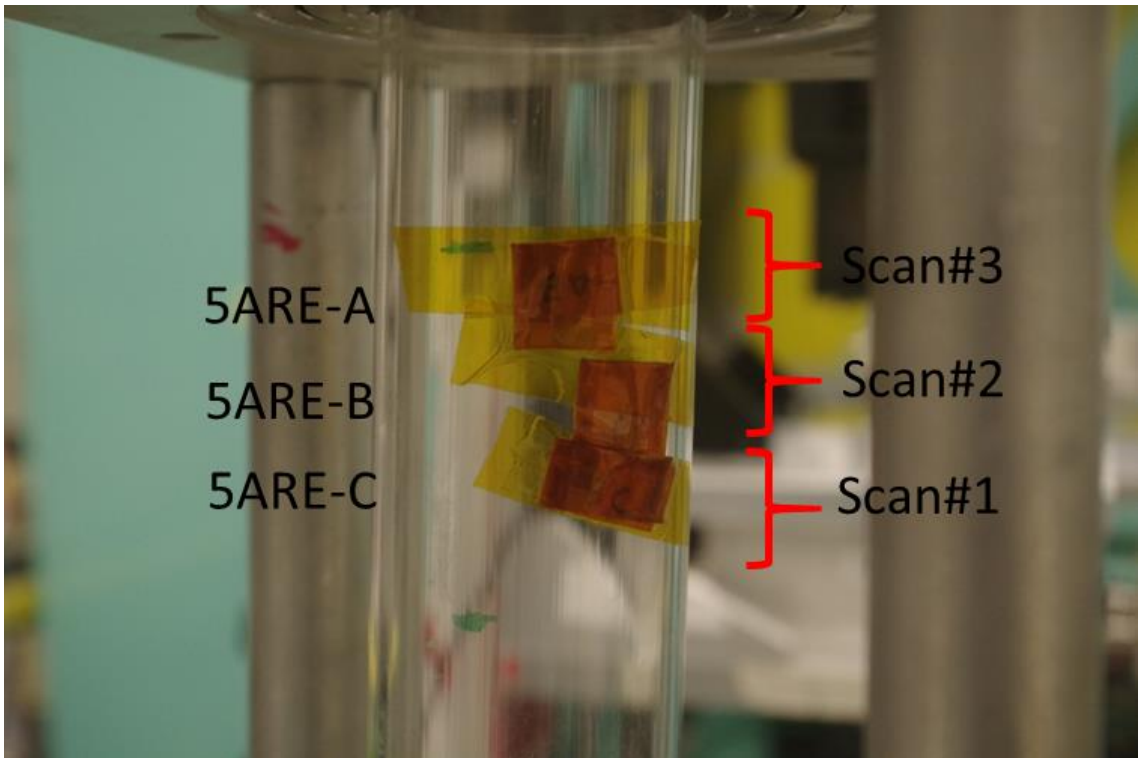

Figure A. 2. TLD chips wrapped in Kapton film. (a) at position#1 and (b) at position#2, showing the region of the three subsequent scans.

a

b

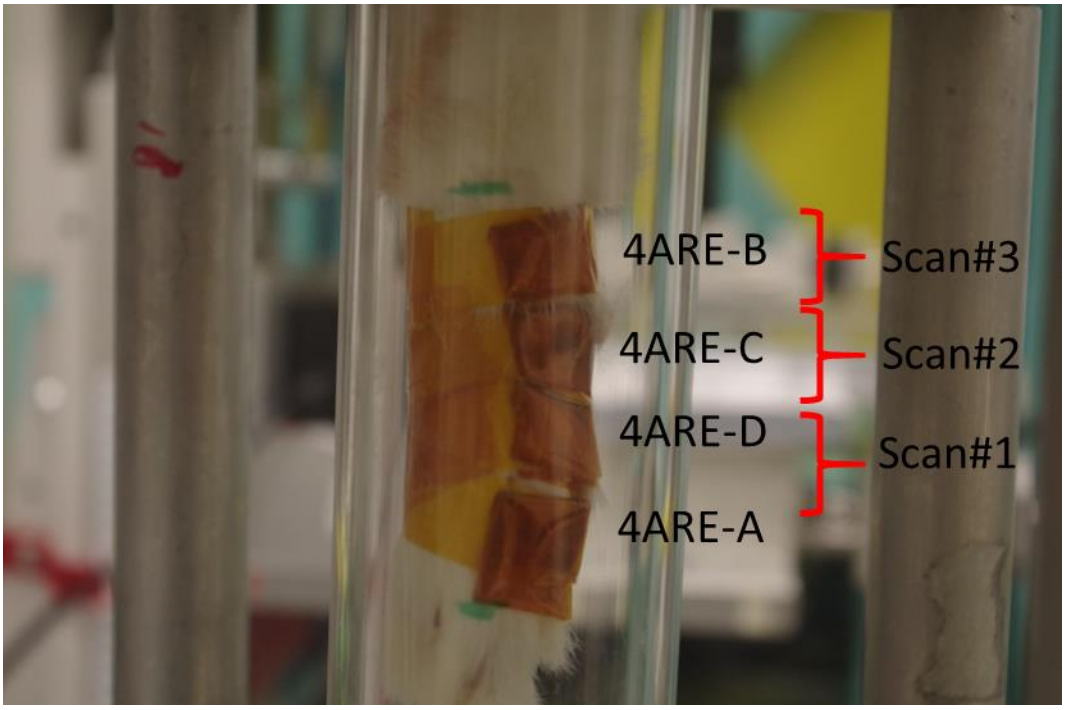

Figure A. 3. (a) TLD chips wrapped in the rabbit carcass. (b) The rabbit leg inside the Lucite tube shows the region of the three subsequent scans.

Table A. 1. in vivo and ex vivo data sets threshold ranges

TLD Chip ID #	Radiation Dose Estimation using TLD Chips and Ion Chamber		
	TLD (Gy)	**TLD Description**	**Ion Chamber (Gy)**
6ARE-A	2.22	TLD in the same position as the ion chamber (position #1).	2.11
5ARE-A	1.85	Without the rabbit leg and outside of the tube. TLD was positioned in the image of Scan#3.	2.11
5ARE-B	1.13	Without the rabbit leg and outside of the tube. TLD was positioned in the image of Scan#2. The chip went out of the field of view during scan.	2.16
5ARE-C	1.34	Without the rabbit leg and outside of the tube. TLD was positioned in the image of Scan#1. The chip went out of the field of view during scan.	2.20
4ARE-B	3.33	With the rabbit leg inside of the tube. TLD was positioned in the image of Scan#3.	2.13
4ARE-C	2.87	With the rabbit leg inside of the tube. TLD was positioned in the image of Scan#2.	2.15
4ARE-D	1.93	With the rabbit leg inside of the tube. TLD was positioned in the image of Scan#1.	2.16
4ARE-A	0.06	With the rabbit leg inside of the tube. Half of the TLD was positioned in bottom of the image of Scan#1. The chip went out of the field of view during scan.	2.16

APPENDIX B

This appendix presents the settings used for image reconstruction for the *in vivo* data sets using the UFO-KIT software package (https://ufo.kit.edu/dis) and the *ex vivo* data sets using the NRecon software package (Bruker).

B.1. *In vivo* data sets reconstruction

EZ-UFO is a graphical user interface to the UFO-KIT software package (Figure B1) used for the reconstruction of synchrotron-based X-ray micro-CT data available at the Biomedical Image and Therapy Facility (BMIT) at the Canadian Light Source (CLS). EZ-UFO reconstructs the images using the Filtered Back Projection (FBP) algorithm. In the main tab (Figure B1), you can set parameters for the center of rotation, phase retrieval, filters, region of interest and histogram settings, and configuration before you click on reconstruct. In the new software version, it is also possible to set advanced parameters for reconstruction, stitch images, and view them. The first version of the software used in this thesis only consisted of the main tab. Below, I am describing the step-by-step used for the *in vivo* data sets reconstruction.

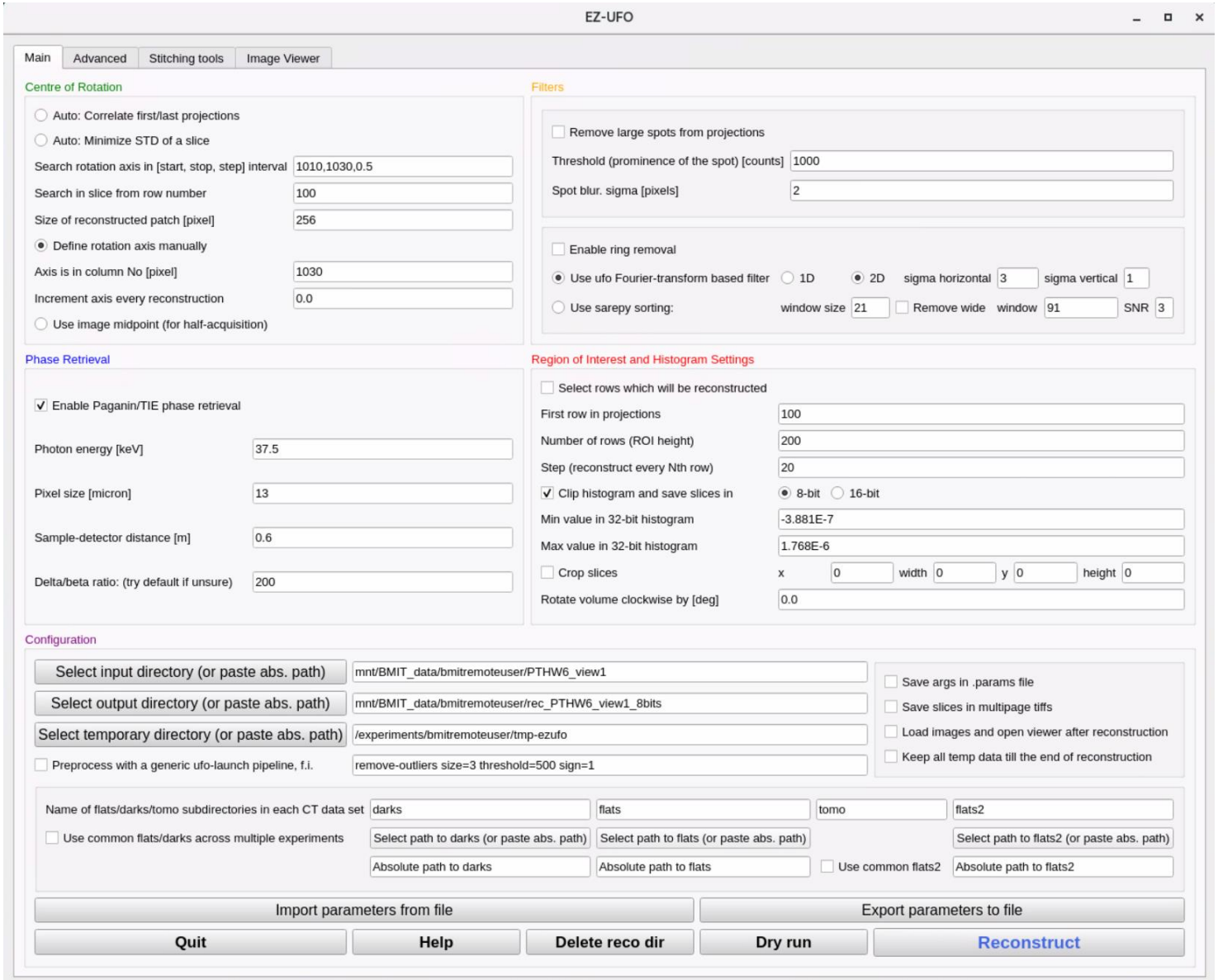

Figure B. 1. Ez-UFO main interface.

Once the EZ-UFO was launched, the first step was to select the input and output directories for the images and the names of the darks, flats and tomo from each data in the Configuration section (Figure B1). After that, enable Phaganin/TIE phase retrieval was selected using the parameters taken from the *in vivo* image (photon energy = 37.5 keV, pixel size = 13 μm and sample-detector distance = 60 cm) and the default value of 200 for the delta/beta ration. The Paganin phase retrieval method[154] converts the image signal into enhanced image contrast between materials. In other words, it enhanced the image contrast between bone and soft tissue in the *in vivo* data sets. The next step was to set the center of the rotation axis. During the image acquisition the center of rotation axis varied between 1029 to 1031. The rotation axis was set at 1030 pixel. In the first version of the software, it was possible to use a sinogram filtration in the frequency domain filter with kernel sizes of 1, 2 and 3. This filter uses convolution to suppress variations in the mean intensity of sinogram rows. As the *in vivo* images did not present significant ring artifacts, a convolution kernel of size =1 was used on the reconstruction. By default, EZ-UFO reconstructs the images in 32-bit format. However, the user can clip the image histogram to 16 or 8-bit format (Region of interest and Histogram settings section in Figure B1). To apply this step is necessary to choose the best range values for the histogram to be clipped. A preview reconstruction was applied to each *in vivo* data set using the Select rows which will be reconstructed (First row in projections = 100, Number of rows = 200, and Step = 20, Region of interest and Histogram settings section in Figure B1). After this step, each short reconstruction was opened in the ImageJ software (https://imagej.nih.gov/ij/) to record their histogram range values. Table B1 presents each 32-bit histogram range of the *in vivo* data sets. The best histogram range was chosen using the minimum and maximum values of table B1 (-3.881E-7 – 1.768E-6). It was applied to Clip histogram and save slice in the Region of interest and Histogram settings section (Figure B1) to convert the images into the 8-bit format. Figure B2 shows an image dataset histogram before and after clipping. All the *in vivo* data sets were then reconstructed using the button Reconstruct in the Configuration section.

Table B. 1. In vivo and ex vivo data sets threshold ranges

Rabbits	32-bit Histogram Ranges	
	***in vivo* View# 1**	in vivo **View# 2**
PTHW1	-3.321E-7 – 1.478E-6	-3.073E-7 – 1.492E-6
PTHW2	-2.772E-7 – 1.370E-6	-2.791E-7 – 1.412E-6
PTHW3	-3.881E-7 – 1.483E-6	-2.946E-7 – 1.340E-6
PTHW4	-3.229E-7 – 1.473E-6	-2.973E-7 – 1.342E-6
PTHW5	-3.336E-7 – 1.435E-6	-2.773E-7 – 1.311E-6
PTHW6	-3.637E-7 – 1.768E-6	-3.239E-7 – 1.731E-6
PTHW7	-2.986E-7 – 1.350E-6	-3.124E-7 – 1.421E-6
PTH1	-3.022E-7 – 1.281E-6	-3.107E-7 – 1.328E-6
PTH2	-2.925E-7 – 1.263E-6	-3.120E-7 – 1.587E-6
PTH3	-2.915E-7 – 1.290E-6	-3.267E-7 – 1.423E-6
PTH4	-3.776E-7 – 1.424E-6	-3.769E-7 – 1.396E-6
PTH5	-3.804E-7 – 1.283E-6	-3.238E-7 – 1.251E-6
PTH6	-2.756E-7 – 1.358E-6	-2.985E-7 – 1.337E-6
PTH7	-3.809E-7 – 1.265E-6	-2.985E-7 – 1.469E-6

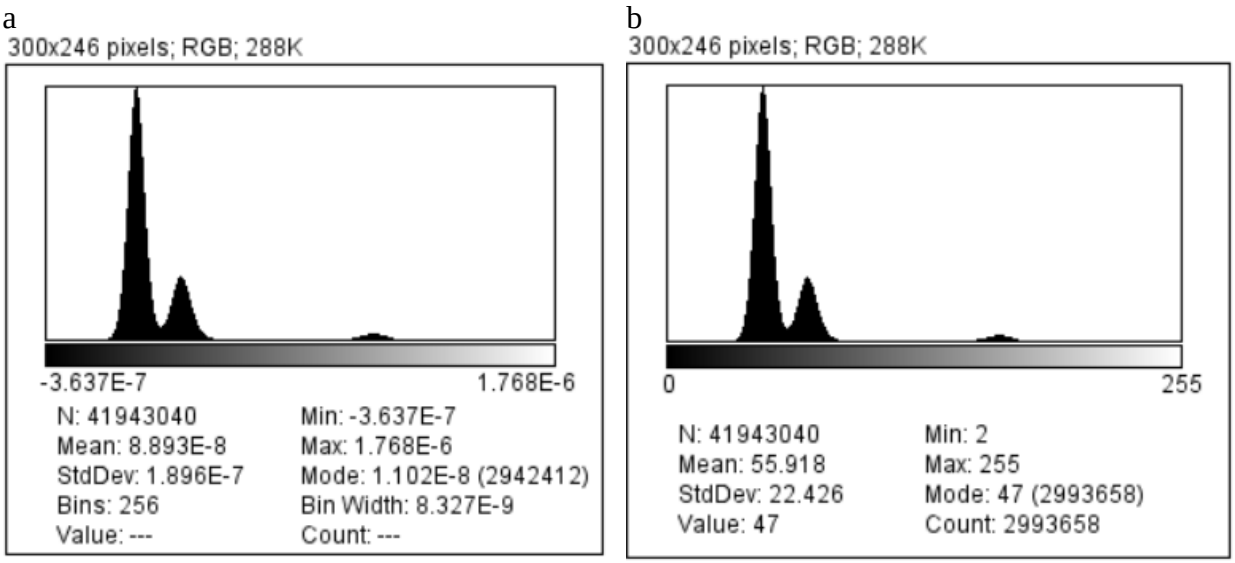

Figure B. 2. (a) 32-bit histogram of PTHW6 in vivo View#1. (b) 8-bit histogram of PTHW6 in vivo View#1 after clipping.

B.2.*Ex vivo* data sets reconstruction

The ex vivo data sets from the right and left tibia were reconstructed using the NRecon software package (Bruker). The NRecon reconstructs the images using the Filtered Back Projection (FBP) algorithm. Once NRecon is started and a data set is loaded (Figure B3), it is possible to see a scout scan image with two dark-red lines indicating the slice range for volume reconstruction, and a green line indicating the slice to be reconstructed in the preview mode. The first step is to do a preview reconstruction of a slice of your data set by clicking on the Preview button on the Start tab (Reconstruction section Figure B3). Once the preview reconstruction is done, the Output tab (Reconstruction section Figure B4) automatically pops up showing an image slice. In this tab, you can see the image histogram with the minimum and maximum values of the attenuation coefficients, and you can also modify a few output parameters, such as the histogram range, image format, scales, ROI, etc. The first step in our methodology was to record the histogram range values of each *ex vivo* data set (Table B2). The best histogram range for reconstruction was chosen using the minimum and maximum values of table B2 (-0.008 – 0.08), and we set the images out put as 8-bit format.

There are another two tabs for reconstruction parameters in the NRecon. The Settings and Advanced tabs. The Settings tab shows the aligned mode. In this tab, we have selected

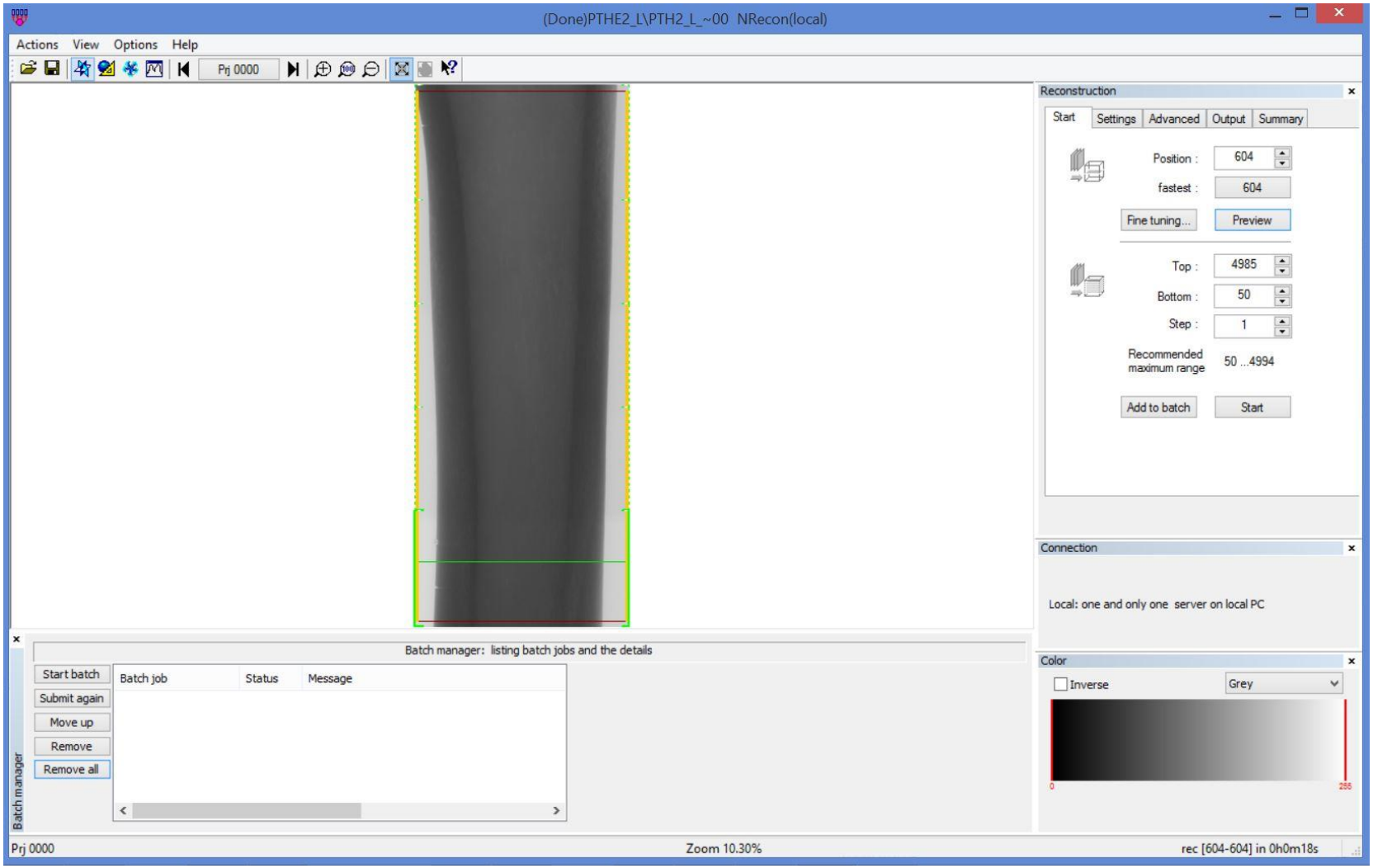

Figure B. 3. NRecon main interface shows the Start tab.

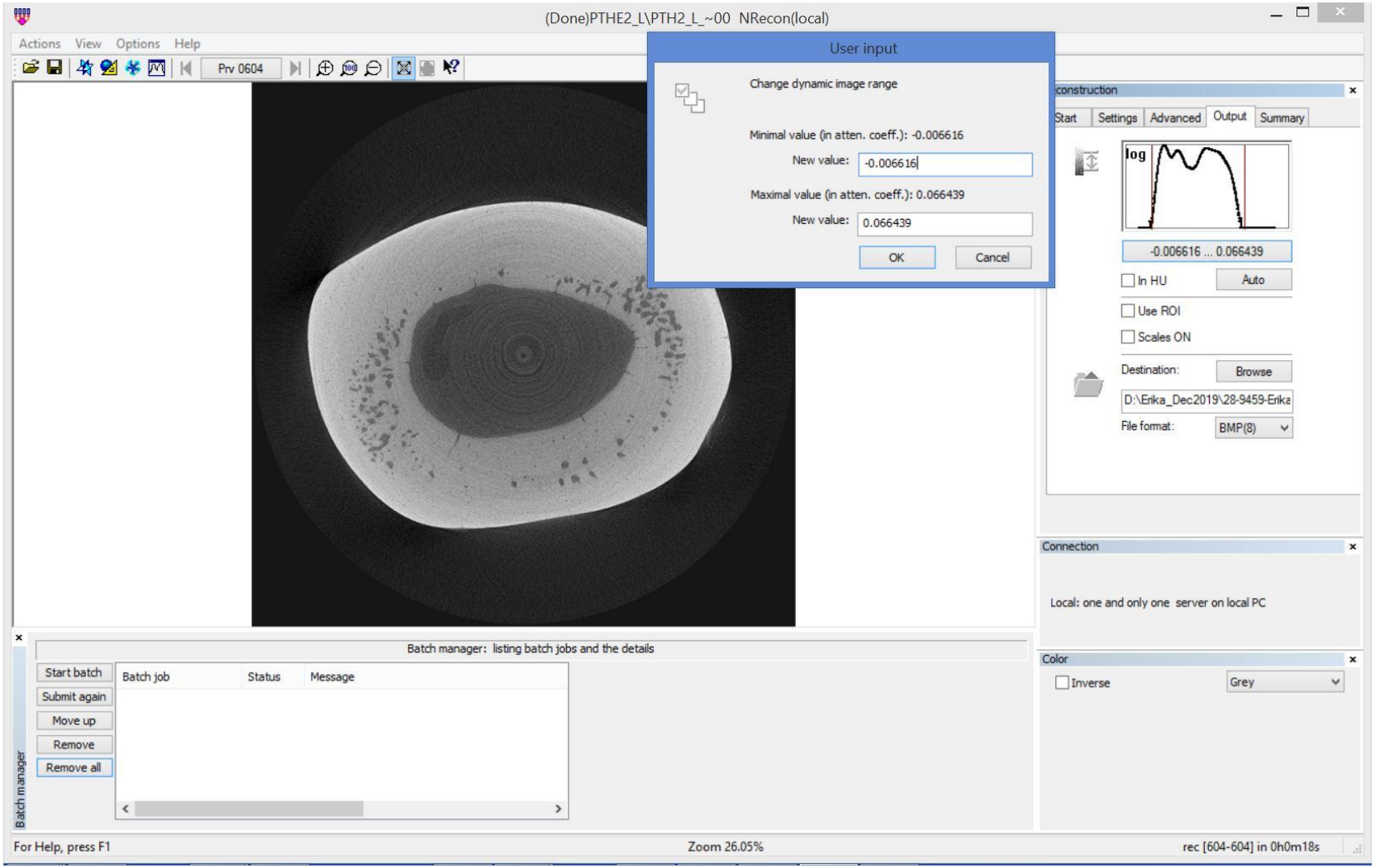

Figure B. 4. NRecon main interface shows the Output tab.

Table B. 2. The attenuation coefficient histogram range of the right and left tibia

Rabbits	Attenuation Coefficient Histogram Range	
	Right Tibia	**Left Tibia**
PTHW1	-0.008-0.06	-0.008-0.07
PTHW2	-0.007-0.07	-0.007-0.06
PTHW3	-0.008-0.07	-0.008-0.06
PTHW4	-0.006-0.08	-0.006-0.08
PTHW5	-0.008-0.07	-0.008-0.07
PTHW6	-0.008-0.07	-0.008-0.07
PTHW7	-0.008-0.07	-0.008-0.07
PTH1	-0.008-0.07	-0.008-0.07
PTH2	-0.007-0.07	-0.006-0.07
PTH3	-0.008-0.07	-0.008-0.08
PTH4	-0.008-0.06	-0.008-0.07
PTH5	-0.008-0.07	-0.008-0.07
PTH6	-0.007-0.07	-0.007-0.08
PTH7	-0.008-0.07	-0.008-0.07

to Show Misalignment compensation with a value of 4. We have also selected Object larger than the field of view, and Ring artifact reduction with a value of 1. In the Advancement tab, you can set the parameters for Smoothing filter with different kernels. This filter removes noise, but it may introduce blurring to your image. We have not used the Smoothing filter in our reconstruction. Once all the parameters were set, we used the Start tab clicking on the Start button to do the reconstruction of the whole data set.

APPENDIX C

This appendix presents the methodology developed for the 3D image registration and longitudinal erosion rate (LER) quantification used in my thesis. It is divided into data segmentation, 3D data registration, and LER quantification, as shown below.

C.1. Data Segmentation

In this section, I describe how data sets were imported, resized by a factor of 2, and segmented using the Amira software (version 6.2).

1. Open Amira software and click on open data to import your files (Figure C1.a). If your data set is too big, you will receive a message about out-of-core data. In the loading policy tab, choose to read complete volume into memory and click ok (Figure C1.b).
2. Next, set your images' voxel size and click ok (Figure C2.a). In this thesis, the voxel size of *in vivo* data sets was 13.05 µm, and ex vivo data sets was 4.93 µm. Data set will be visible in the project view, as you can see in Figure C2.b. You can rename it if you want.

a

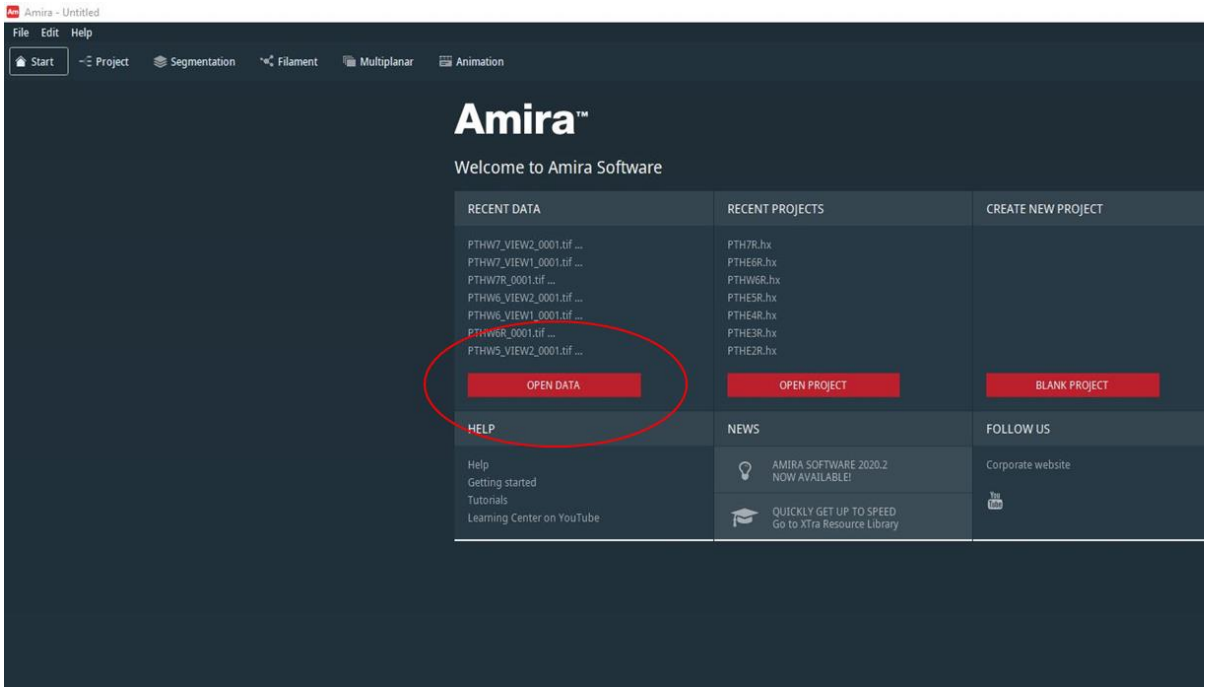

b

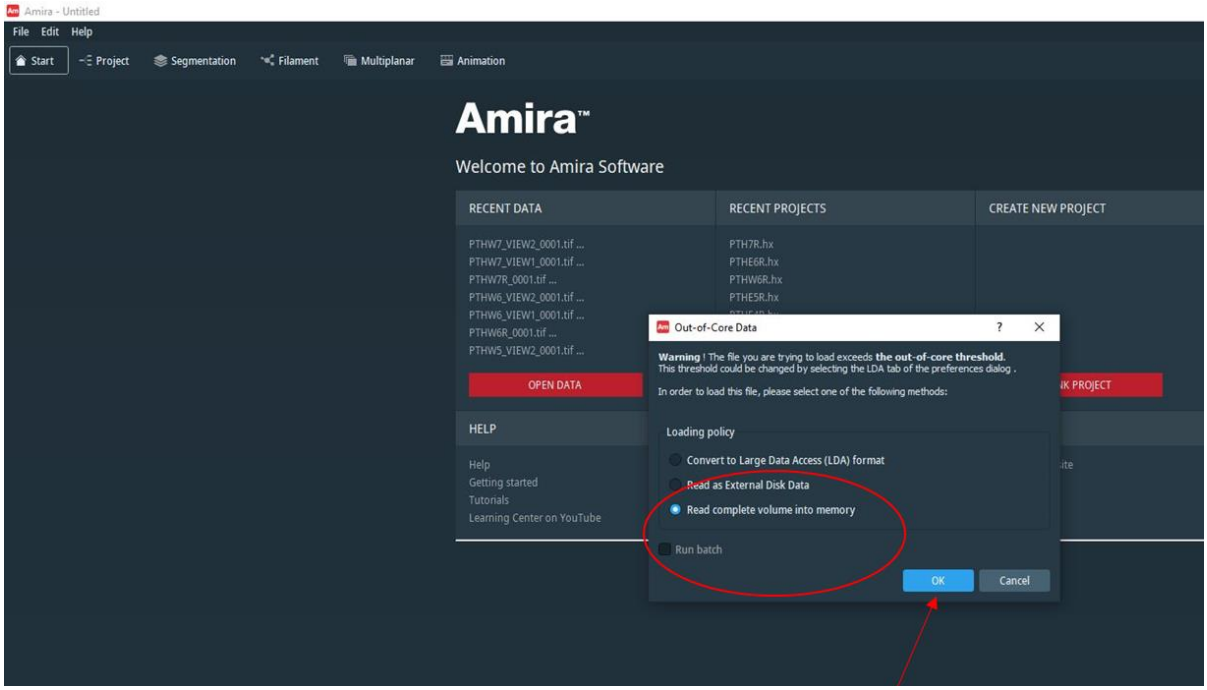

Figure C. 1. Importing a data set in Amira: (a) click on open data and (b) read complete volume into memory.

a

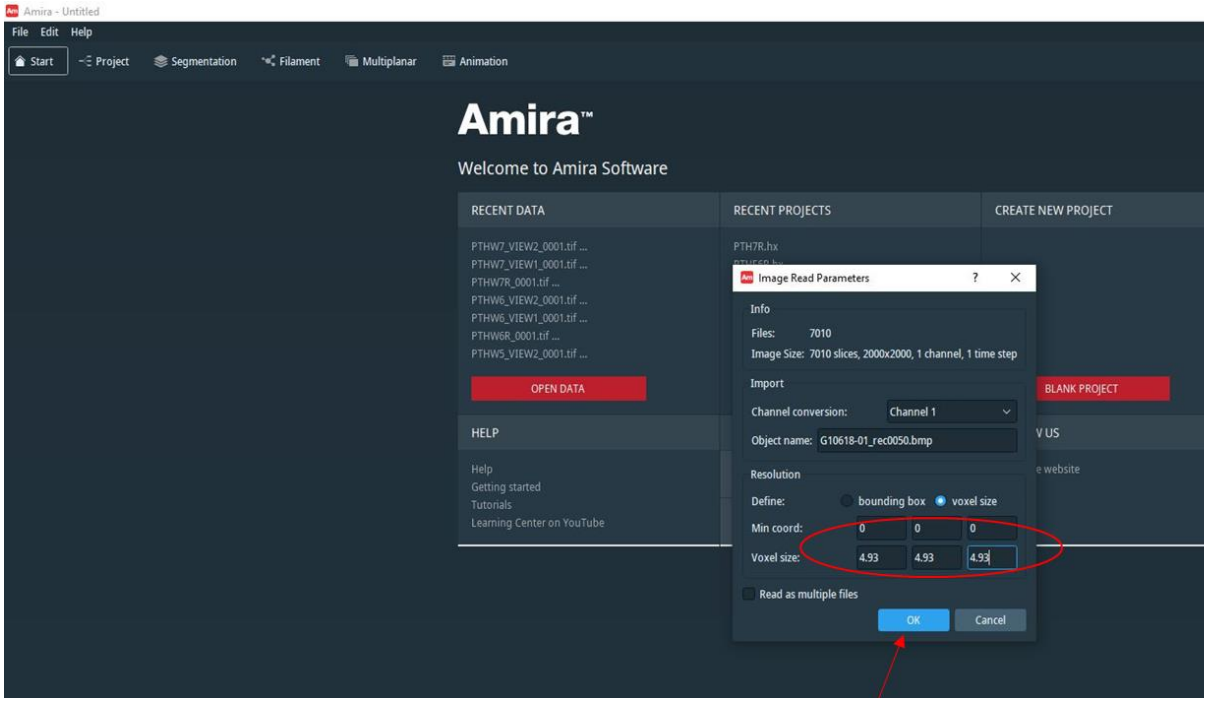

b

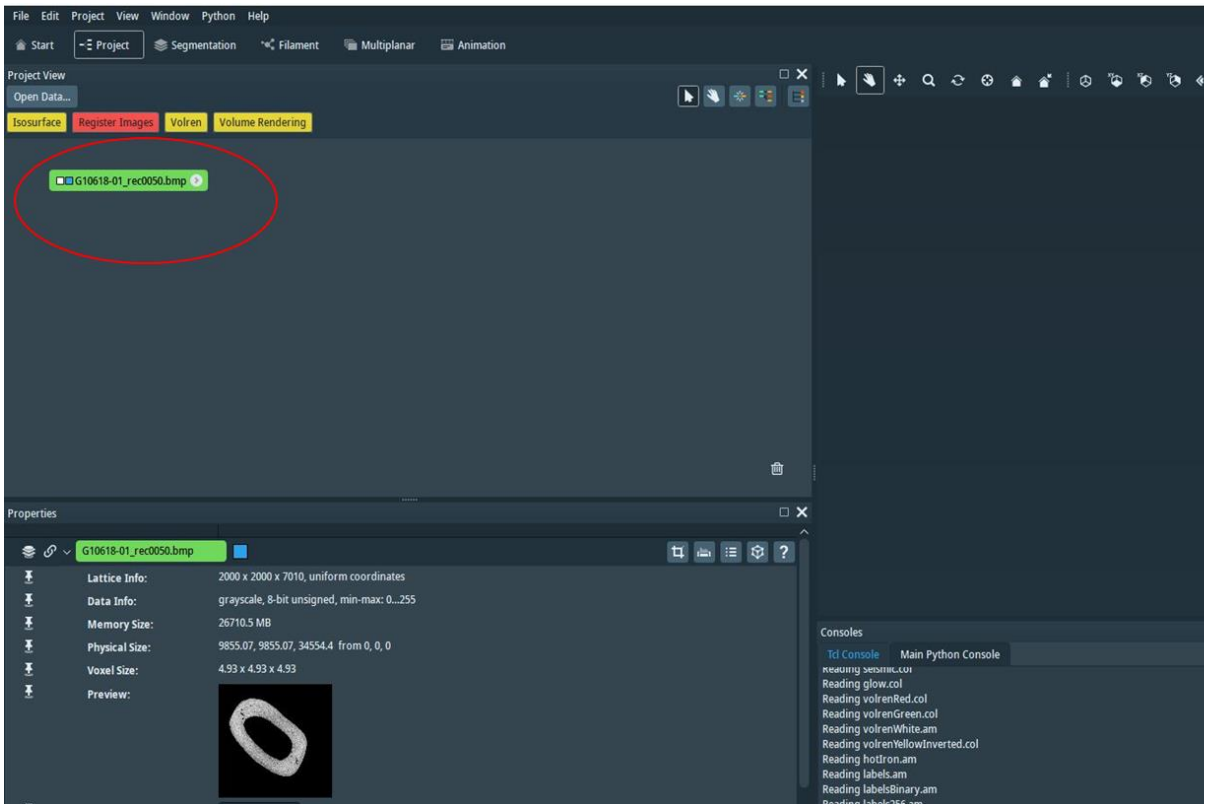

Figure C. 2. (a) Set a data set voxel size. (b) View data set in the project view area.

3. As the *ex vivo* data sets were big, I had to reduce their size by a factor of 2 to save computational memory. Click on data set (Figure C3), then choose compute > volume operations > resample > create.

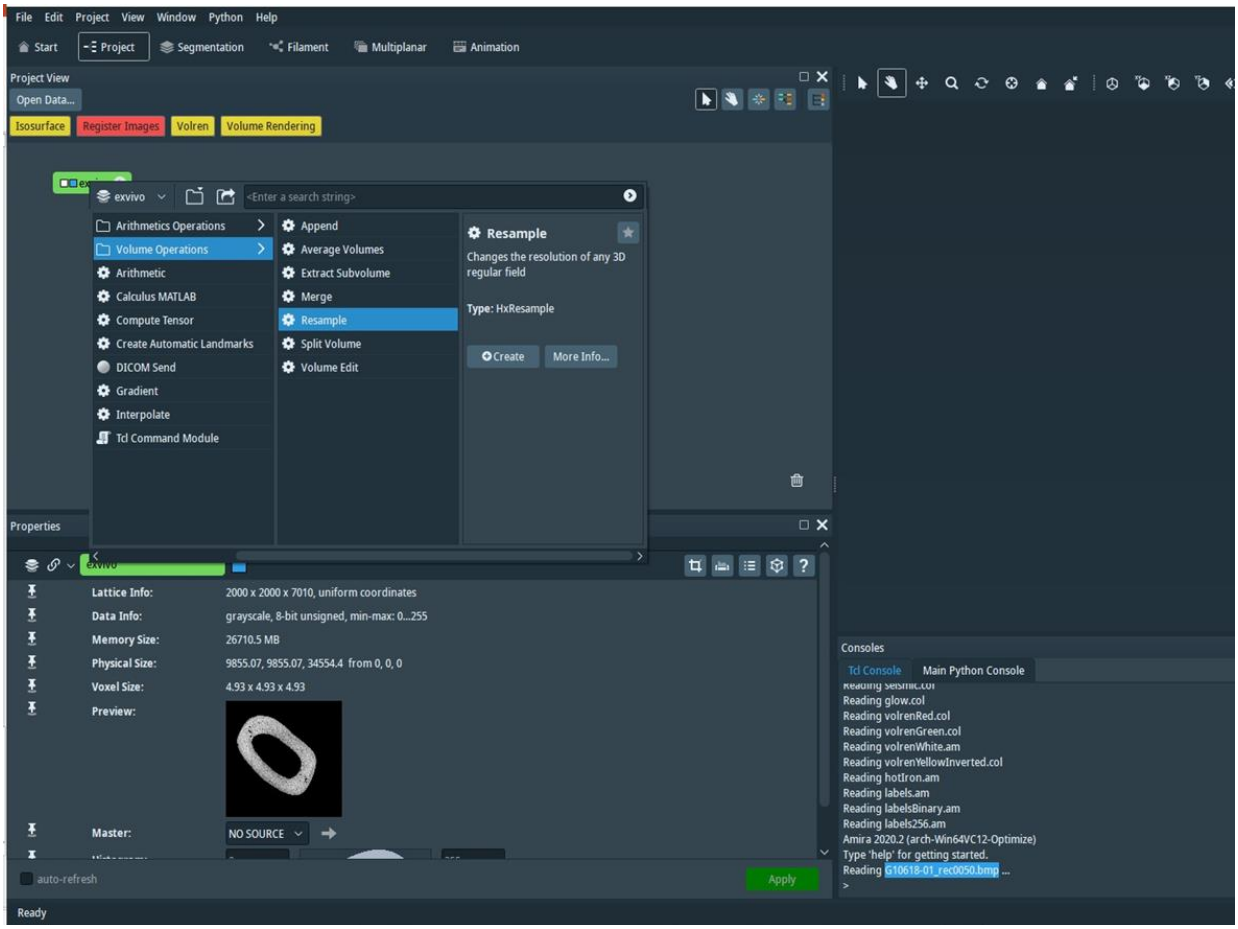

Figure C. 3. Resizing a data set in Amira: use volume operations > resample > create.

4. Once you have created the resample module, you must change the voxel size on the properties panel, and then click the apply button (Figure C4).

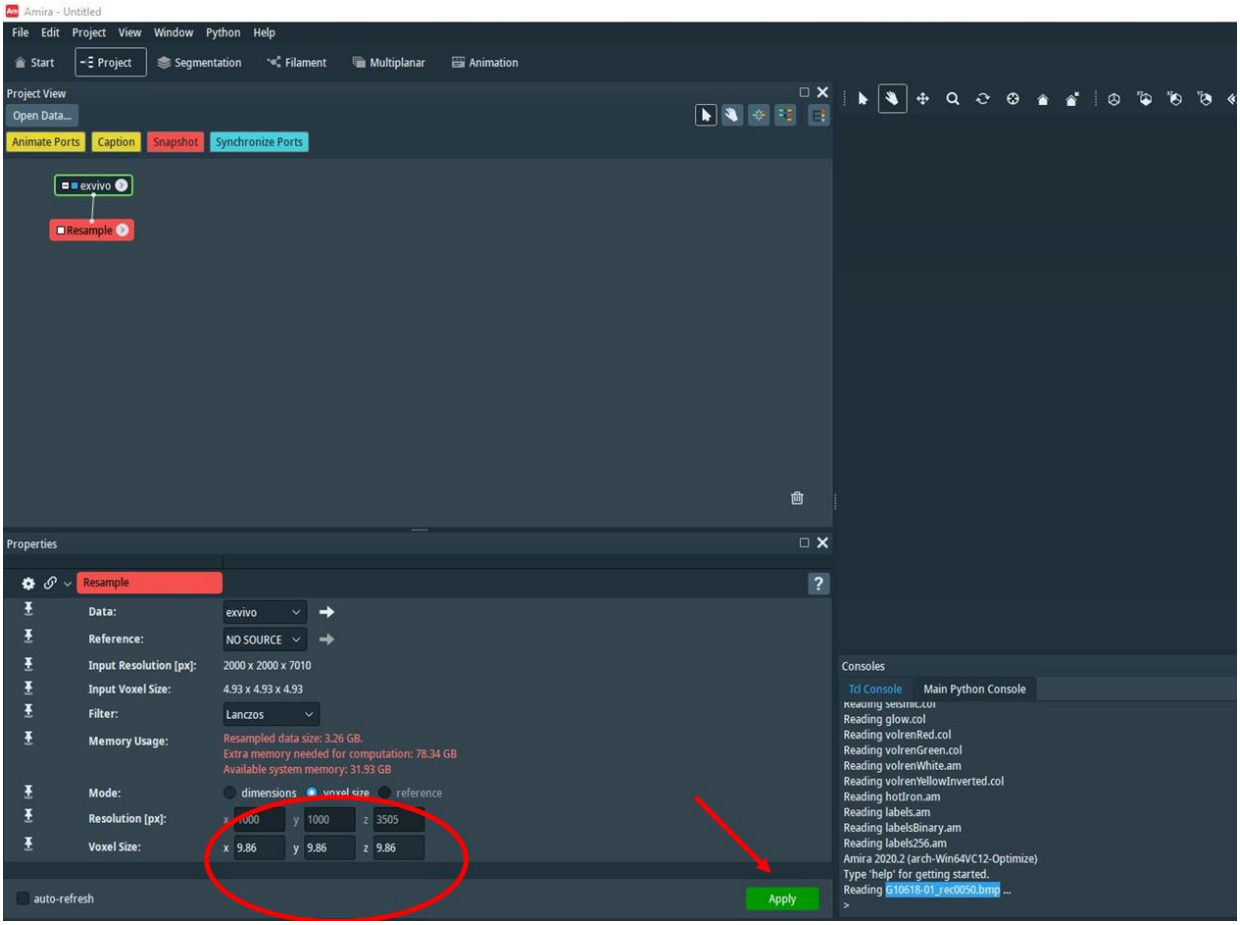

Figure C. 4. Setting the voxel size in the properties area.

5. You have created your resampled data set (Figure C5.a). Now you can click on the segmentation tab (Figure C5.b).

a

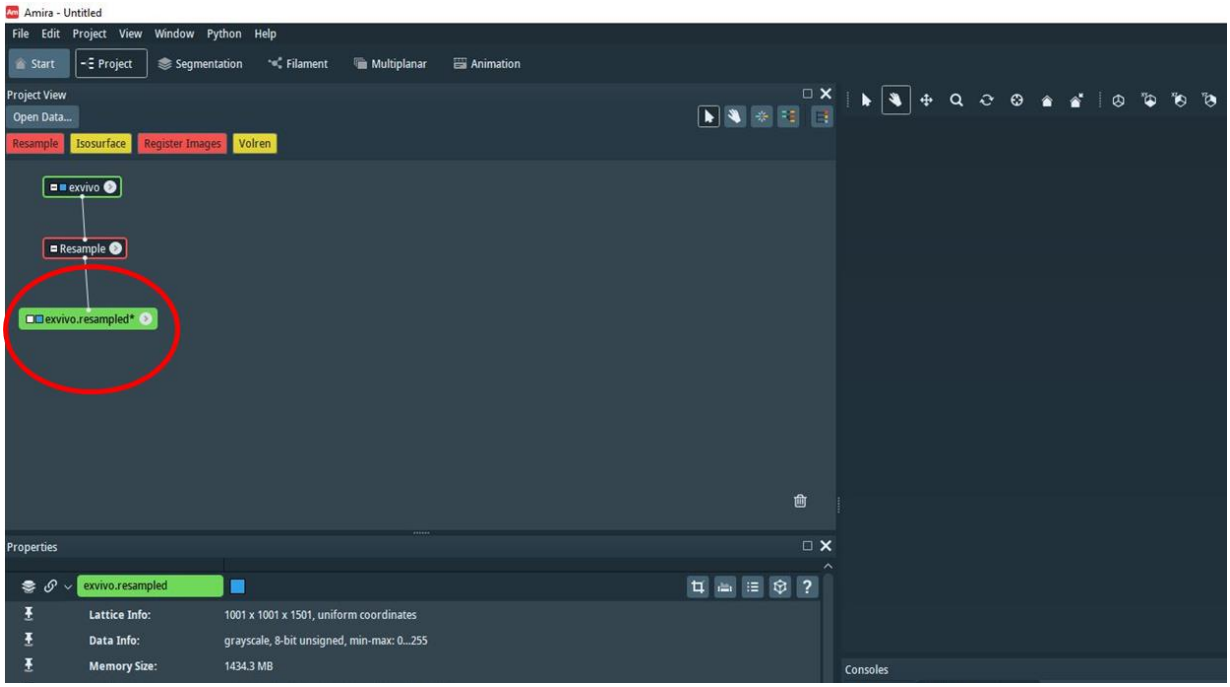

b

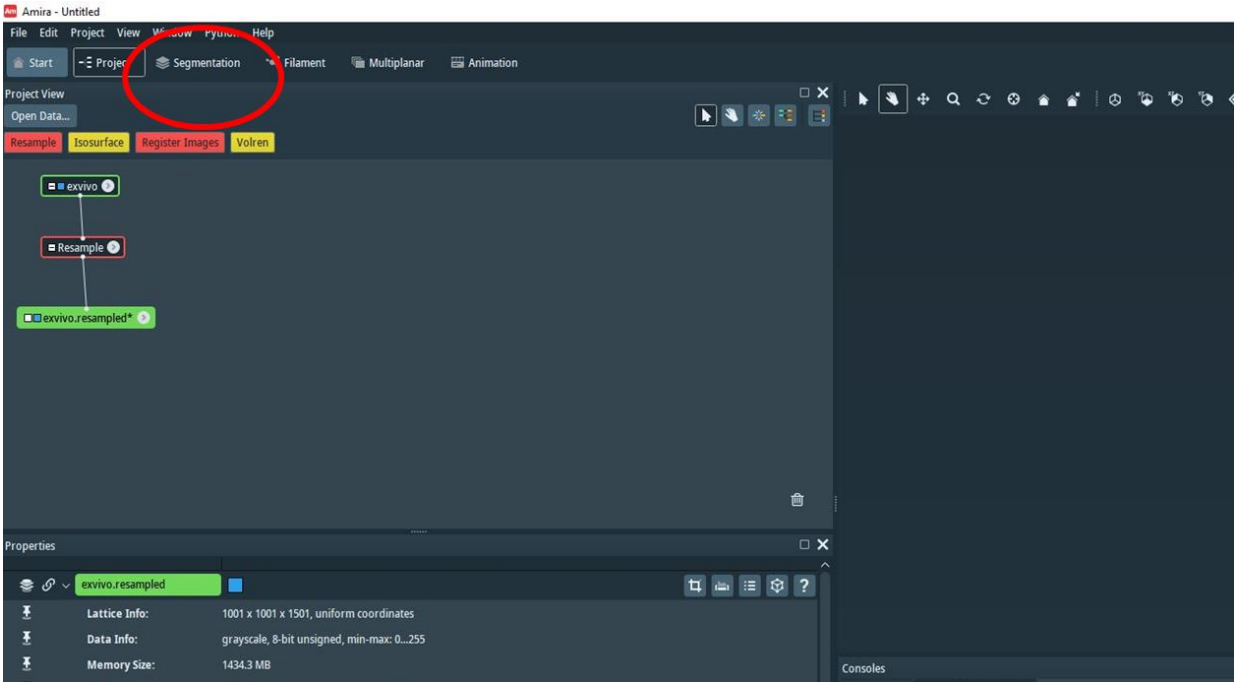

Figure C. 5. (a) Data set resampled. (b) The segmentation tab.

6. Once you have imported your data set into the project view, click on the segmentation tab. In the segmentation area, be sure you have selected the image you need to segment and look at the segmentation editor (red circle). In the same segmentation editor, you can see the image label that was created automatically (Figure C6).

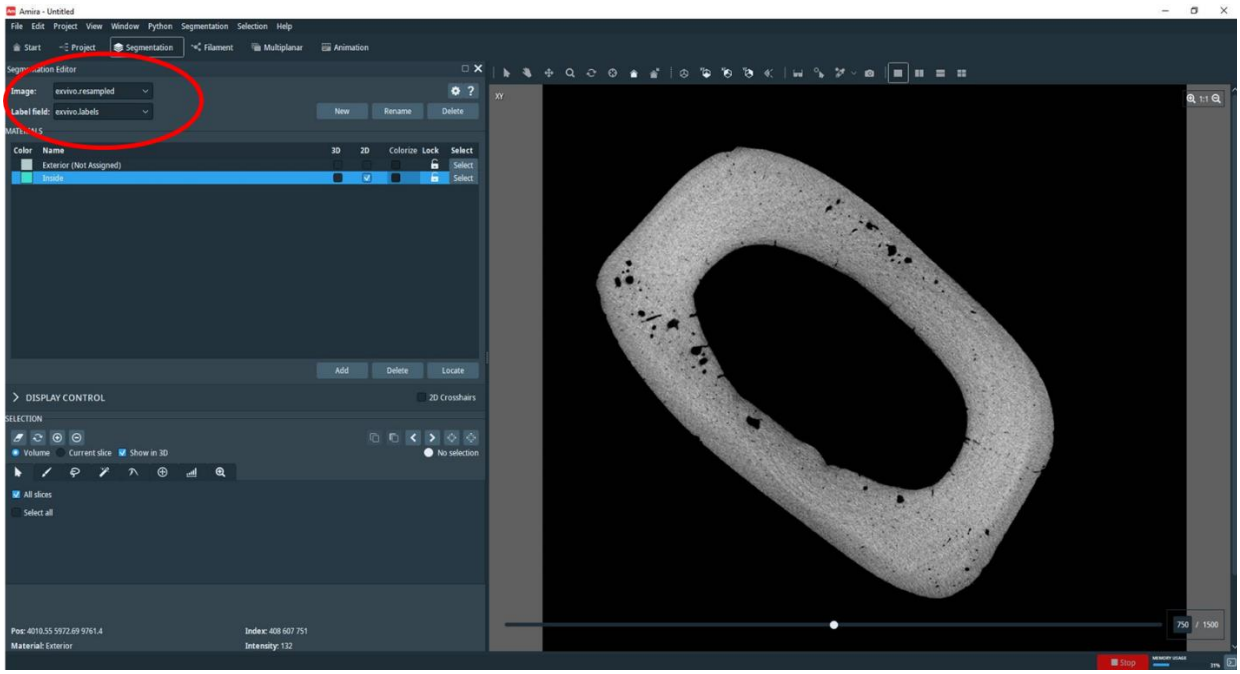

Figure C. 6. Segmentation tab in Amira. Red circle shows the image name and label field.

7. In the materials area, you will see the exterior and inside. Make sure the inside material (green box) is selected (Figure C7.a). To start the data segmentation, click on the histogram icon (red arrow) in the selection area, and with the cursor, visually choose the best threshold for your image (red circle in Figure C7.b).

a

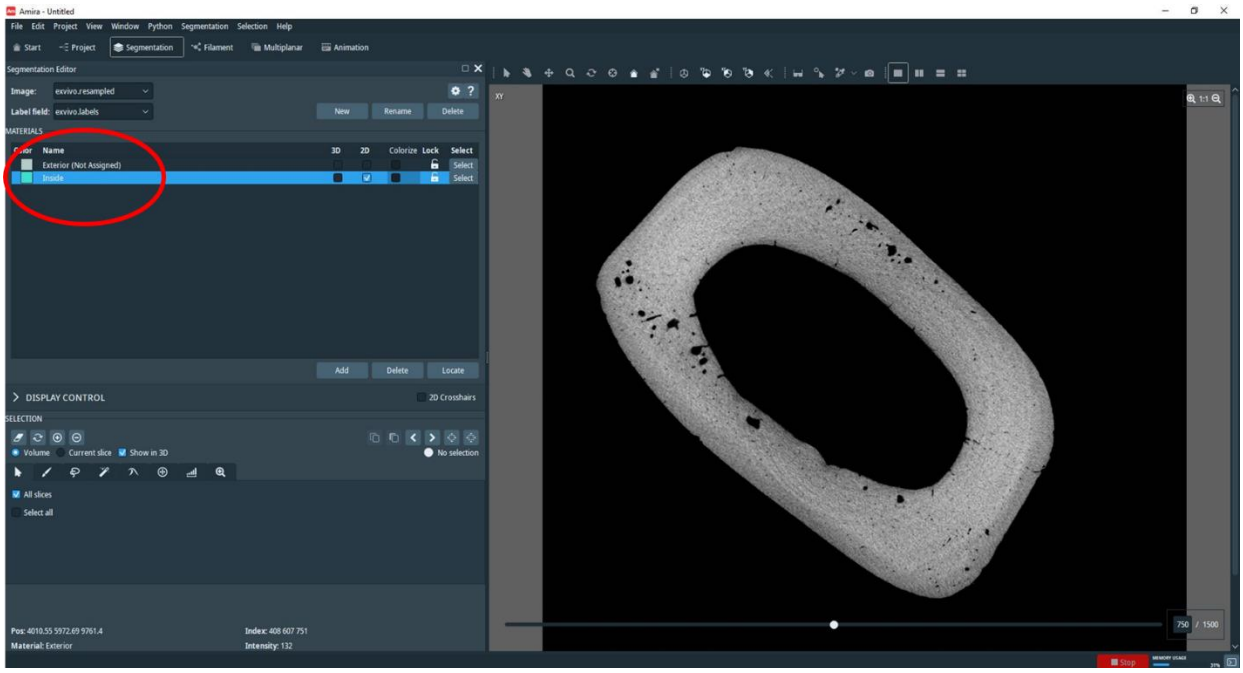

b

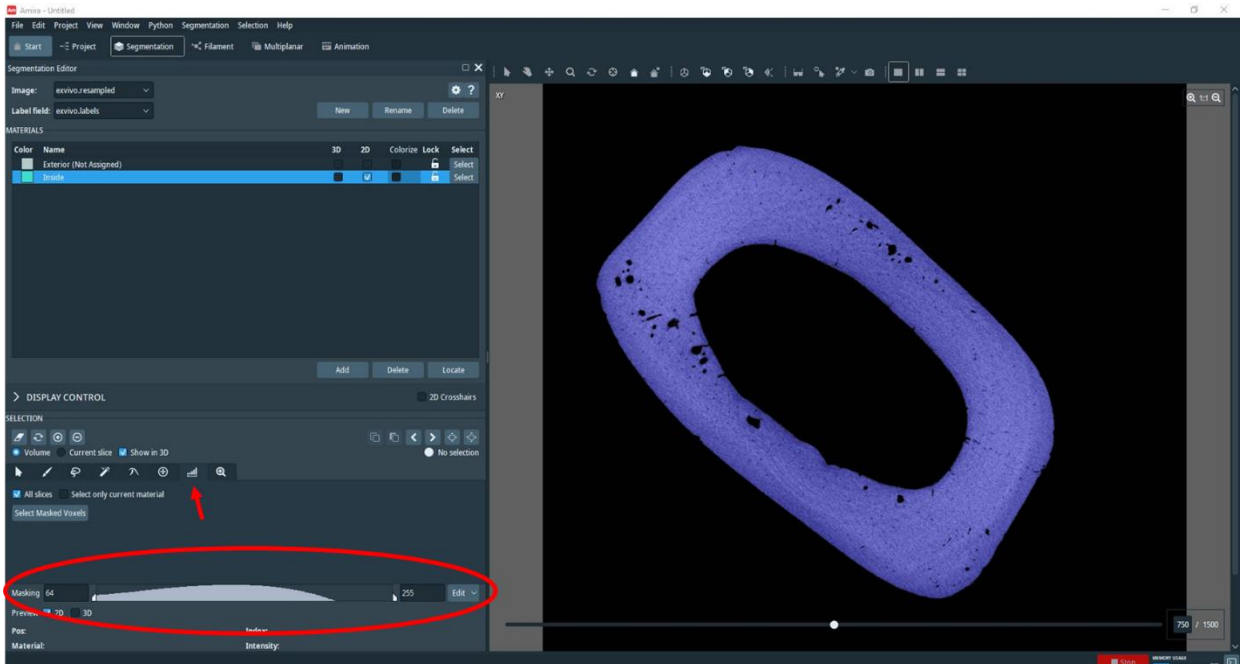

Figure C. 7. First steps for segmentation: (a) exterior and inside materials and (b) image histogram.

8. In this example, the best threshold was selected from 64 to 255. Next, click on select masked voxels. Make sure all slices are selected (red circle in Figure C8.a). Once this has been applied (entire image series masked), click on the + button (red circle in Figure C8.b). This action creates your inside material. Table C1 presents the threshold ranges used for the *in vivo* and *ex vivo* data sets used in this thesis.

Table C. 1. in vivo and ex vivo data sets threshold ranges

Rabbits	Threshold Ranges		
	***in vivo* View# 1**	in vivo **View# 2**	***ex vivo***
PTHW1	134 – 255	134 – 255	126 – 255
PTHW2	147 – 255	147 – 255	113 – 255
PTHW3	142 – 255	142 – 255	112 – 255
PTHW4	142 – 255	142 – 255	129 – 255
PTHW5	144 – 255	144 – 255	138 – 255
PTHW6	144 – 255	144 – 255	138 – 255
PTHW7	140 – 255	140 – 255	131 – 255
PTH1	147 – 255	147 – 255	127 – 255
PTH2	135 – 255	135 – 255	130 – 255
PTH3	130 – 255	130 – 255	105 – 255
PTH4	132 – 255	132 – 255	114 – 255
PTH5	132 – 255	132 – 255	122 – 255
PTH6	130 – 255	130 – 255	128 – 255
PTH7	139 – 255	139 – 255	114 – 255

a

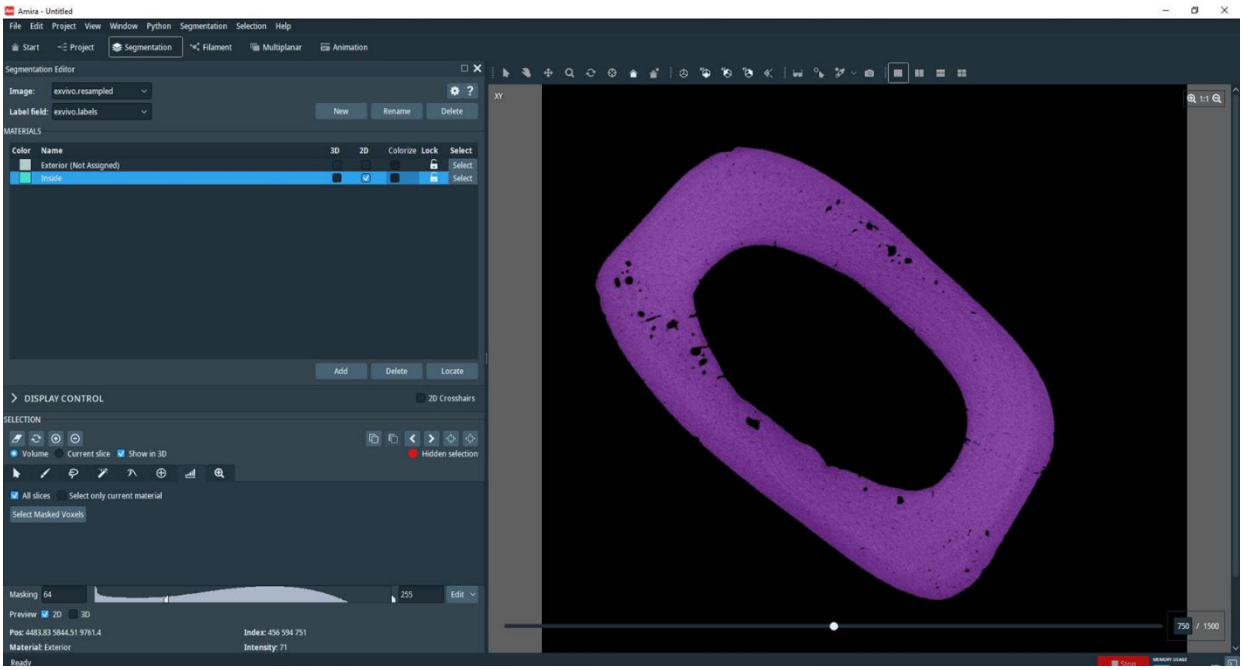

b

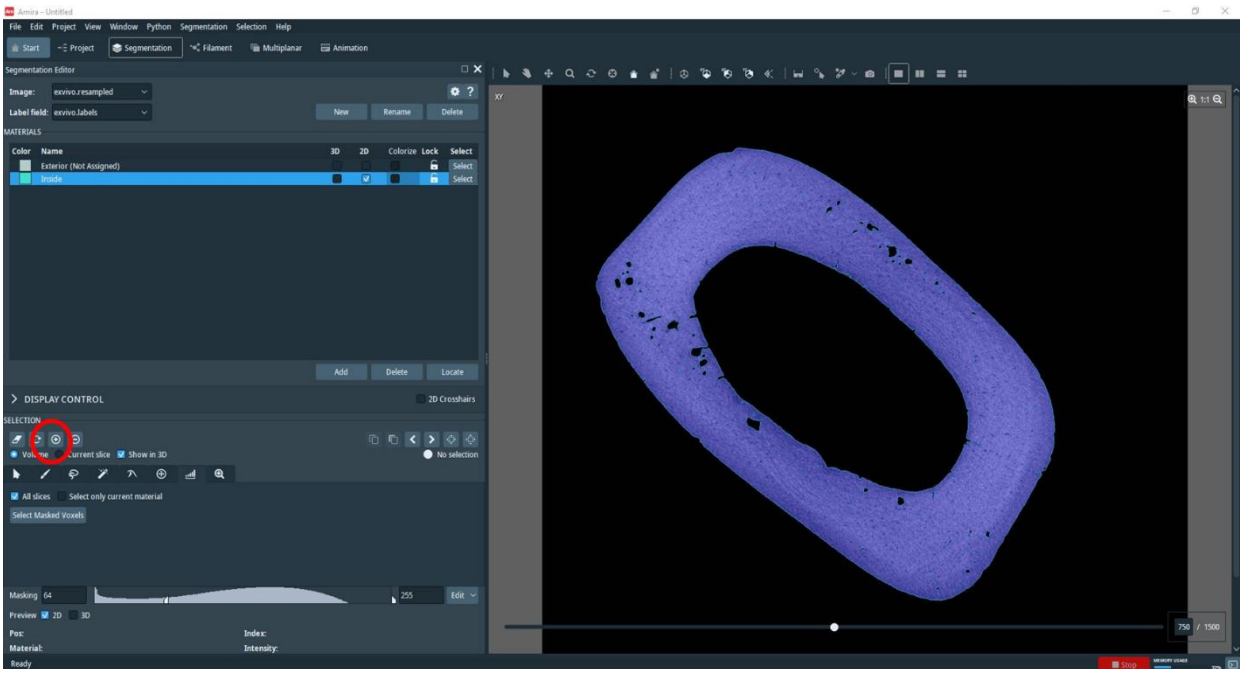

Figure C. 8. (a) Masked voxel selection. (b) + button to create inside material.

9. In the next step, click on the segmentation tab (red arrow), then click on remove islands. I used the remove islands to create a mask in the bone and pores. I set a value of 5000 voxels to make sure that the cortical bone and pores were connected. Next, select all slices and

then click apply. Once that is finished, click on close (Figure C9.a). Next, click on select inside material (red arrow). You will see that the bone and pores are segmented. In other words, both are now included in the segmentation (Figure C9.b).

a

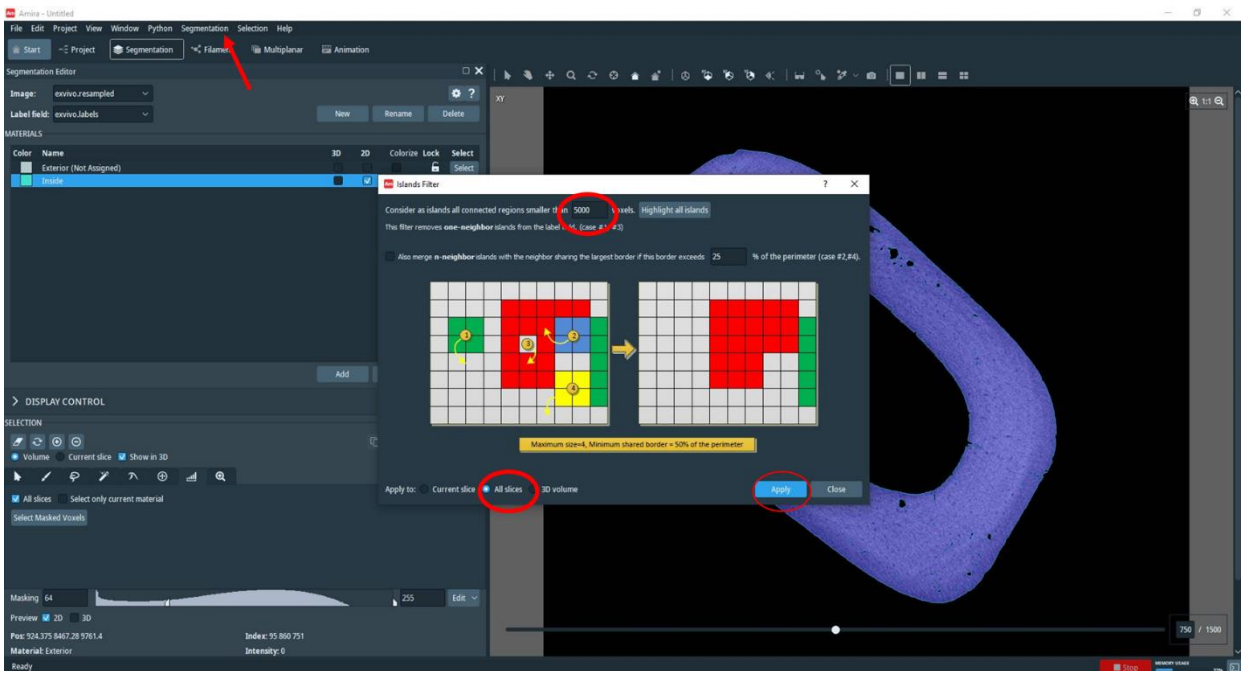

b

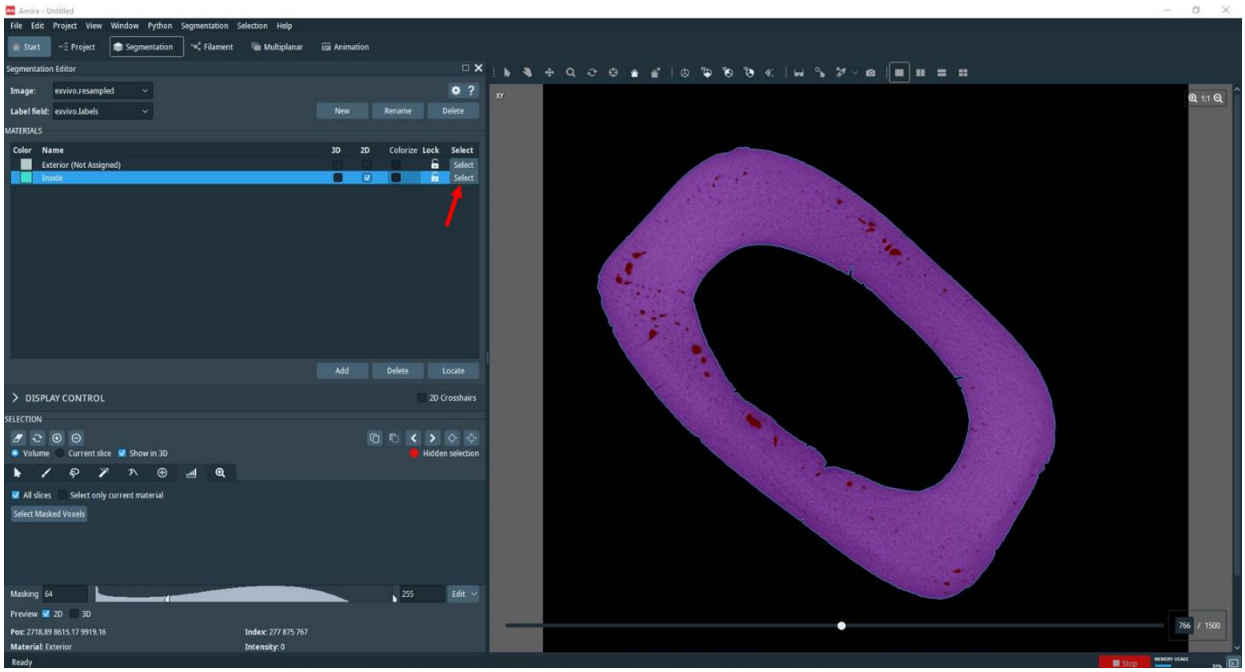

Figure C. 9. (a) Using remove islands to segment bone and pores. (b) Selecting inside material.

10. For the next step, click on the selection tab (red arrow in Figure C10) and then shrink all slices. This helped to remove new bone formation from the endosteal envelope, that could make the visualization of registration more difficult. In some data sets I had to apply it x2 or x3, depending on the amount of bone formation in each data set. After shrinking all slices, add new material (red circle in Figure C10); click on the button and add it to the materials area.

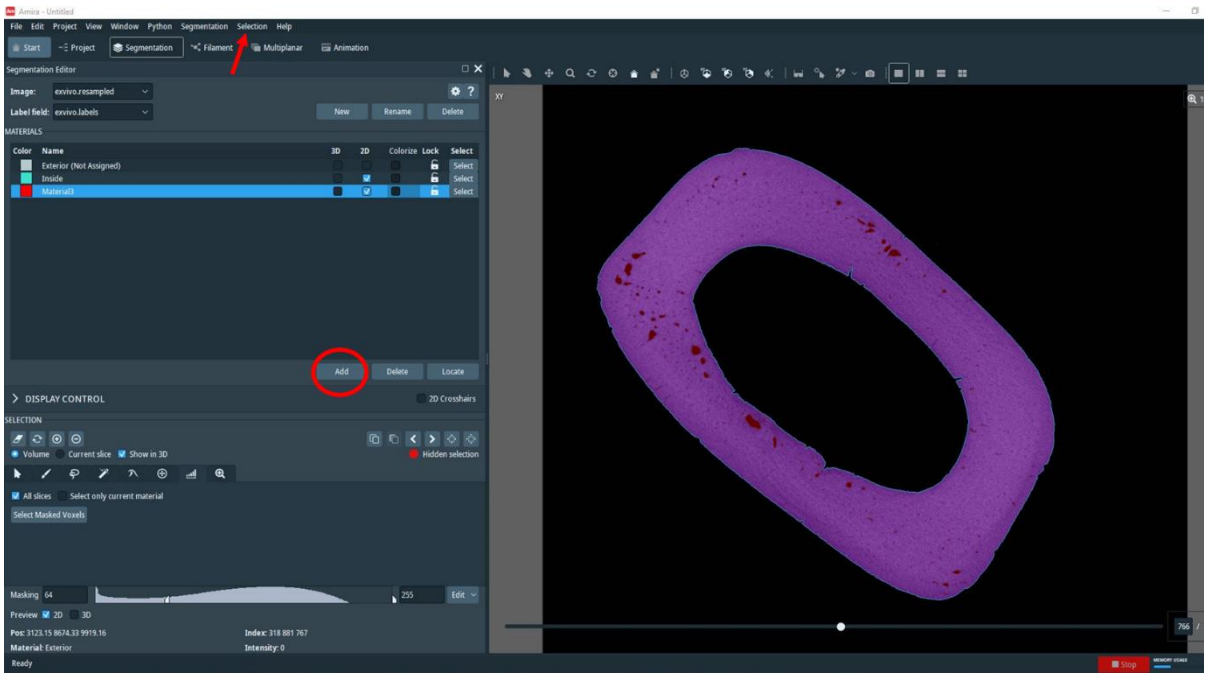

Figure C. 10. Using the shrink all slices.

11. In this example, the new material is material 3 (in red). You can see that material 3 is selected. Then, click on the + button in the selection area (red arrow in Figure C11). You will see a red mark around your image (two red arrows in the XY slice in Figure C11).

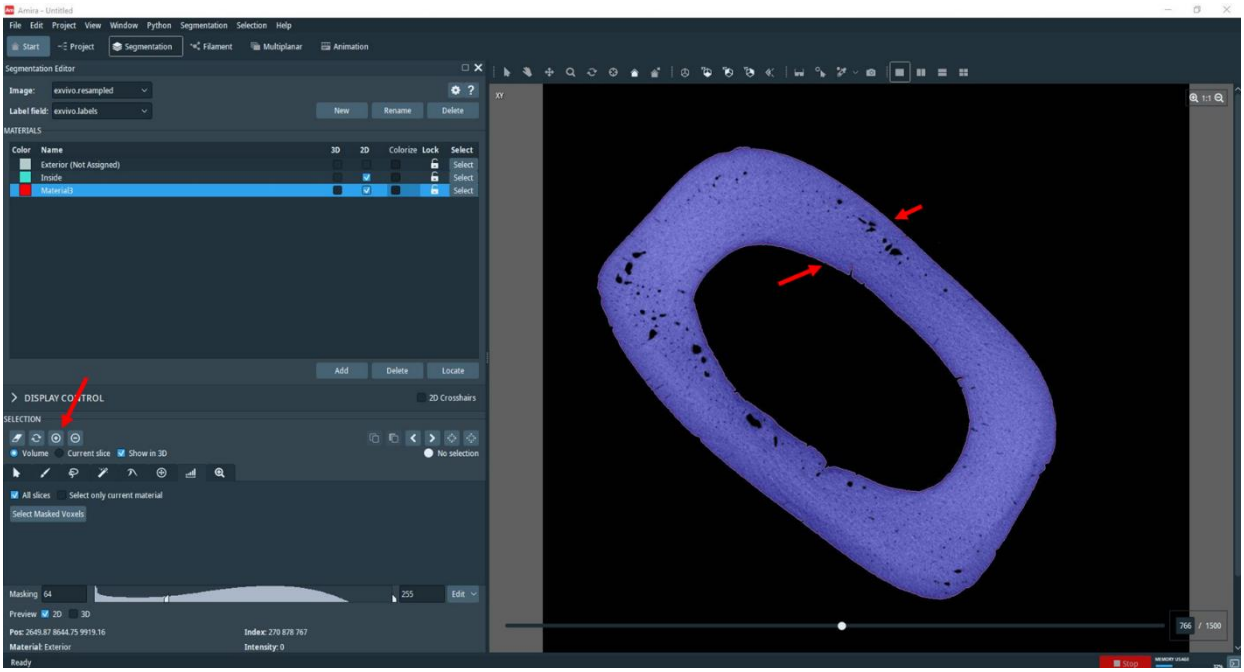

Figure C. 11. Creating material 3.

12. With material 3 still selected, go to the selection area and click on select only current material (red arrow in Figure C12.a). Next, invert the image threshold (in this example, from 0 to 64 in Figure C12.b). With this action, you can see the pores are blue and ready to be segmented. Next, click on select masked voxels (red circle in Figure C12.b).

a

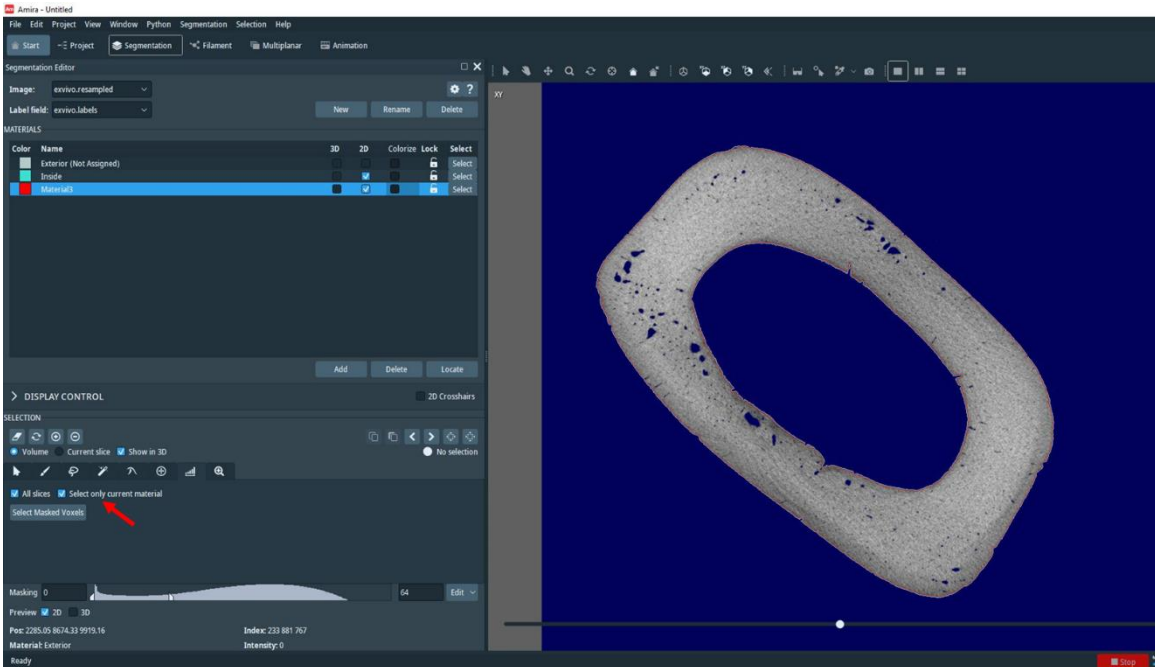

b

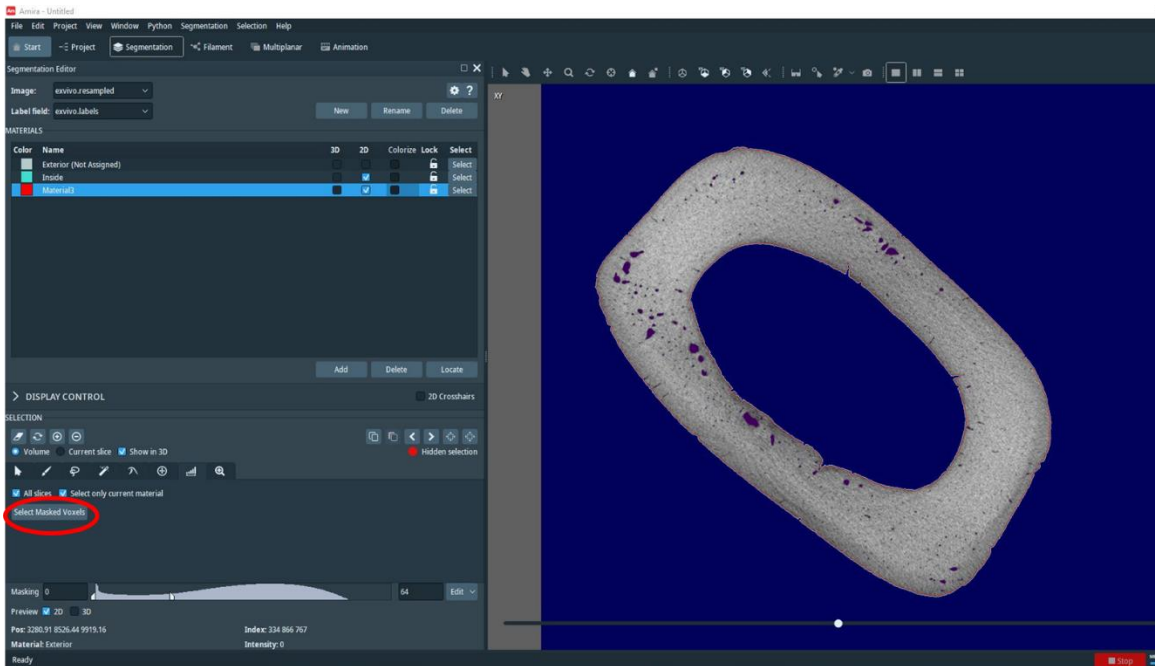

Figure C. 12. Creating material 4: (a) selecting only current material (red arrow) and (b) selecting masked voxels (red circle),

13. As your pores are now masked, add a new material (material 4 in Figure C13.a). With material 4 selected, click in the + button (red circle in Figure C10.b). You can see a pink mark around the pores.

a

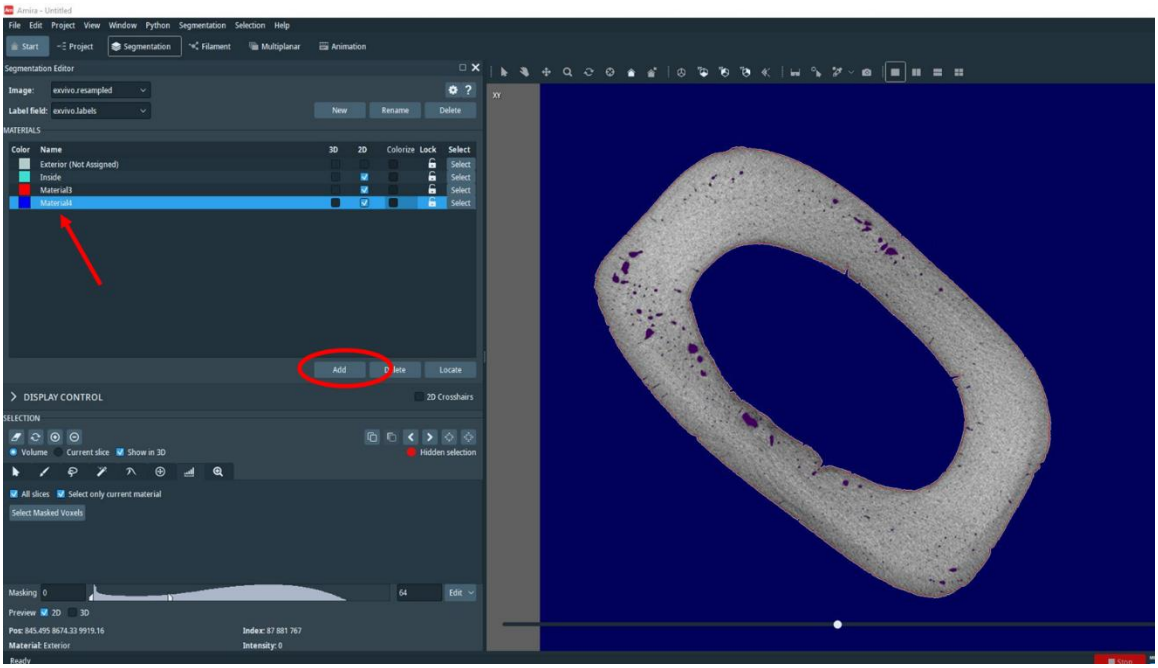

b

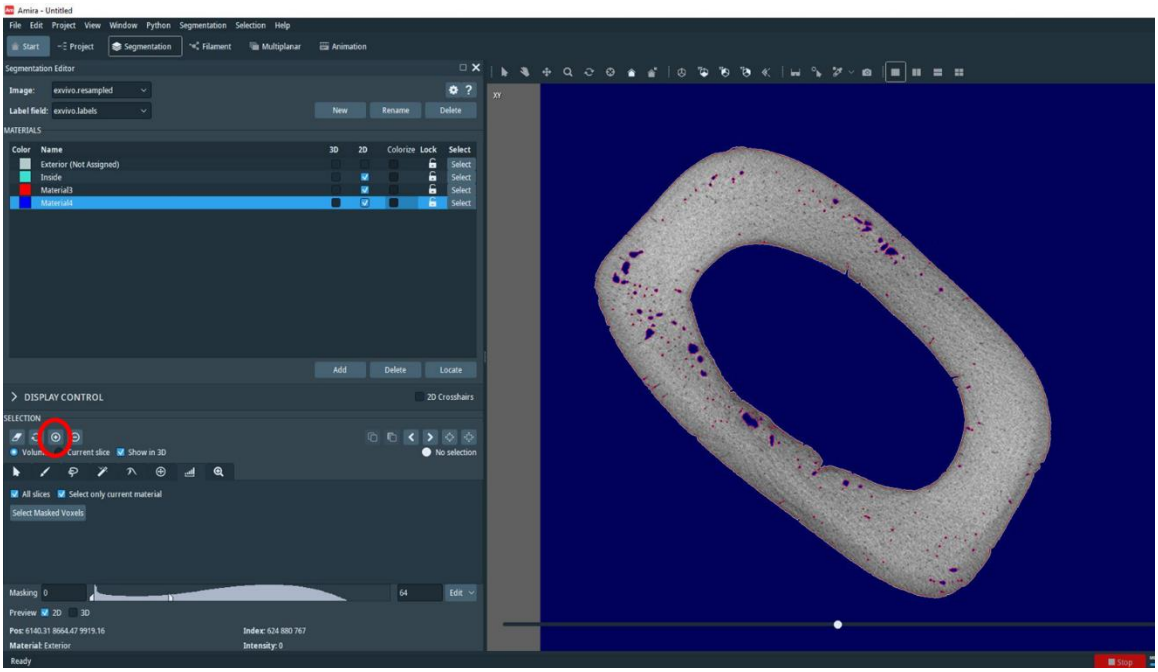

Figure C. 13. (a) Adding material 4 (red circle). (b) Inserting the pores in material 4 (red circle).

14. To see the pores segmented, click on the select icon in material 4 (red arrow in Figure C14). Then, click on the single viewer to see the pores in 3D (red arrow in Figure C14).

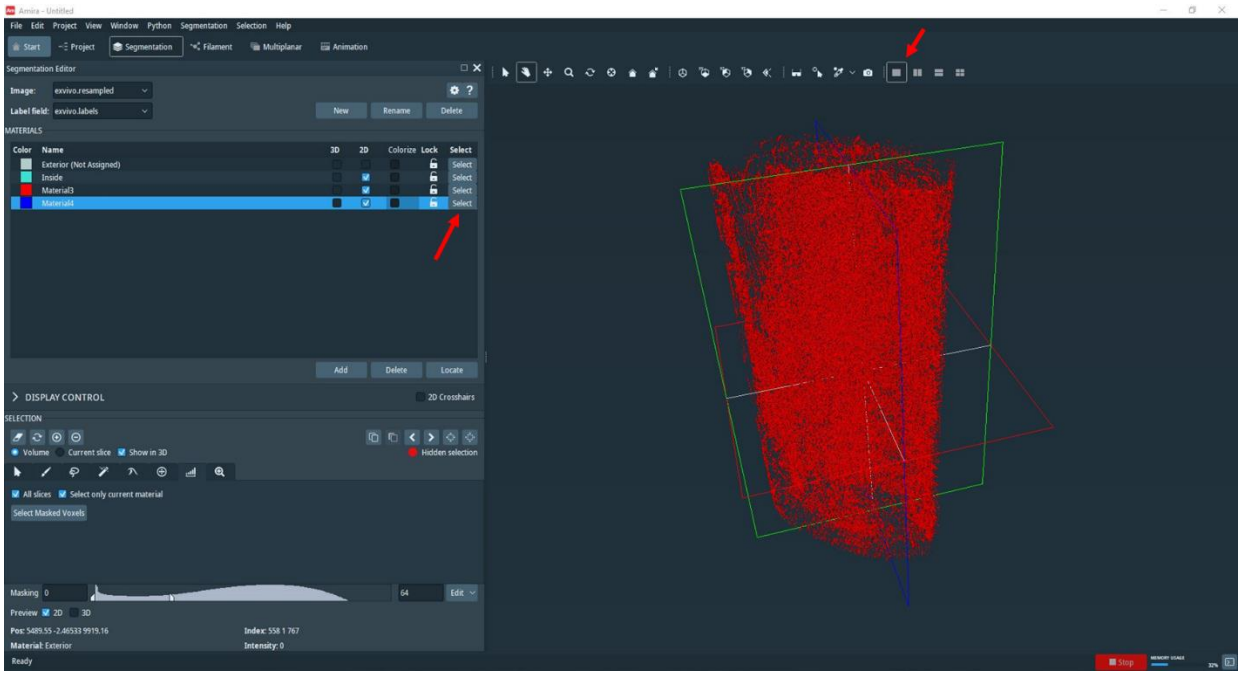

Figure C. 14. Visualizing the segmented pores in 3D.

C.2. 3D Registration

In this section I describe how the 3 data sets (View #1 and View #2 *in vivo* and *ex vivo*) used in this thesis were registered using the Amira software (version 6.2). The same methodology can be used to register 2 data sets.

1. Once you have finished segmenting your data sets as described in the previous section, click on the project tab. You will see your data sets with labels in the project view area (Figure C15).

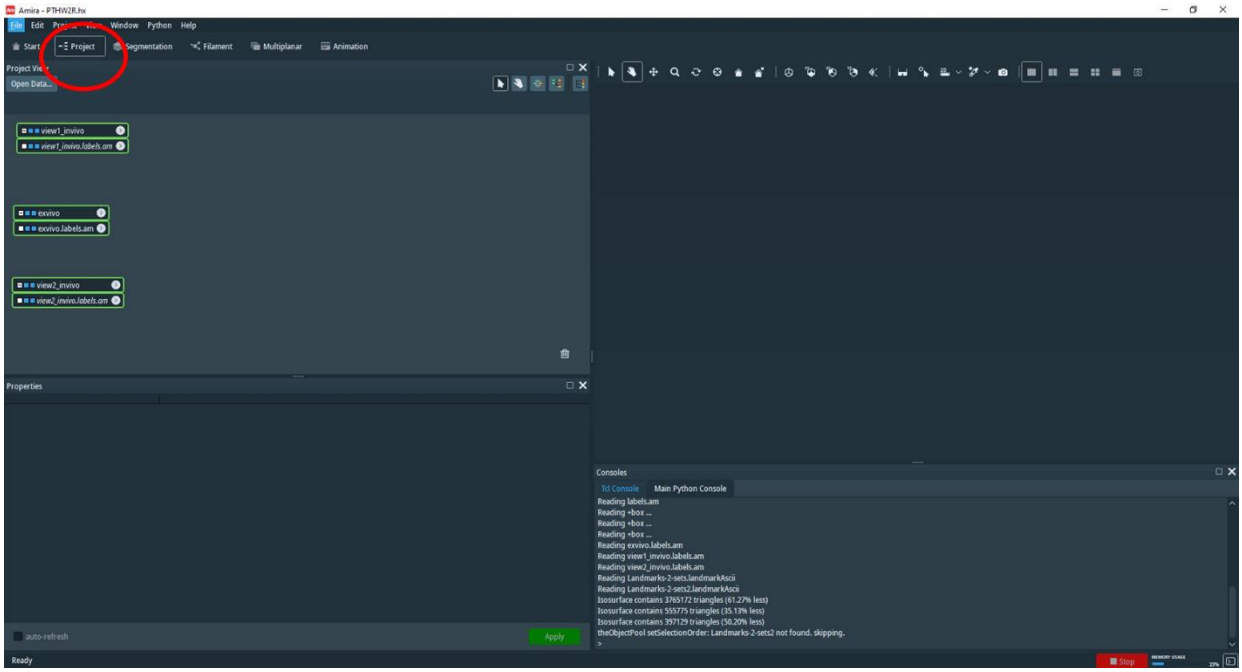

Figure C. 15. Data sets in the project view area

2. Click on each data set, then choose display> volren > create (Figure C16.a and b).
3. This way, you will be able to see your data sets in 3D (Figure C17).

a

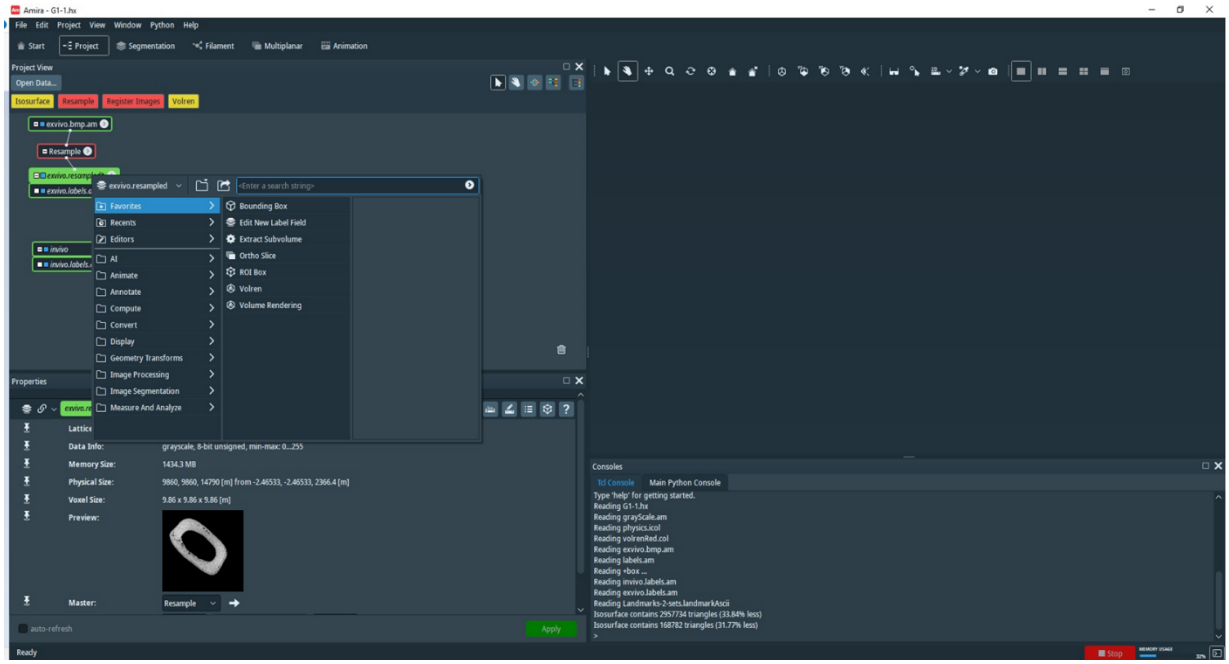

b

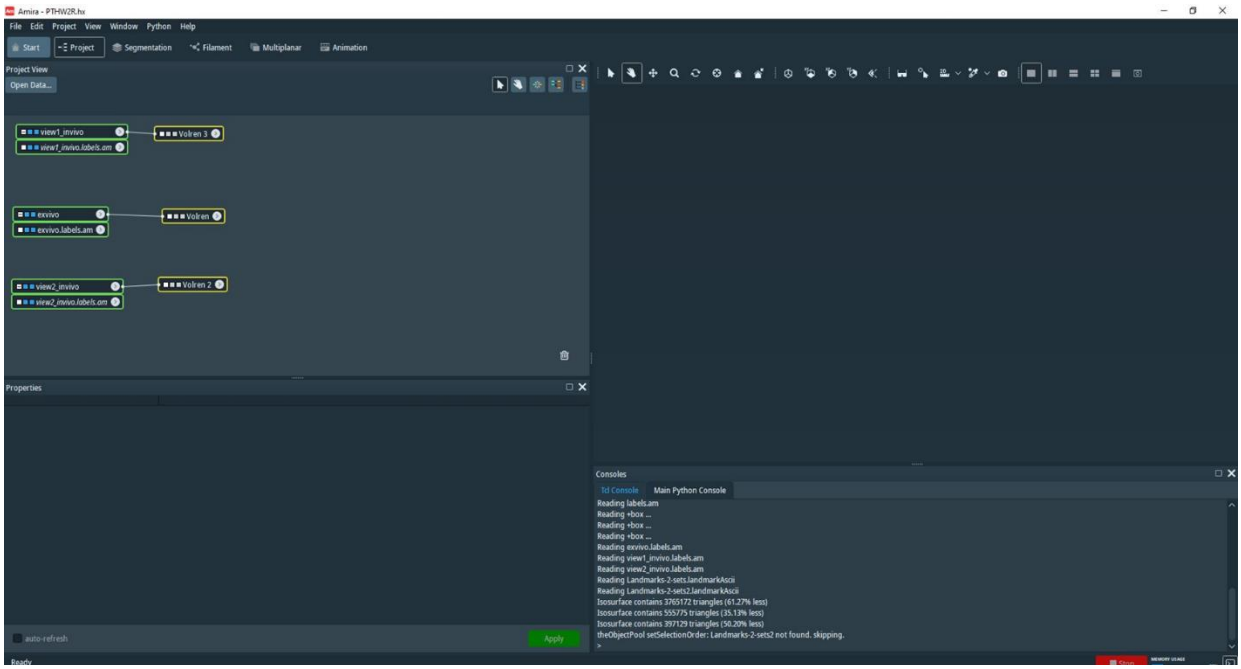

Figure C. 16. (a) Click on the image and choose to display volren. (b) Data sets with the volren modules.

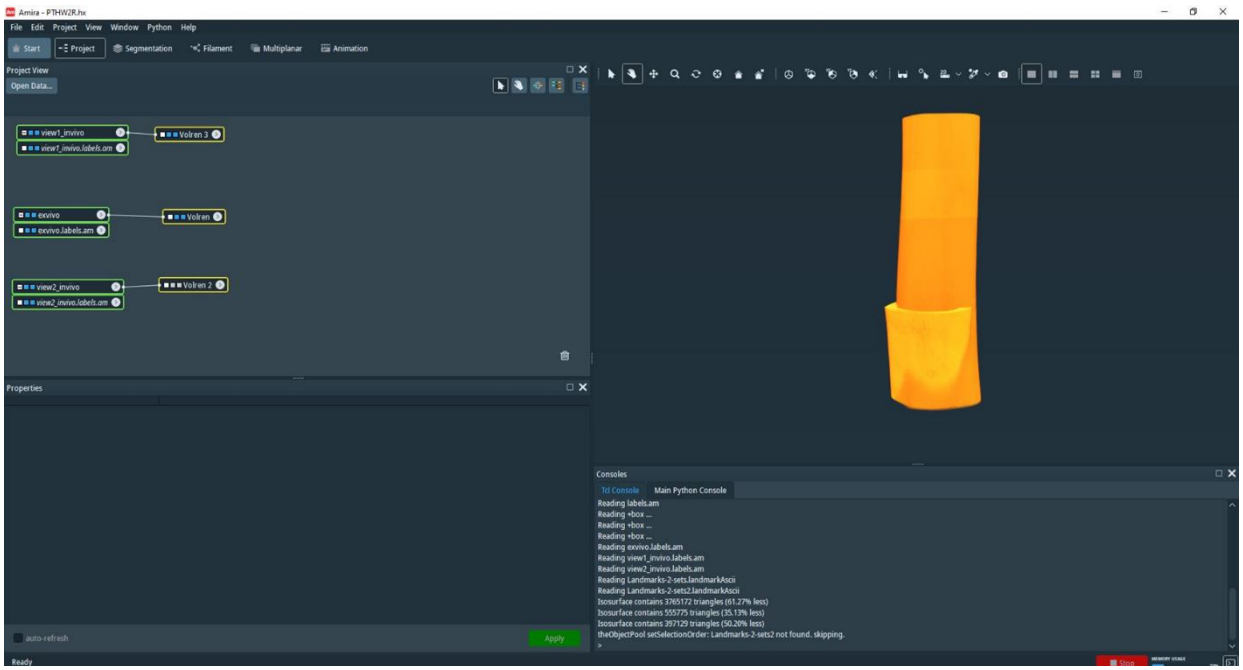

Figure C. 17. Volrens displayed in 3D

4. Before applying automatic registration, you must manually align your data sets. That will help with the automatic registration. For this thesis, the *in vivo* data sets were manually adjusted (the model), and the *ex vivo* data set was stationary (the reference). First, click on the View #1 data set (red arrow), and in the properties area, click on the transform editor icon (small green circle). You can see a bounding box that will allow you to rotate and translate the data set (white arrow). Use the arrow cursor (small white circle) to move your data set (Figure 18A.a). When your data set is ready, you can go to the registration. Click on the View #1 data set > geometry > transform > register images > create (Figure 18A.b).

a

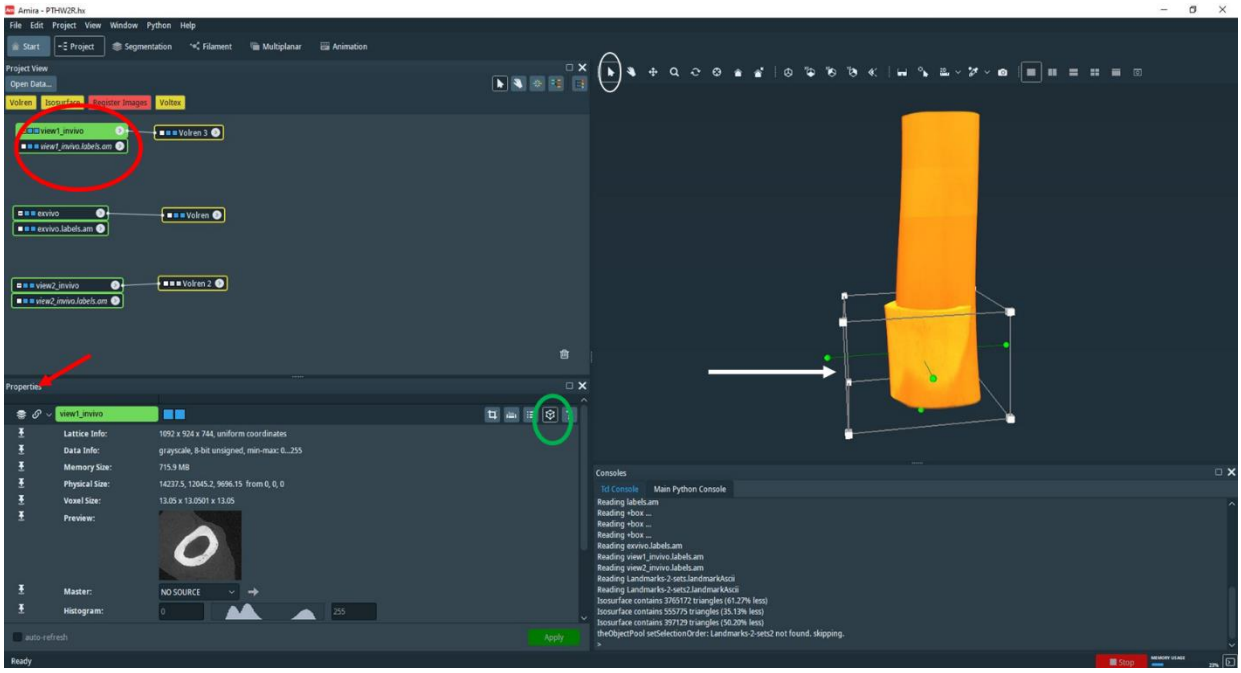

b

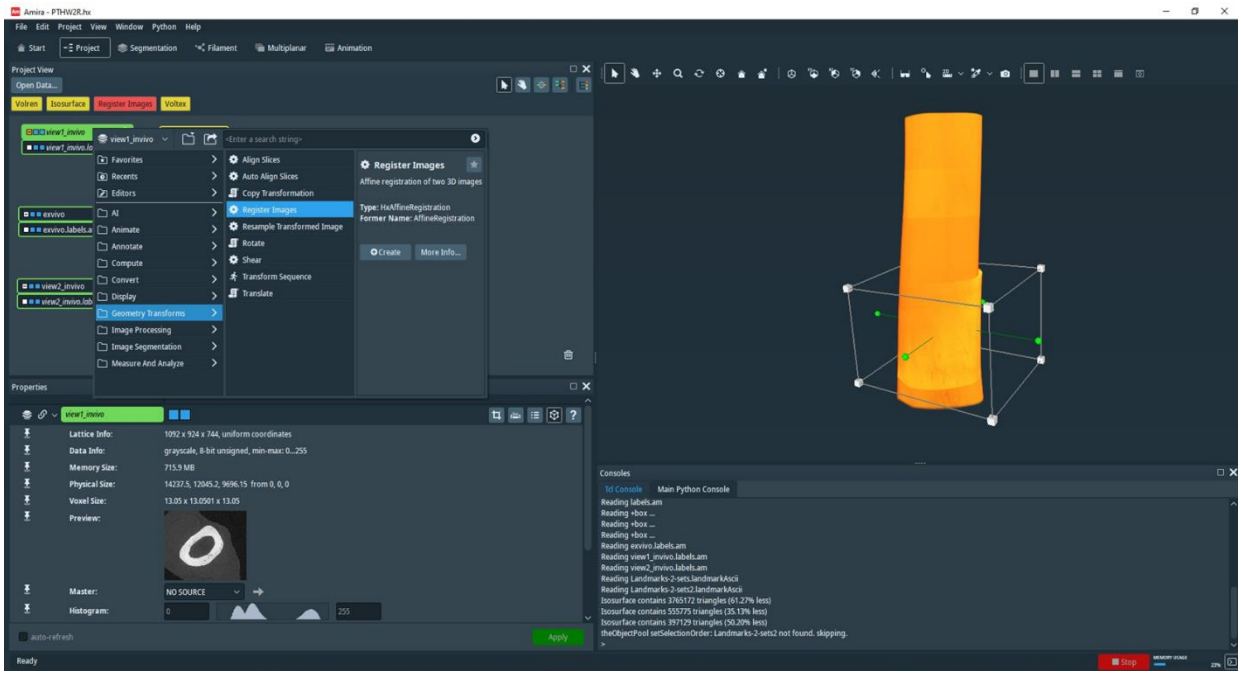

Figure C. 18. (a) Manual alignment of View #1 *in vivo* data set. (b) Creating your registration module.

5. As you have created your registration module (red circle in Figure 19A), go to the properties area and choose the model (View #1) and reference (*ex vivo*) (white circle in Figure 19A). Click on rigid+Iso-scale and choose the metric correlation (or mutual information) and then click apply (Figure 19A).

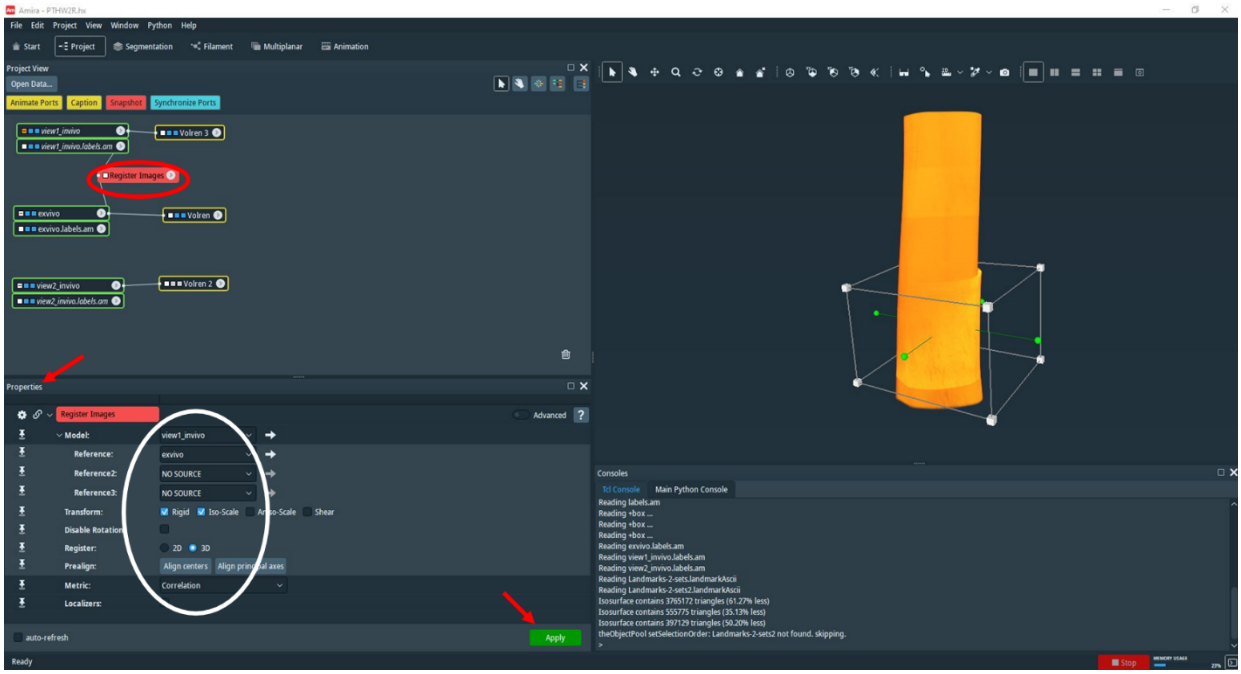

Figure C. 19. Applying automatic registration.

6. Now you must register View #2. Go back to the project view area and turn off the View #1 volren, as you have already registered it, and turn on View #2 (Figure C20.a). Click on the View #2 data set (red circle in Figure C20.a), and in the properties area (red arrow in Figure C20.a), click on the transform editor icon (green circle in Figure C20.a). Manually adjust (rotation and translation) your data set (white arrow in Figure C20.a). Use the arrow cursor (white circle) to move your data set to the best position (Figure C20.a). Once your View #2 is ready, then go to the registration. Click on View #2 data set > geometry > transform > register images > create (Figure C20.b).

a

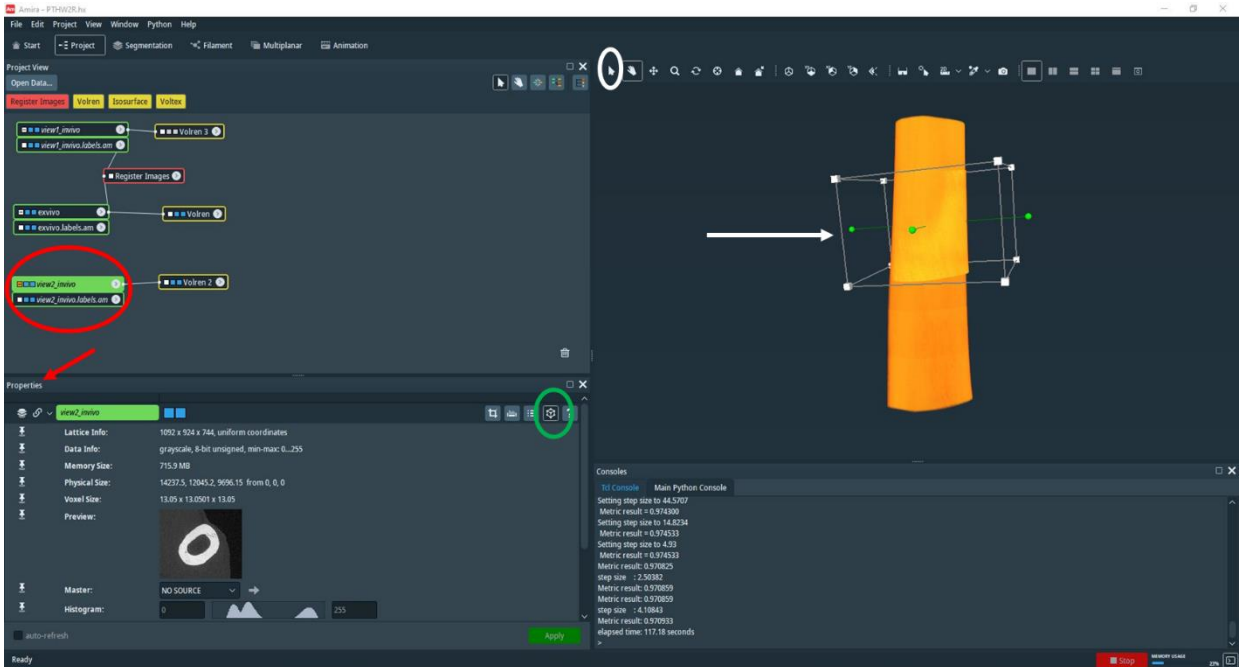

b

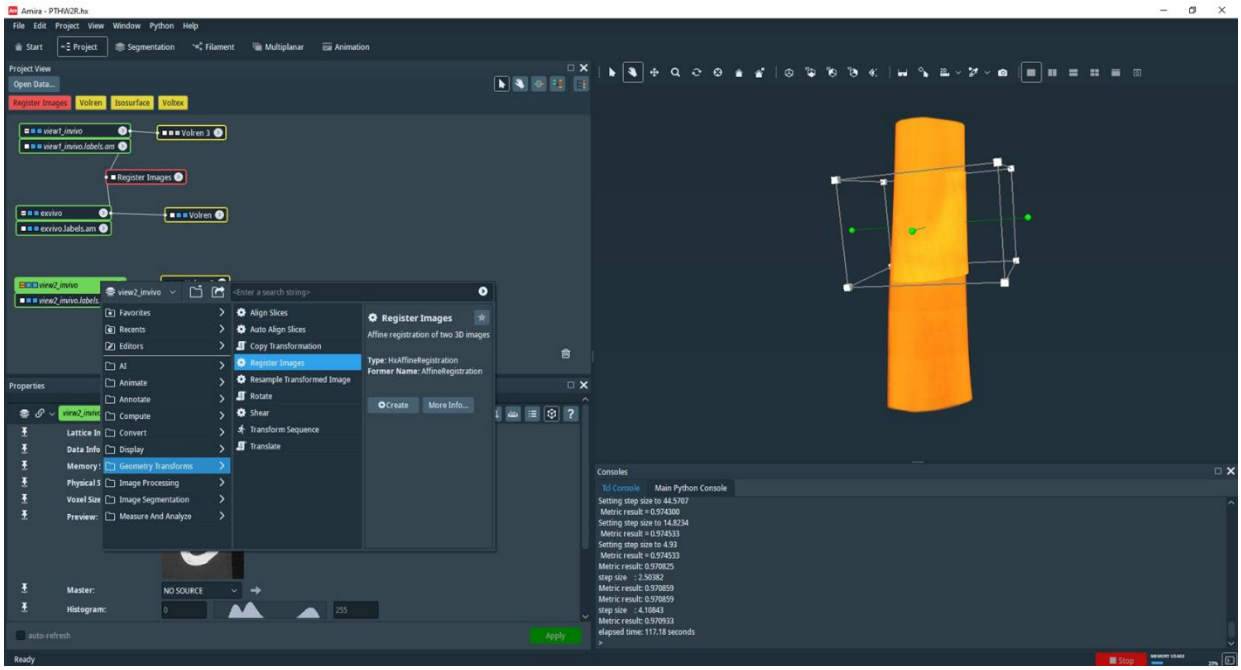

Figure C. 20. (a) Manual alignment of View #2 *in vivo* data set. (b) Creating your registration module.

7. In this case, View #2 is the model, and *ex vivo* and View #1 are the references (white circle in Figure C21.a). Use the same transformation and metric as described above. Then, click apply (red arrow in Figure C21.a). Once your registration is done, you can turn on the View #1 volren. Now you can see the 3 data sets registered (Figure C21.b).

a

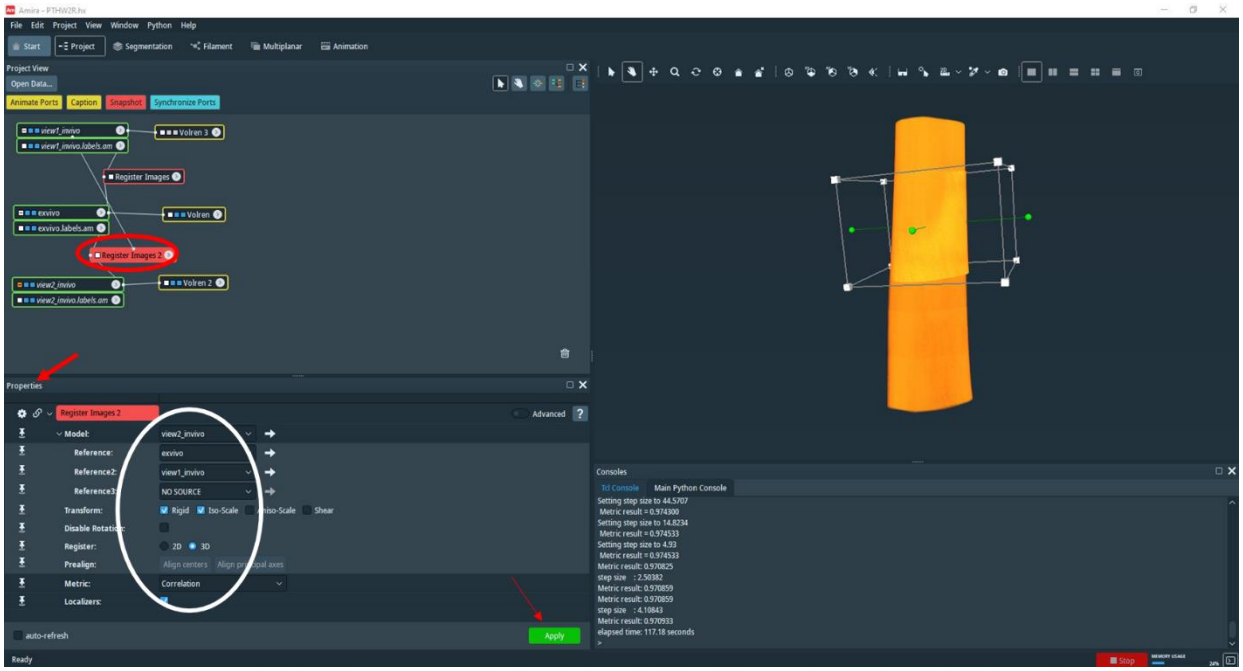

b

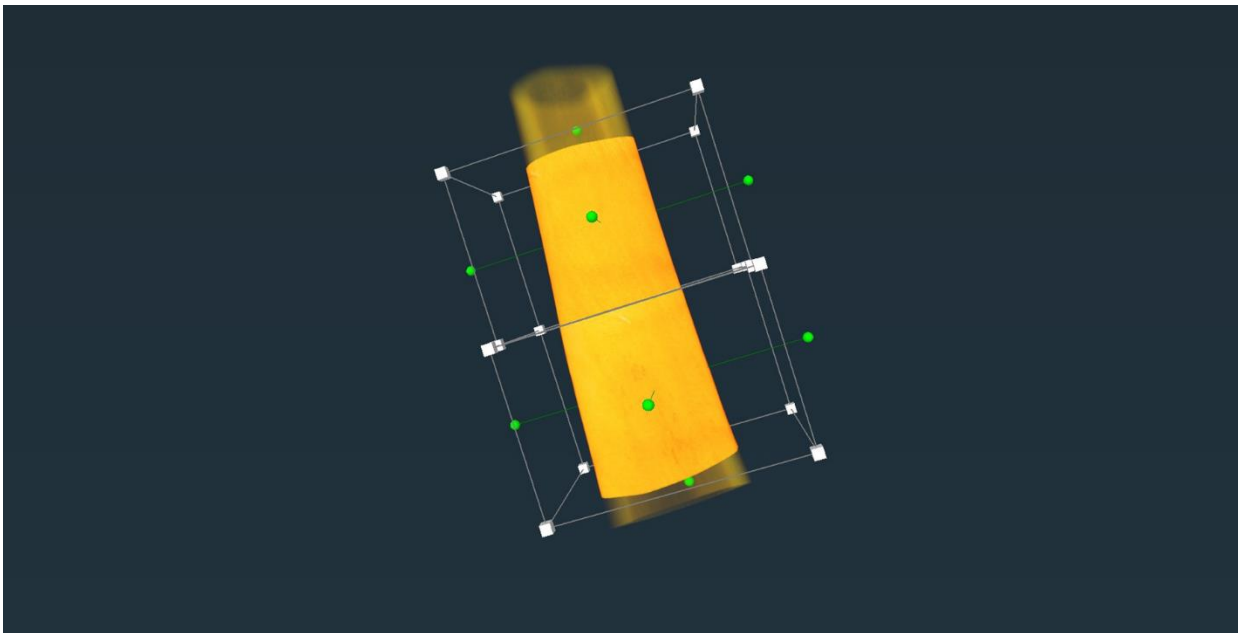

Figure C. 21. (a) Applying automatic registration. (b) The 3 data sets registered.

8. To inspect your registration, go back to the project view area and turn off all the volrens (Figure C22).

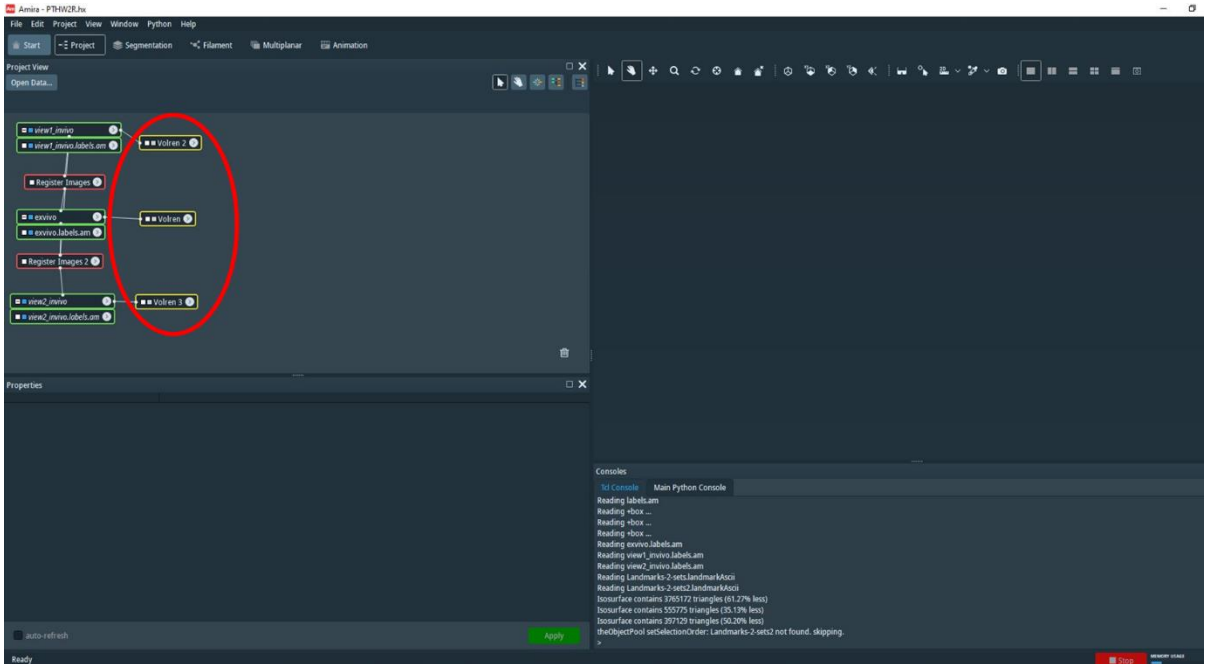

Figure C. 22. Turning off volrens in the project view area.

9. With volrens off, click on the labels of each data set, as in this example: ex vivo.labels> display > isosurface > create (Figure C23.a). Now do the same for the View #1 and View #2 *in vivo* data sets. With these actions, you have created your isosurface modules (red arrows in Figure C23.b). Click on the threshold (properties area) and click apply (Figure C23.b).

a

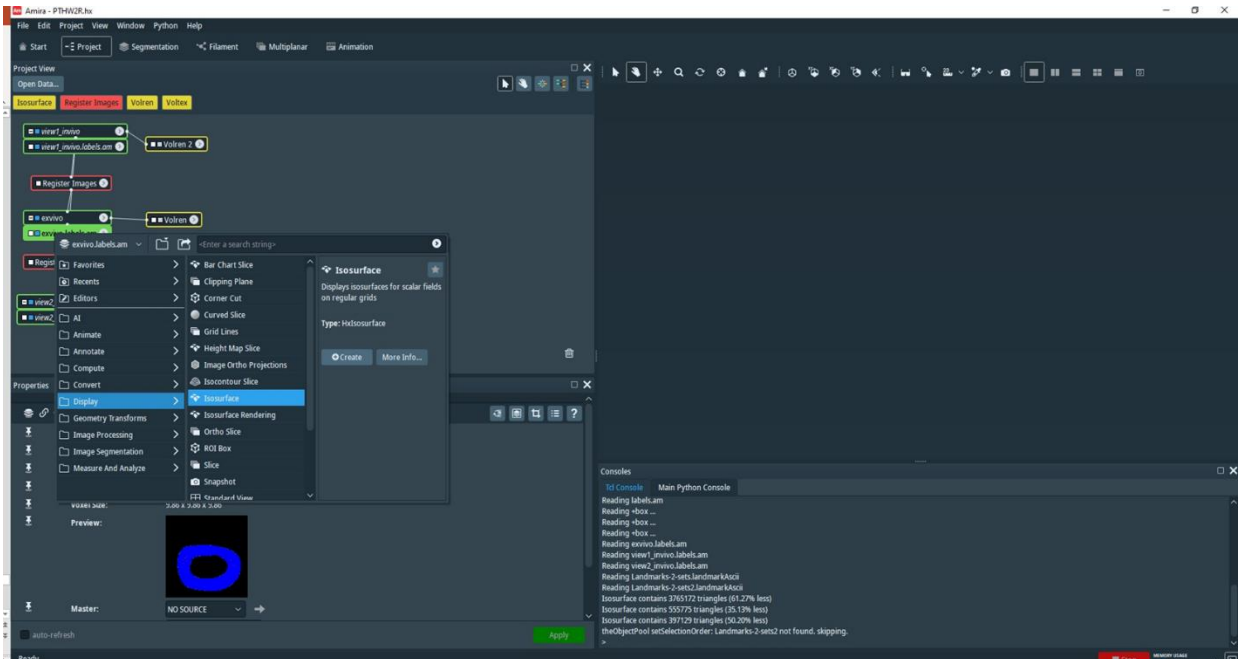

b

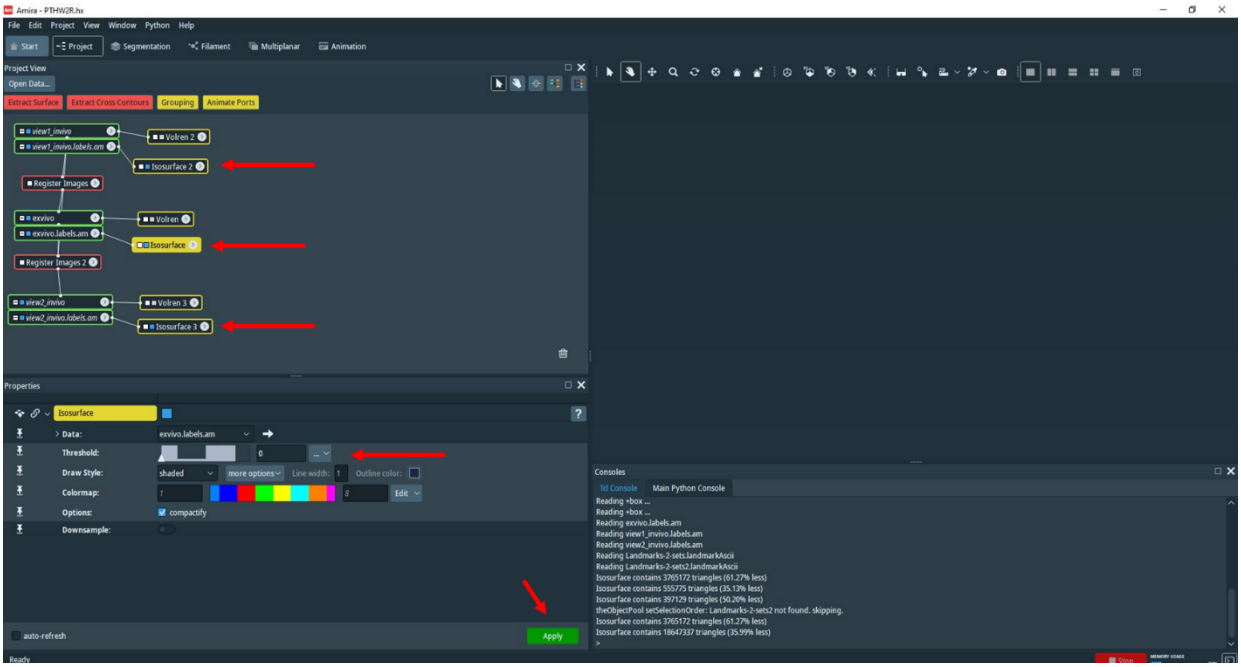

Figure C. 23. (a) Creating isosurface modules. (b) Choosing the threshold for the isosurfaces.

10. You can choose different colors for your threshold. In this example, the *ex vivo* BMUs are in white, View #1 *in vivo* BMUs are in blue, and View #2 *in vivo* BMUs are in red (Figure C24).

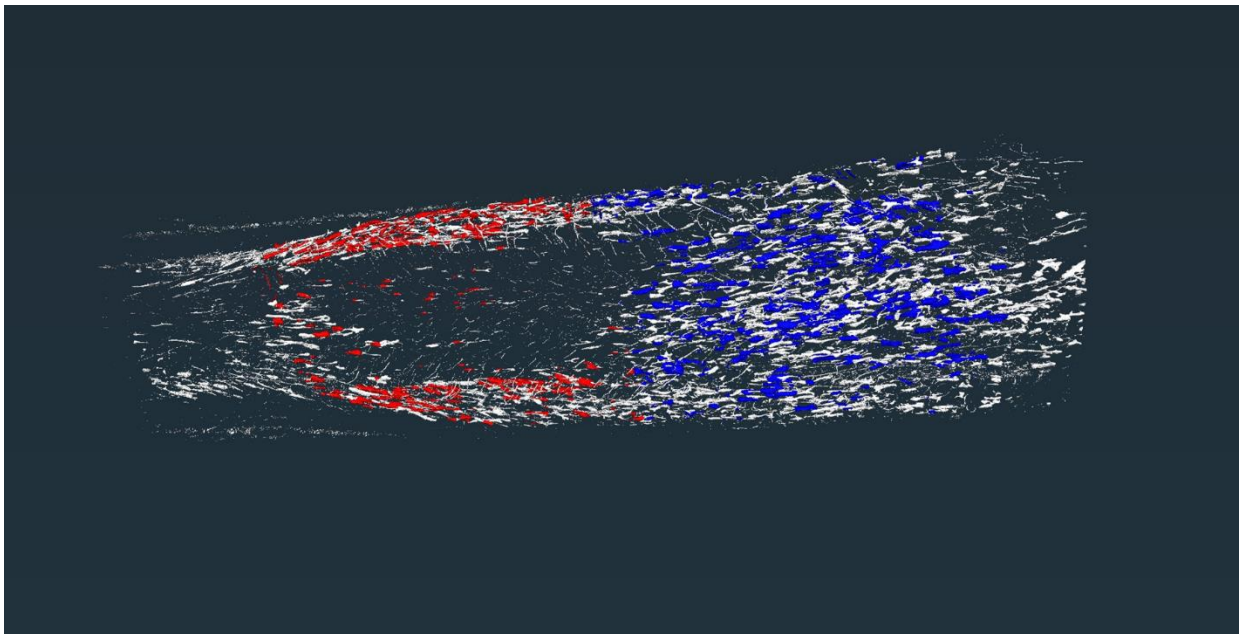

Figure C. 24. *Ex vivo* BMUs are in white, View #1 *in vivo* BMUs are in blue, and View #2 *in vivo* BMUs are in red.

B.3. LER Quantification

In this section, I describe how to landmark basic multicellular unit (BMU) using Amira software (version 6.2). For this thesis, we used two landmarks: one in the BMU *in vivo* and another in the BMU *ex vivo*. This way, the 3D coordinates of each BMU were computed, which enabled quantification of the distance between them. LER was calculated as the distance between BMUs divided by the time between *in vivo* and *ex vivo* image acquisition, as described in Section 3.2.4. BMUs were landmarked as described below.

1. With all isosurfaces on, click on the project view area (red circle in Figure C25) and choose create object. Search for landmark and click on landmarks (2sets).

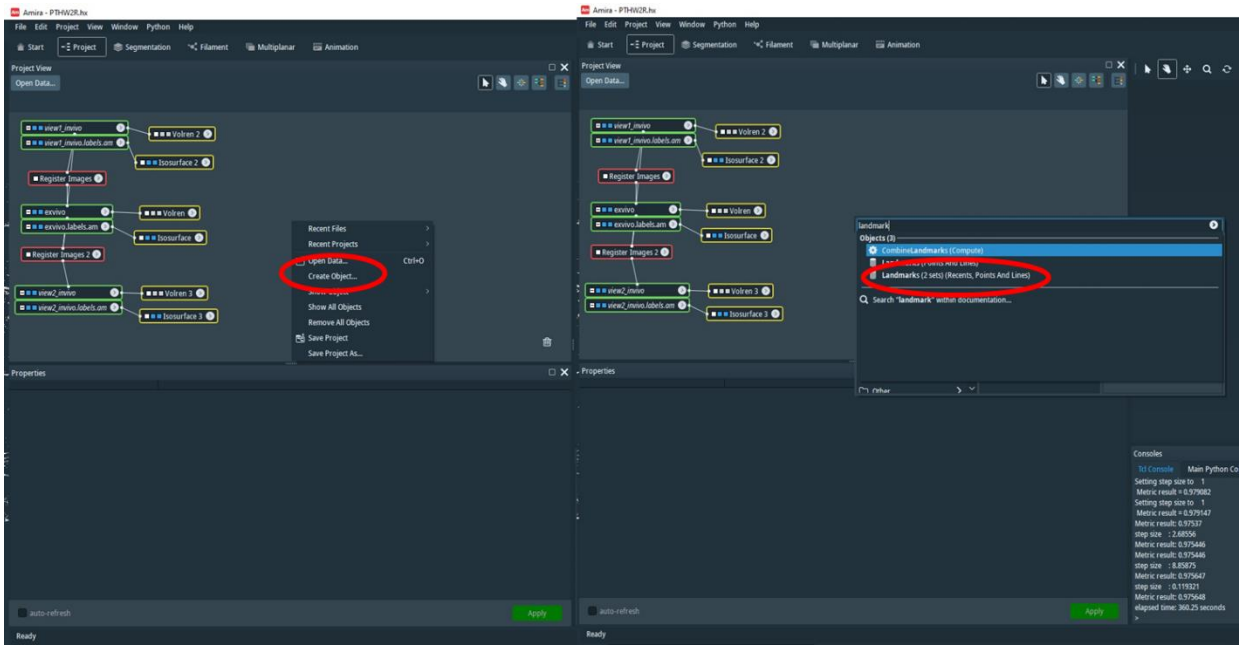

Figure C. 25. Creating landmarks-2sets.

2. Now you can see the landmarks-2sets module in the project view area (red circle in Figure C26.a). To connect the landmarks, click on landmarks-2sets and go to the properties area (Figure C26.b). Choose image set1: view#1 and image set2: ex vivo. Now you can see that the object landmarks-2sets is connected to the two data sets (Figure C26.b).

a

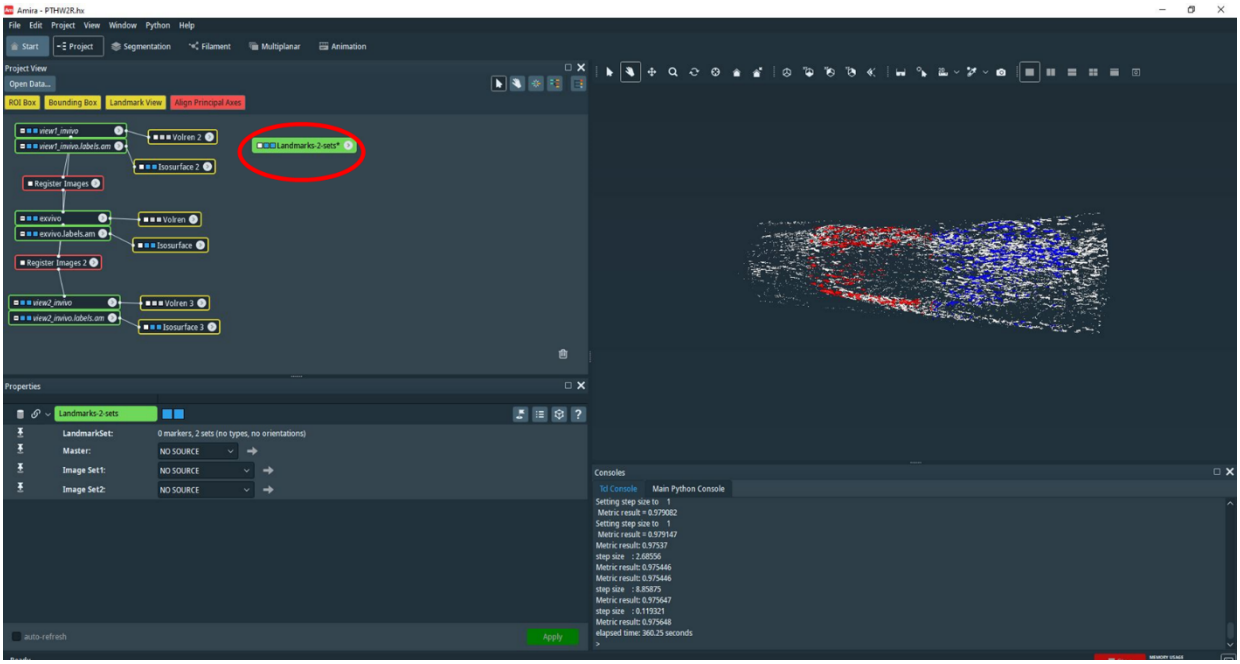

b

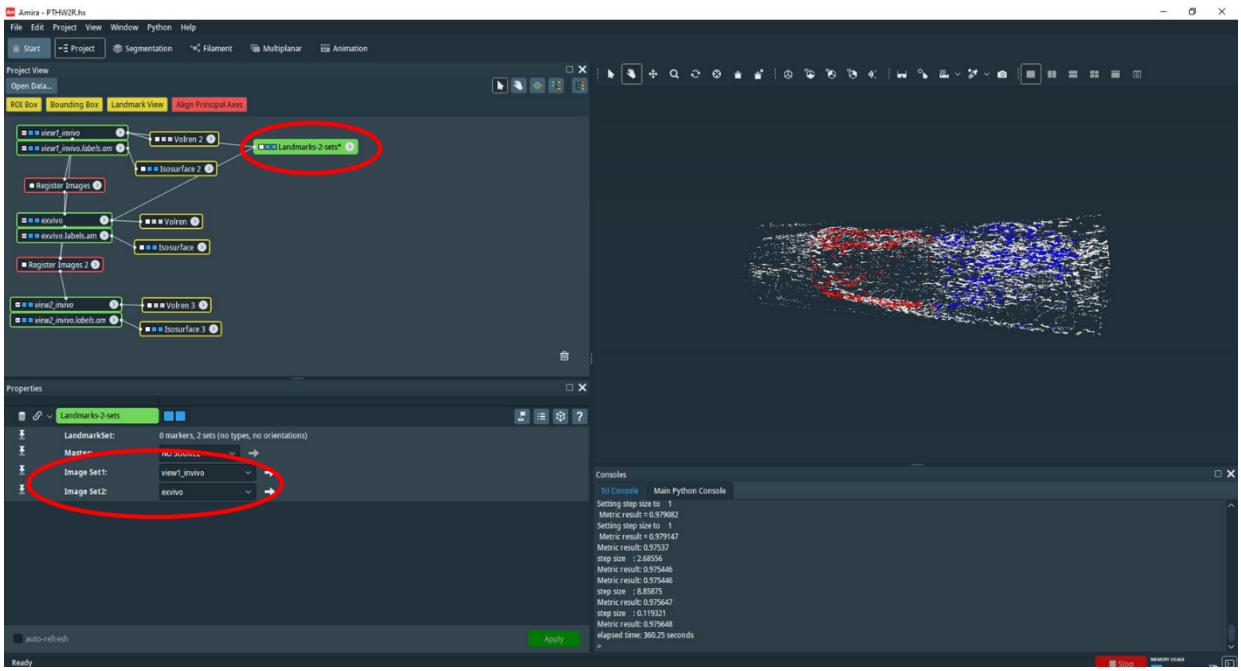

Figure C. 26. (a) Landmarks-2sets module in the project view area (red circle). (b) Choosing image set 1 (View #1 in vivo) and set 2 (ex vivo).

3. Next, click on landmark editor (flag icon in the properties area – Figure C27). In the landmark editor, you can add or remove landmarks and choose the marker type. In this example, the marker type was point (Figure C27).
4. Click on the landmark view module in the project view area (red circle in Figure C28.a) to change the size and complexity of the landmarks. In this example, line (size 0.3) and complexity 1 (Figure C28.a) were used. Now you are ready to start to landmark BMUs. Use the extra viewer to landmark BMUs. Zoom in on BMUS you want to mark. Choose the arrow cursor and click on the tip of the BMU *in vivo* (blue); then click on the tip of the BMU *ex vivo* (white). Now you can see the two landmarks: gold (*in vivo*) and blue (*ex vivo*) (green circle Figure C28.b). Repeat this procedure for the other BMUs.

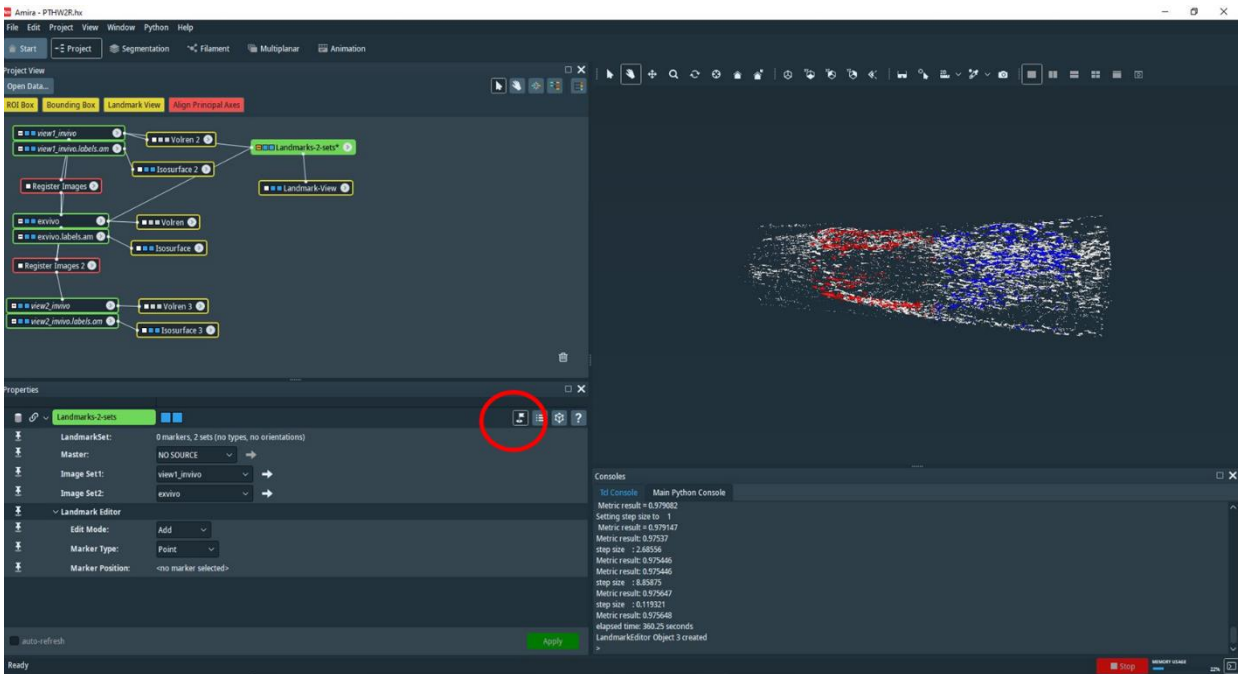

Figure C. 27. Landmark editor (flag icon on the properties area).

a

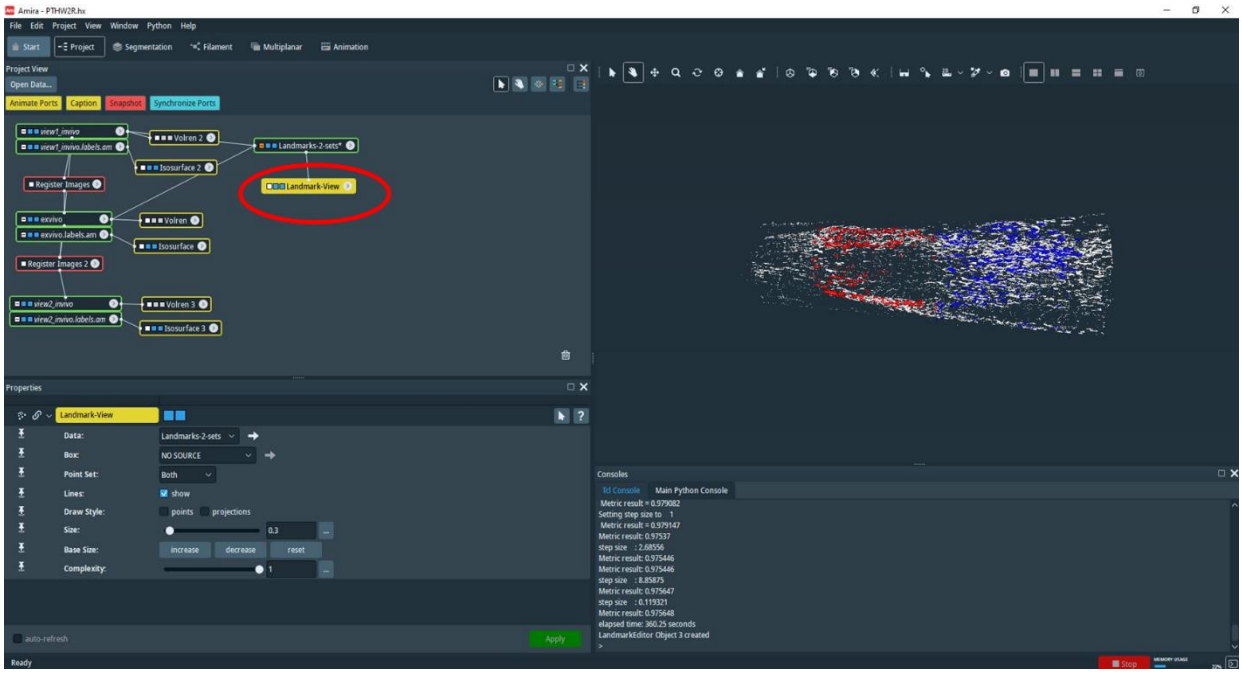

b

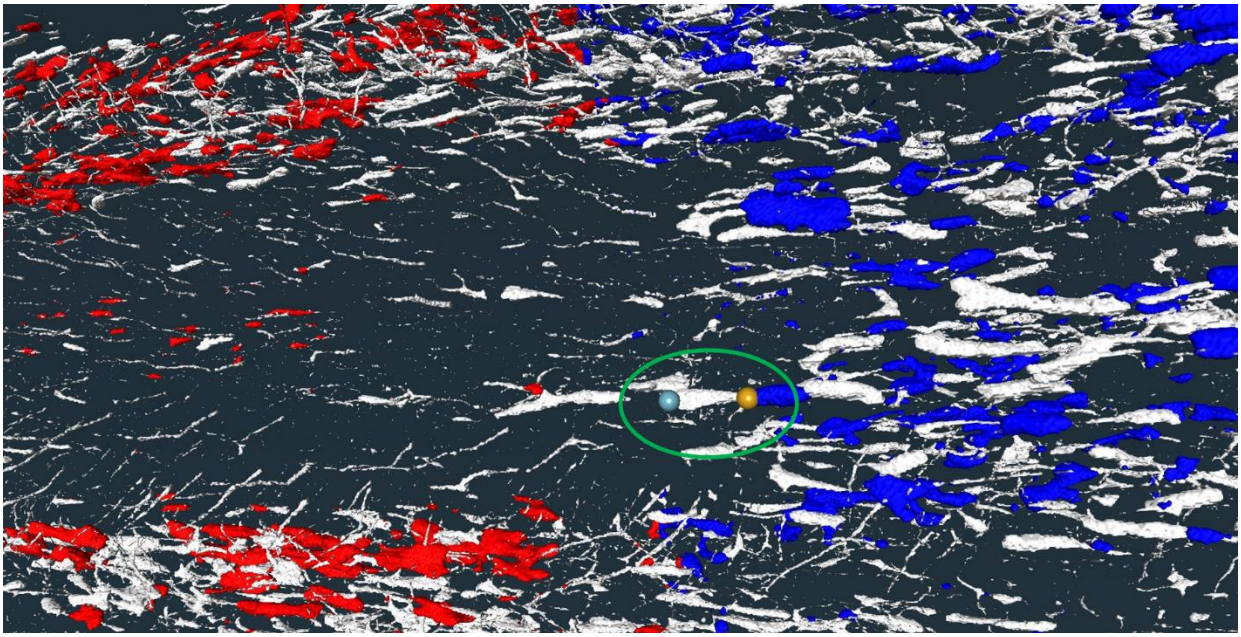

Figure C. 28. (a) Landmark view module in the project view area (red circle). (b) The two landmarks: gold (in vivo) and blue (ex vivo).

5. Once you have finished marking all BMUs, go back to the project view area and click on landmarks-2sets, and then click on export data (Figure C29). Choose the folder to save it. You can read the text files in Excel.

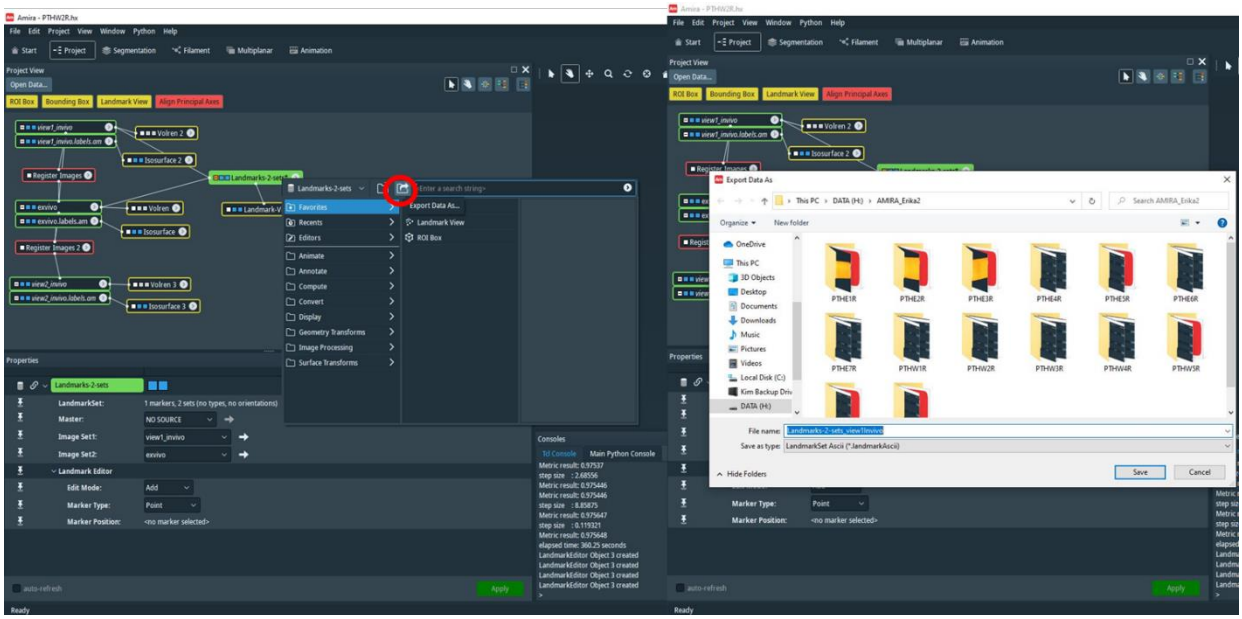

Figure C. 29. Exporting data.

6. Now you can quantify BMUs in View #2 (Figure C30.a). Create the landmarks-2sets in the project view area as described in Step 2. Use the extra viewer to landmark BMUs as described in Step 2. Now you can see the two landmarks: gold (*in vivo*) and blue (*ex vivo*) (green circle in Figure C30.b). Figure C31 shows BMUs landmarked in both views.

a

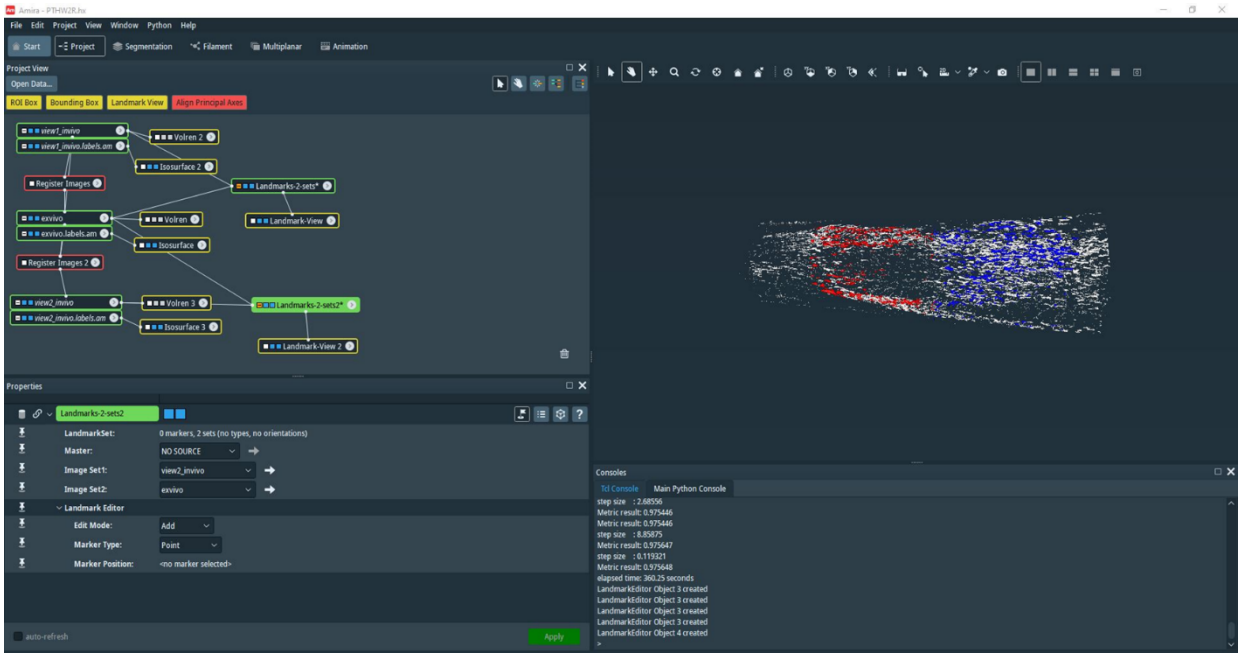

b

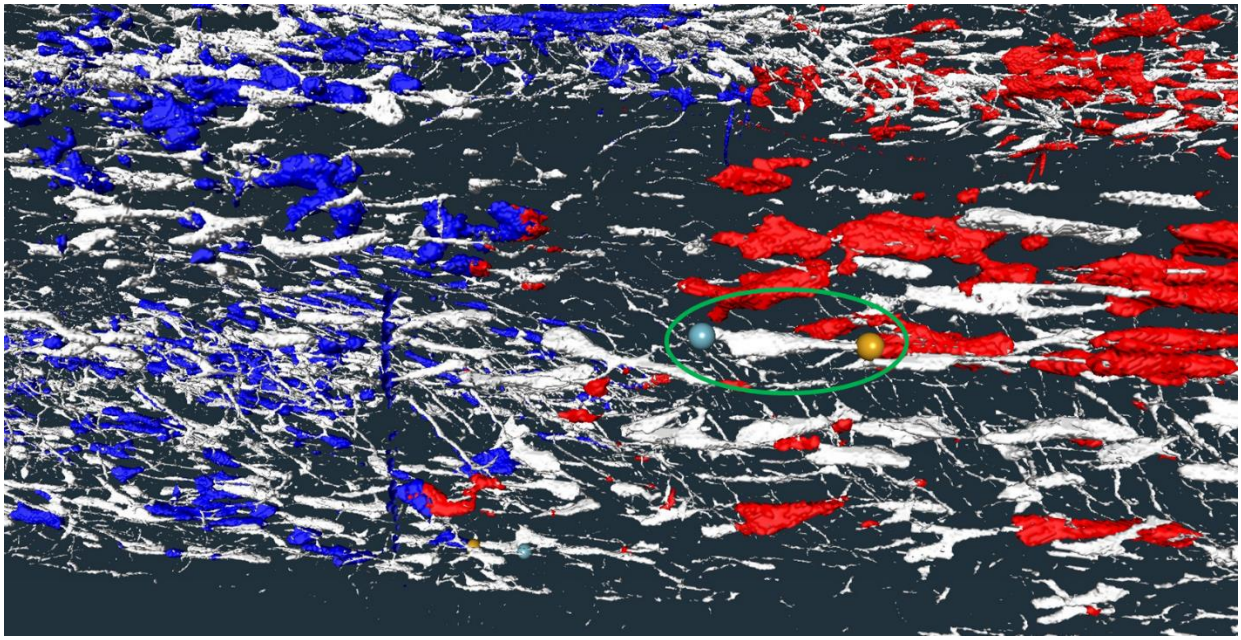

Figure C. 30. (a) Creating landmarks-2sets for View #2. (b) The two landmarks: gold (*in vivo*) and blue (*ex vivo*).

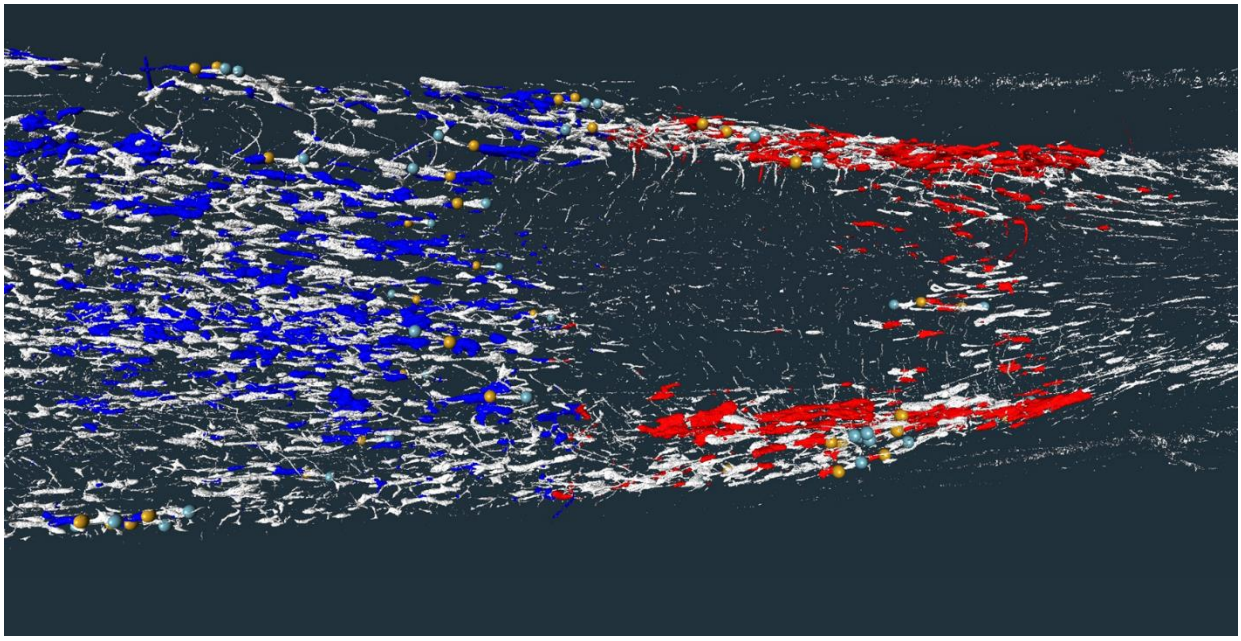

Figure C. 31. BMUs landmarked in both views